NTNU

Norwegian University of
Science and Technology

Dynamic Analysis of a Floating Vertical Axis Wind Turbine using the Actuator Cylinder Flow Theory

Comparative study on a land-based versus
spar vertical axis wind turbine concept and a
code-to-code comparison

Boy Solo Koppenol

Boy S. Koppenol

Dynamic Analysis of a Floating Vertical Axis Wind Turbine using the Actuator Cylinder Flow Theory

Comparative study on a land-based versus spar vertical axis wind turbine concept and a code-to-code comparison

Master's thesis in European Wind Energy Master

Delft – September 29th, 2016

Supervisors:

Dr.ir. C.J. Simão Ferreira
Delft University of Technology, Delft, The Netherlands

Prof. Z. Gao
Norwegian University of Science and Technology, Trondheim, Norway

Dr.ir. Z. Cheng
Norwegian University of Science and Technology, Trondheim, Norway

EWEM

T U Delft Delft University of Technology

NTNU Norwegian University of Science and Technology

Abstract

An ever-increasing demand for electricity pushes the wind energy industry to deep waters that favor floating concepts. Vertical axis wind turbines (VAWTs) failed for onshore applications in the 1980s, but its advantages raise the potential for competitive floating designs and ultimately lowering the cost of energy. This thesis aims to (1) better understand the dynamic response characteristics of such floating concept and (2) critically evaluate numerical tools able to perform fully coupled dynamic analysis on floating VAWTs.

The studied wind energy converter is a combination of DeepWind's two-bladed Darrieus rotor and the OC3 spar floater. A comparative study is made between this spar concept and the equivalent land-based VAWT in both steady and unsteady wind-wave environments. The dynamic responses are calculated by the aero-hydro-servo-elastic code SIMO-RIFLEX-AC, designed to model physical phenomena as accurately and efficiently as possible. Efficiency-driven design solutions imply simplifications in the field of aerodynamic, hydrodynamic and structural modeling. The effect of modeling theories on the calculated dynamic response of the spar VAWT is studied in a code-to-code comparison between HAWC2 and SIMO-RIFLEX-AC. Special attention is devoted to the aerodynamic models, which are both based on the Actuator Cylinder (AC) flow theory.

The model-comparison shows high energy content at the 2P frequency in most responses, this characterizes the two-bladed Darrieus rotor. Aerodynamic loads excite the first tower modes (close to 2P) of the land-based VAWT, whereas the spar VAWT hints to a tower mode around the 4P frequency. Tower tilt of the spar concept – pitch offset extends up to 8° – induces gravitational loads at the tower base and blades, and also reduce the generated power up to 5%. Dynamic content from hydrodynamic loads is strongly felt at the tower base, but the effect of wind turbulence is more significant in terms of platform motions and rotor speed. Introducing wind turbulence reduces the aerodynamic and structural loads.

The code-to-code comparison shows that HAWC2's aerodynamic model calculates lower loads in steady wind, but higher aerodynamic torque in turbulent wind. Dynamic stall significantly increases the lift force in the downwind half of the rotor, causing an overall increase of aerodynamic load at low tip-speed ratios. The wave-induced platform response is stronger in HAWC2, which is also felt at the tower base. The physical mooring system in SIMO-RIFLEX-AC endures an increased mean tension, but its standard deviation is lower.

Acknowledgements

This Master's thesis is carried out in order to obtain the degrees *Offshore Engineering* from TU Delft and *Wind Energy* from NTNU. I have gotten familiar with the topics through a specialization project that took place in Fall 2015 in Trondheim. The major work that is presented in this thesis has been carried out from February 2016 through September 2016 in Delft. My daily supervisors Carlos, Zhen and Zhengshun have assisted me in this period through regular (Skype) meetings and conversations via email. I owe my gratitude to them for each in their own way. Carlos, thank you for your general guidance on writing and structuring this thesis. Zhen, thank you for your input on designing (and adjusting) the approaches and methods applied in this thesis. Zhengshun, thank you for your countless efforts on solving my problems related to the numerical tools, I appreciate it.

With this thesis I close off a truly well-spend two years of my life. The European Wind Energy Master has put me in a very international program that takes place at the technical universities in Copenhagen, Delft and Trondheim. After a rough start, I was forced to work extra hard at TU Delft and NTNU in order to remain with my fellow students and finish in time. I would like to thank my fellow students – and everyone around it – for this unforgettable experience.

Last but not least, I would like to show my appreciation and love to my girlfriend and family. They have not been able to help me out on any technical issues, but they did provide me with moral and emotional support that shaped me to the person I have become today.

Delft, the Netherlands   September 29th 2016

Boy S. Koppenol

Table of Contents

List of Figures

List of Tables

List of Symbols

Latin Symbols

A	Area
$\boldsymbol{A}$	Added mass matrix
C_l, C_d, C_m, C_T, C_p	Lift, drag, moment, thrust, power coefficient
D	Diameter
F, M	Force, Moment
$\boldsymbol{M}, \boldsymbol{B}, \boldsymbol{K}$	Internal structural mass, damping, stiffness matrix
H_s	Significant wave height
Q	Volume force
T_p	Peak period
V	Wind speed
$|X|$	Dynamic response amplitude
a	Axial induction factor
c	Chord
k_a	Correction factor
t	time
u	Particle velocity
$x, \dot{x}, \ddot{x}$	Displacement, velocity, acceleration
x_{static}	Static response amplitude

Greek Symbols

Ω	Rotor speed
Ω_G	Global rotational speed
θ	Azimuth angle
α	Angle of attack
η	Wave amplitude
η_j	Platform motions
ω	Excitation frequency
ω_n	Natural frequency
ϕ	Potential flow
ρ	Density
σ	Standard deviation
τ	Time constant

Acronyms

1P, 2P, 3P, 4P	1,2,3,4-per-revolution
3D	Three dimensional
AC	Actuator Cylinder
AD	Actuator Disk
BEM	Blade Element Momentum
CFD	Computational Fluid Dynamics
DMS	Double Multiple Streamtube
DOF	Degree of Freedom
DTU	Technical University of Denmark
HAWT	Horizontal Axis Wind Turbine
NTNU	Norwegian University of Science and Technology
PSD	Power Spectral Density
TU Delft	Technical University of Delft
VAWT	Vertical Axis Wind Turbine

1 Introduction

1.1 Offshore Wind Energy

The global increase in energy consumption and the depletion of fossil fuels create an important demand for large-scale alternative energy sources. In Europe this problem is recognized and targets are set to realize a renewable energy contribution of 20% in 2020 and 27% in 2030. Wind energy is a clean energy source that can significantly contribute in reaching these targets, currently the wind energy sector makes up more for than 8% of Europe's energy consumption with 142 GW of installed capacity in 2015 [1].

In order to fulfill the large demand for renewable energy the industry is moving towards offshore wind energy. In the open sea there is widely available space, better wind conditions and less visual and auditory pollution. On top of this, it is shown that offshore wind farms are a great addition to marine life. In 2015 the offshore wind energy capacity added up to 11 GW, although this number is rapidly growing.

Some countries around the globe contain little opportunity for the installation of bottom-fixed structures due to deep waters and/or severe environmental conditions. These countries, for instance Norway and Japan, have a current interest in floating wind energy converters. Additionally, the rapid installation of bottom-fixed wind turbines in the North Sea create a trend towards deeper waters that eventually will favor floating wind turbines as well. There is, however, a big challenge involved with respect to the cost of energy. In order for the floating wind turbine industry to contribute at a large-scale, the cost of energy has to be reduced to a competitive level. This creates a re-emerging interest in vertical axis wind turbines (VAWTs) that show potential in realizing this cost reduction.

1.2 Floating Vertical Axis Wind Turbines

Vertical axis wind turbines are characterized by a rotor shaft that is orientated vertically. In contrast with the conventional horizontal axis wind turbines (HAWTs), the vertical axis rotor has a three dimensional swept volume that extends in the streamwise direction as well. Three common rotor configurations – the Savonius, Darrieus and H-type rotors – are shown in Figure 1.1. The working principle of a VAWT as wind energy converter is very different than the conventional HAWT. Its three dimensional swept volume makes that the incoming wind flow is crossed twice by each blade, once in the upstream half and once in the downstream half of the rotor. This may seem like an opportunity for exceeding the Betz limit that describes a

theoretical maximum power that can be extracted from the wind, however, practice has shown the opposite with relatively low efficiencies. The VAWT was popular in North-America during the 1970s and 1980s, in this period considerable efforts were made to develop the Darrieus rotor. A commercialized device was made available in two diameters and installed over 500 times [2]. Though, its popularity vastly diminished when the Darrieus VAWTs started collapsing from fatigue-related issues. Until recently, the wind energy industry did not consider the vertical axis designs and therefore it lacks long track records as opposed to HAWTs.
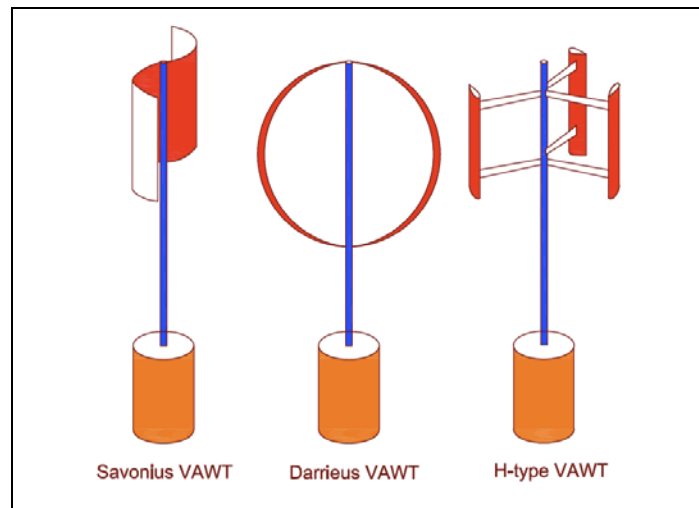
Figure 1.1: Common VAWT rotor configurations [2]

The reason why a re-emerging interest exits for floating VAWTs can be summarized through the following points.

- Simplicity of design
- Lower center of gravity
- Independence of wind direction
- Lower installation, operation and maintenance costs
- (potentially) Lower manufacturing costs
- (potentially) Higher power-extracting efficiency

Many of the above points can be related to machinery position, that can be placed at (or below) the waterline. A great advantage of the Darrieus and H-type rotor design is that its blades can be manufactured through the cost-effective pultrusion technique [3]. An optimized blade profile along the length is less important here because loads can be transferred through multiple joints. On the whole, its potential for extracting more energy at a lower cost has lead to several innovative floating VAWT designs shown in Figure 1.2.
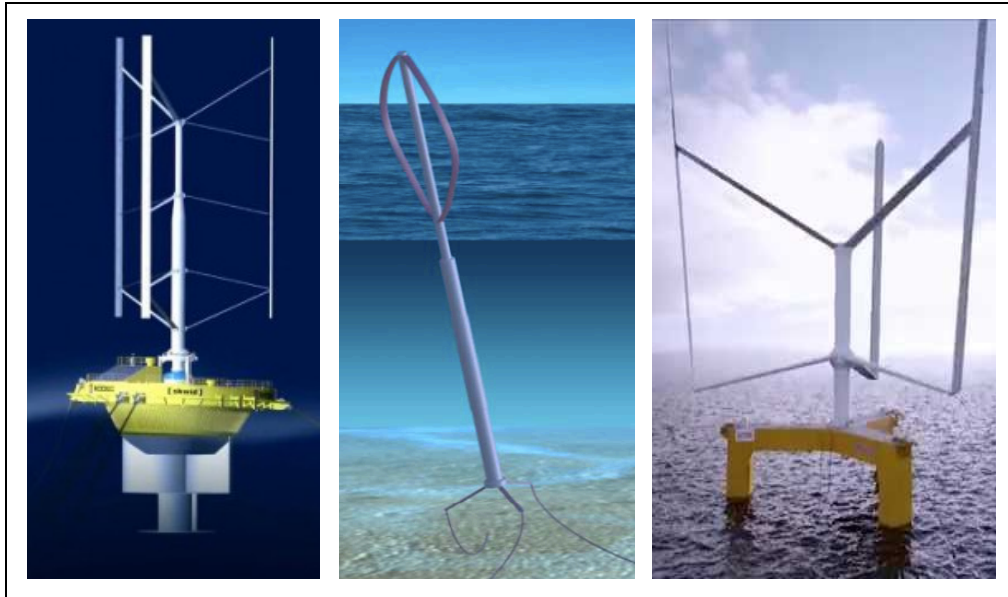
Figure 1.2: Example of innovative floating VAWT concepts [4] [3] [5]

From left to right, the floating concepts are named SKWID [4], the DeepWind concept [3] and Spinfloat [5]. The SKWID concept is a hybrid design by MODEC Inc. that extracts energy from both the wind and current. A 500 kW prototype was installed in 2014 off the coast in South-West Japan. The DeepWind concept is from a project coordinated by Risø DTU and has an innovative rotating platform with the generator acting as ballast. A 1 kW demonstrator was installed in the Roskilde Fjord in 2012. The third concept is Spinfloat by Eolfi and is a pitch-blade innovation. A full-size 6 MW demonstrator is scheduled to be build in 2019.

1.3 Motivation of this Thesis

1.3.1 Numerical Simulation Tools

A lengthy detailed design process takes place before building a large structure such as the innovative concepts in Figure 1.2. In general, the basic floating VAWT system consists of three main components being (1) a turbine for extracting wind power, (2) a floating structure to support the turbine and (3) a mooring system for stabilizing and positioning the floater. In order to minimize the amount of conservatism used in the design of these components, numerical tools are required that can predict environmental loads and the structural responses accurately. The theory and modeling of hydrodynamics and structural dynamics is fairly developed, but the aerodynamics of a VAWT rotor is more complex and introduces challenges with respect to load prediction. Vita [3] categorizes the existing numerical tools for modeling VAWT aerodynamics into the blade element momentum (BEM) codes and vortex codes. Aerodynamic models that are able to predict loads accurately include vortex models, panel models and CFD

models. However, these methods go parallel with high computational costs that make them unsuitable for aero-elastic simulations. Presently, the following simulation tools are publicly available that are capable of modeling floating VAWTs in a fully coupled way.

- FloVAWT by Cranfield University
- CALHYPSO by EDF R&D
- OWENS toolkit by Sandia National Laboratories
- HAWC2 by DTU Wind Energy
- SIMO-RIFLEX-DMS and SIMO-RIFLEX-AC by NTNU/MARINTEK

A large difference between VAWTs and HAWTs is the amount of track record that is available. For instance, some of the above codes have been verified using data from measurements on a $34\ m$ onshore VAWT by Sandia in the 1980s. This illustrates why it is common to verify newly developed numerical methods using other (verified) simulation tools.

1.3.2 Aim and Scope

It has become evident that there is an interest to broaden the understanding of floating VAWTs. This thesis aims to form a basis of understanding for the dynamic response characteristics of a floating VAWT concept from fully coupled time-domain simulations in SIMO-RIFLEX-AC. The concept is constructed from DeepWind's Darrieus rotor and the OC3 spar platform. The basic understanding of the dynamic behavior will be created through analysis of the excitation loads and the structural response of the spar VAWT in a steady environment. Whereas most previous research deal with steady wind environments only, this thesis also aims to understand the dynamic responses in fully turbulent wind and irregular wave environments. The aerodynamic load calculations are based on the Actuator Cylinder (AC) flow theory and the hydrodynamics will be computed from potential flow theory.

The second part of this thesis consists of a code-to-code comparison between SIMO-RIFLEX-AC and HAWC2. Here the main scope is to understand the effect of different implementations of the AC flow theory, but also to understand the impact of other physical phenomenon such as dynamic stall and structural modeling. The study aims to achieve this through isolating the aerodynamic model from any structural and hydrodynamic influences. The tests consist of multiple steady environmental conditions and uses an equivalent rigid land-based VAWT model. Additionally, it is aimed to understand differences that could exist between the codes in a fully dynamic environment using the spar VAWT model.

1.4 Overview of the Report Structure

The report is structures through six chapters. Starting with the introduction, in Chapter 1, outlining the motivation and aim of this thesis work. A solid theoretical framework is created in Chapter 2 by explaining the dynamics of floating VAWTs, AC flow theory, flow dynamics, wave theory, hydrodynamics and VAWT control theory. This is followed by a description of the studied VAWT models, numerical tools and designed load cases in Chapter 3. The results of the first part of this thesis, related to understanding the dynamic response characteristics of the spar VAWT, are presented and extensively discussed in Chapter 4. The same is done for the results from the code-to-code comparison in 5. The thesis is concluded in Chapter 6, where also recommendations for future work are given.

2 Theoretical Framework

Chapter 2 provides the theoretical framework on which the discussed concepts in this thesis are built. First a description of the dynamic equilibrium, rigid-body motion analysis and structural modeling of floating VAWTs is given in Section 2.1. This is followed by a detailed explanation of the Actuator Cylinder flow theory formulation in Section 2.2, which will help understanding the aerodynamic load calculation applied in this thesis. Modeling the effect of dynamic stall and inflow in a VAWT rotor is covered Section 2.3. Potential wave theory and methods for hydrodynamic load calculation are described in Section 2.4 and Section 2.5, respectively. At last the relevant theory on control strategies and control algorithms are presented in Section 2.6.

2.1 Dynamics of a Floating Vertical Axis Wind Turbine

A floating wind turbine can be considered as a separate system on which external loads are applied that together induces a dynamic response. The system is subjected to aerodynamic, hydrodynamic and internal structural loads that are satisfied by a dynamic equilibrium. This equilibrium essentially means that the forces or moments in each degree of freedom (DOF) of the system are in balance with the dynamic response (acceleration, velocity and displacement) of that DOF. The dynamic equilibrium of a floating wind turbine system can be described by the following equation of motion.

$$(M + A)\ddot{x}(t) = -B \cdot \dot{x}(t) - K \cdot x(t) + F^{ext}(x, \dot{x}, t) \tag{2.1}$$

Here M, B and K describe the internal structural mass, damping and stiffness matrix of the full system. Written on the left-hand-side is also the added mass matrix A, which is a frequency-dependent characteristic related to hydrodynamic wave radiation. All external loads are included in F^{ext}, which is not only dependent on time but also on the dynamic response of the structure. The latter is related to using velocities relative to the structure in aerodynamic and hydrodynamic load calculation. Additionally, hydrostatic forces on the hull and (seabed) loads on the anchors of the mooring system are related to the instantaneous displacement $x(t)$ of the floating system. The external loads can be categorized into the components given by Equation (2.2).

$$F^{ext}(x, \dot{x}, t) = F^{aero}(x, \dot{x}, t) + F^{hydrodynamic}(x, \dot{x}, t) +$$
$$F^{hydrostatic}(x, t) + F^{anchor}(x, t) \tag{2.2}$$

In numerical solvers the presented dynamic equilibrium is often simplified to restrict computational efforts. As an approximation, the floater is often considered rigid which largely reduces the system. This makes the floating platform a large element described by 'only' six DOFs. For structural components such as the blades and tower of a VAWT the structural elasticity plays an important role, hence elastic deformations should not be ignored [6]. Rigid-body motion analysis is described in Section 2.1.1, structural dynamics at the element-level is explained in Section 2.1.2 and numerical integration methods are discussed in Section 2.1.3.

2.1.1 Rigid-Body Motion Analysis of a Floating Wind Turbine

Defining the Coordinate System

A rigid floating platform knows six DOFs, which can be further distinguished into three translational and three rotational DOFs. The platform motions are referred to as surge, sway, heave, roll, pitch and yaw. In this thesis work it is chosen to set the surge parallel to the streamwise direction and sway perpendicular to the wind direction. Heave is defined positively upwards. The rotational DOFs are rotating about their corresponding translational DOFs according to the conventions. The definitions and orientations of the platform motions are illustrated by Figure 2.1. The definition of the platform motions is in line with the global coordinate system used throughout.
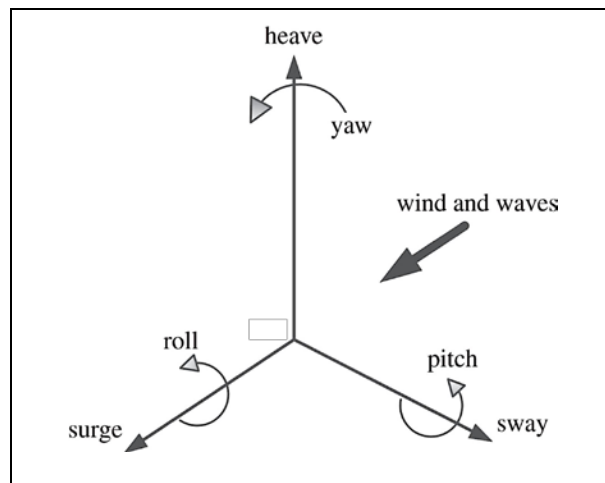
Figure 2.1: Definition of the platform motions

Coupling of Platform Motions

Due to the geometrical nature of a floating platform some DOFs are coupled to each other. This means that a platform response in one DOF can induce a response in another DOF. Hence the translations and rotations of the platform are not always independent and can be connected by coupling constraints. For instance, a floating platform moored by catenary mooring lines will experience a (small) heave response when displaced in surge or sway. The platform motions can be coupled through acceleration, velocity and displacement. The coupling constraints are represented by the off-diagonal elements in the structural and added mass matrices M, B, K and A.

Natural Frequency

On a global level, the platform motions are very dominant when compared to the elastic deformations of the rest of the structure. For this reason, it is often of interest to analyze the

2.1 Dynamics of a Floating Vertical Axis Wind Turbine

natural frequency of the platform in each DOF in order to recognize and/or avoid resonance conditions. The natural frequency of a floating wind turbine is dependent on all terms found in the equation of motion (see Equation (2.2)), except for the pure influence from environmental conditions such as the wind-induced aerodynamic loads and wave-induced hydrodynamic loads. The natural frequencies of a floating platform can by computed by means of a free decay test. Here the floating wind turbine is given an initial displacement in the analyzed DOF for a windless and still water environment. The dynamic response of the platform motion will reveal information about the damping and natural frequency of the floating system in the corresponding DOF. A numerical decay test is performed in this thesis work and presented in Section 3.2.2.

In structural design it is essential to keep the loads to a minimum, hence a fully coupled analysis should be performed to learn about the structure's response to dynamic loading. The dynamic response amplitude is dependent on the frequency of the loading. The general variation of the dynamic amplitude with the loading frequency is shown in Figure 2.2. The dynamic response amplitude $|X|$ and loading frequency ω are non-dimensionalized with the static response amplitude x_{static} and natural frequency ω_n, respectively.
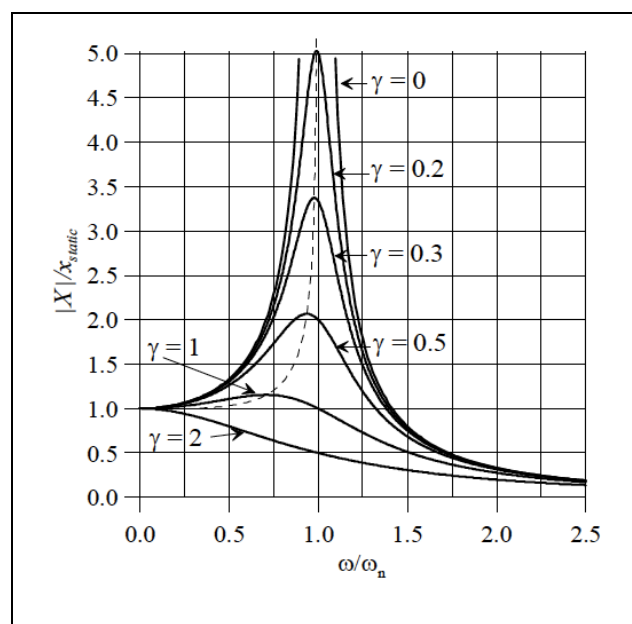
Figure 2.2: Dynamic amplification from loading with a frequency content [7]

It can be seen that for relatively slow varying loads ($\omega \ll \omega_n$) the dynamic response is equal to the static response. The reason for this is that the load is so slow that the structural response follows statically. On the other hand, for relatively quick varying loading ($\omega \gg \omega_n$) the structure has no time to respond to variations and hence the dynamic amplitude tends to zero.

10

The most important phenomenon occurs when the loading frequency is equal or close to the natural frequency ($\omega \approx \omega_n$), because in theory the dynamic amplitude could then tend to infinity. This phenomenon is called resonance and can impose large amplitude loading on a floating wind turbine. The actual dynamic amplitude for the resonance condition is dependent on the amount of damping that is present in the system.

2.1.2 Structural Modeling of a Vertical Axis Wind Turbine

In this thesis, a vertical axis wind turbine is mounted on top of the floating platform. It was mentioned previously that the elastic deformations within the tower and blades are significant and should not be neglected. The actual structure can be broken down to the atom level, however, this is not very convenient for numerical solvers. A method is required to model the structure as accurately and as efficiently as possible. The finite element method is a widely applied modeling technique that allows for sufficient freedom in the weighing between accuracy and numerical efficiency. This section describes the theory behind the structural modeling of a VAWT.

Finite Element Method

A structure can be divided into a number of small elements in order to form a finite element model, as the name suggests. The elements can be of arbitrary shape and size. Each element has its own DOFs, such as the floating platform described previously. By introducing interface conditions, it is possible to describe how an element behaves with respect to another element. This concept is similar to the coupling of motions as described before. If all interface conditions are defined, then the internal structural response can be calculated upon the displacement of one of the elements. However, in order fix the structure in space, boundary conditions have to be introduced. In case of the land-based VAWT in this thesis, it is assumed that the basis is rigidly connected to the ground. This boundary condition essentially defines that the elements directly in contact with the ground are constraint in all DOFs. Accordingly, the elements connected to these rigidly connected elements would respond according to the interface conditions when the structure is excited. At last, it is required to know the initial conditions in order to be able to solve the equation of motion. When the system is provided with enough information to solve or calculate the dynamic response, the system is referred to as well-conditioned.

Elements can be further classified according to their characteristics or properties in order to realize system reduction. Here there will be distinguished between bar and beam elements. Bar

elements are assumed to be straight with a constant cross-sectional area. The element has three translational DOFs at each node (end of the element), and loads can only be transferred in the axial direction (see Figure 2.3). This means that no bending moments are present and that no bending or torsional deformations can take place.
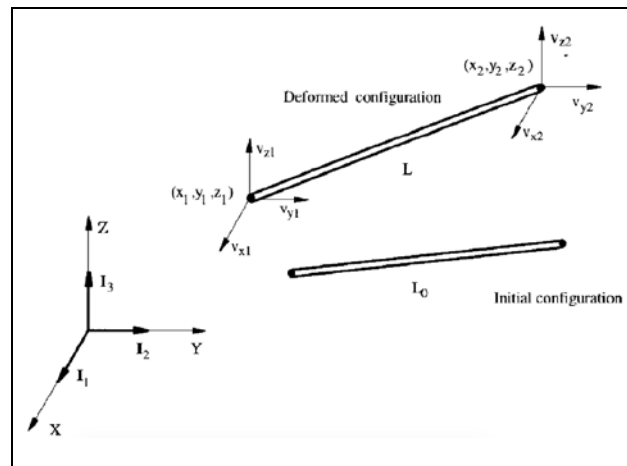
Figure 2.3: Illustration of bar element [8]

Small strain is commonly assumed, which is then calculated from a normal force, initial configurations and material properties. Equation (2.3) describes this relation, where $\frac{L - L_0}{L_0}$ is the strain and A the deformed cross-sectional area.

$$F_N = \frac{L - L_0}{L_0} \cdot E \cdot A \qquad (2.3)$$

A beam element is slightly more complex in its formulation. It has six DOFs at each node, hence both translational and rotational deformations are possible when modeling a beam element. A schematic of a beam element is illustrated in Figure 2.4.
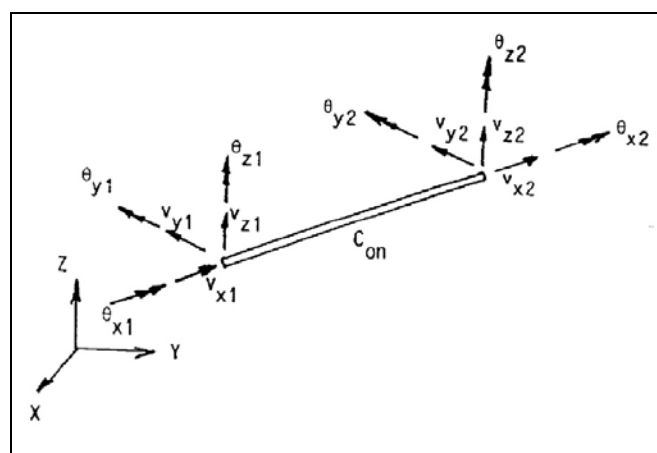
Figure 2.4: Illustration of beam element [8]

12

The beam can be modeled according to an extension of the classical beam theory, which is the Timoshenko beam theory [9]. An example is shown in Figure 2.5. Taking into account both shear deformation and rotational effects allows the beam elements to model a wide variety of structural parts of a VAWT.
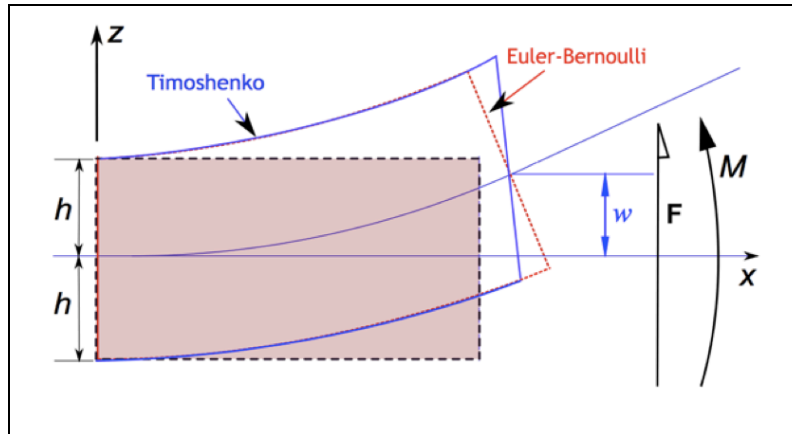
Figure 2.5: Deformation of a Timoshenko beam element [10]

Similar as the bar element theory, the strains are assumed to be small for the beam theory to be valid. For linear elastic beam theory, the shear force F and bending moment M as function of displacement w and rotation ϕ are given by Equations (2.4) and (2.5).

$$F_{xx} = \kappa \cdot A \cdot G \cdot (-\phi + \frac{\delta w}{\delta x}) \tag{2.4}$$

$$M_{xx} = -E \cdot I \cdot \frac{\delta \phi}{\delta x} \tag{2.5}$$

Multi-Body System

The multi-body system formulation is a variation of the FEM by dividing the structure into a number of (mechanical) bodies. Each body has its own coordinate system and they are interconnected by joints. The joints represent constraints that limit the bodies' DOFs. A visual representation of such system is shown in Figure 2.6. The bodies are constructed of a finite amount of Timoshenko beam elements, modeled according to the finite element method theory described in the previous section. Here small deflections are assumed within the bodies, so that the dynamic behavior can be determined by linear Timoshenko beam theory. On a global level however, a structure like a wind turbine cannot be assumed to behave linearly. The multi-body system accounts for non-linear effects (such as large deformations) in the coupling constraints between the bodies. It is therefore required that a sufficient amount of bodies is used to build

the structure, especially for the flexible and lengthy blades of a VAWT. The mass and moment of inertia can be specified for each body in its local coordinate system.
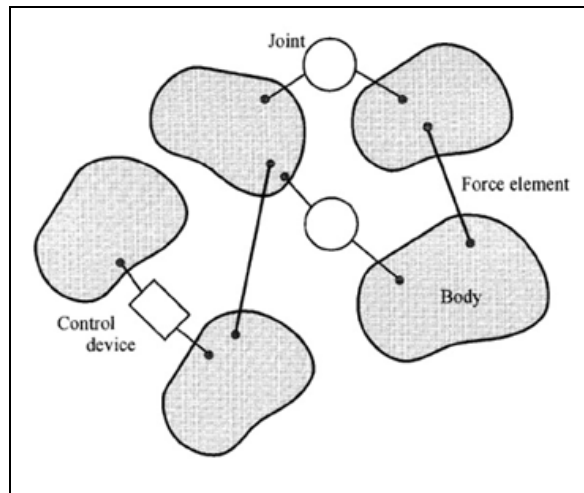
Figure 2.6: Visualization of the multi-body structural model [11]

Structural Damping

Internal structural damping – B in the equation of motion – accounts for energy dissipation in the structure itself. It is strongly dependent on the cross-sectional properties of the structure. Measurements have shown that different structural damping levels can be related to axial, torsional and bending deformations [8]. A popular and efficient method that is applied in practice is Rayleigh damping. This calculates the internal structural damping through a linear combination of mass and stiffness. Equation (2.6) shows the degree of structural damping in an element with mass m and stiffness k.

$$b = \alpha \cdot m + \beta \cdot k \tag{2.6}$$

Since the mass and stiffness are respectively inversely and directly proportional to frequency ω, the total Rayleigh damping becomes a non-linear function of frequency. This is illustrated by Figure 2.7. The method can be extended to account for the full structure, in which the Rayleigh coefficients α and β would become vectors describing the modal damping.

2.1.3 Numerical Integration Method

In time-domain analysis it is required to satisfy the dynamic equilibrium of the system at every time step. When non-linear behavior is involved, it is required to estimate the structural response at the next time step by numerical integration. The predicted response also influences the external loads, since these are a function of the structural velocities and displacements.

Interpolating functions are used for describing the acceleration between the current and next time step. A simple method is the constant average acceleration method. This would assume a constant acceleration which is the average between the current acceleration $\ddot{x}_i$ and the acceleration at the next time step $\ddot{x}_{i+1}$. The corresponding velocities and displacements would then be calculated through basic physics. This method is unconditionally stable. However, it does not allow the user to express the amount of 'thrust' in the predicted structural response at the next time step. A numerical integration tool that is able to do this is the Newmark-β method.
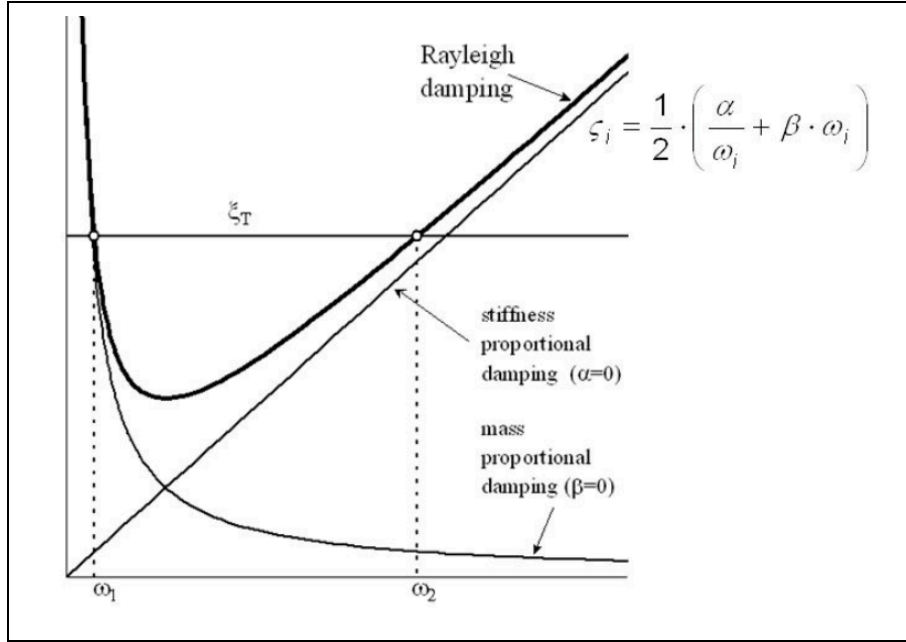
Figure 2.7: Rayleigh damping as function of frequency [12]

The Newmark-β method is described by the factors γ and β ranging between 0 and 1. The factor γ specifies the assumed percentual acceleration of next time step, and β specifies the degree at which the displacement at the next time step x_{i+1} is influenced by $\ddot{x}_{i+1}$. The resulting displacement x_{i+1} and velocity $\dot{x}_{i+1}$ can then be formulated as following.

$$x_{i+1} = x_i + \Delta t \cdot \dot{x}_i + (\Delta t)^2 \cdot \left(\left(\frac{1}{2} - \beta \right) \cdot \ddot{x}_i + \beta \cdot \ddot{x}_{i+1} \right) \qquad (2.7)$$

$$\dot{x}_{i+1} = \dot{x}_i + \Delta t \cdot \left((1 - \gamma) \cdot \ddot{x}_i + \gamma \cdot \ddot{x}_{i+1} \right) \qquad (2.8)$$

Due to the amount of factors involved in the dynamic equilibrium it is often not possible to predict the structural response at the next time step correctly in one attempt. Hence in numerical analysis an iterative procedure is applied for the solution to converge within the set accuracy.

2.2 Aerodynamic Modeling of a Vertical Axis Wind Turbine

An aerodynamic model describes the interaction between a structure and the surrounding flow field. The conventional method of calculating aerodynamic loads on a wind turbine is the Actuator Disk (AD) model based the Blade Element Momentum (BEM) theory. Whereas this model is applicable on HAWT aerodynamics, VAWT aerodynamics is more complex and requires an alternative approach. The 3D trajectory of the VAWT rotor imposes several challenges on the field of aerodynamics. For instance, the blade elements experience a continuous change of relative speed and direction, encounter their own wakes and operate both in stalled and unstalled conditions [13]. A short overview of aerodynamic models that can deal with these challenges is given in Section 2.2.1, this is followed by an extensive description of the AC flow theory in Section 2.2.2.

2.2.1 Overview of Aerodynamic Models

Currently, the aerodynamic models can be categorized into five types: vortex models, cascade models, panel models, streamtube models and the AC flow model [14]. The prior three aerodynamic models are more complex and have high computational demands. For the application of time domain simulations of VAWTs the streamtube models and AC flow model are more suitable, hence these are covered in more detail for being more relevant to this thesis work.

Vortex Model

The vortex models assume potential flow and calculate the velocity field through the vortices in the wake of blades, the lift is calculated through the strength of the bound vortices.

Cascade Model

The cascade models originate from the turbo machinery industry and positions the blades in a row on a plane surface separated by their circumferential distance. The wake velocity and free stream velocity are related through Bernoulli's equation, whilst a semi-empirical expression relates the induced velocity to the wake velocity.

Panel Model

The panel models have been widely applied in naval hydrodynamics and aircraft aerodynamics. Its principle is to discretize a 3D surface into non-penetrable panels and solve the Laplace equation in terms of velocity potential by placing a source or doublet on each panel. The panel

model is recently extended into a 2D panel model that is more suitable for simulating an unsteady 2D flow past a VAWT.

Streamtube Model

The streamtube models are derived from the classical BEM theory and are based on the conservation of mass and momentum in the streamwise direction. The most comprehensive streamtube model is the Double Multiple-Streamtube model (DMS model) developed by Paraschivoiu [15] [16]. As the name reveals, there is multiple streamtubes that make up the swept area of the VAWT rotor. Additionally, the upwind and downwind half of the rotor is divided by introducing a tandem of Actuator Disks (ADs) in the streamwise direction. A schematic of a streamtube and ADs in tandem in the DMS model is shown for a Darrieus rotor in Figure 2.8.
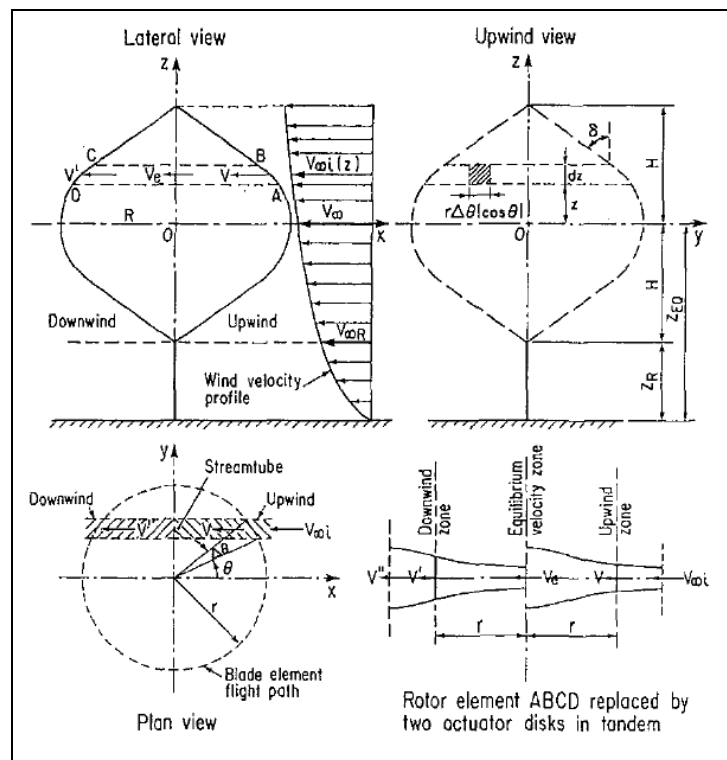
Figure 2.8: Schematic of the DMS model in the geometry of a Darrieus rotor [17]

The multiple streamtubes have the capability to independently model different aerodynamic phenomena across the swept volume of the rotor. This is a valuable addition compared to the simplest streamtube model, because a continuously changing angle of attack and relative flow velocity – with height and azimuth angle – characterizes a VAWT. The addition of modeling two ADs in tandem allows one to consider the variation of induced velocity as function of azimuth angle for each streamtube. Moving towards the design of floating wind turbines, Wang

et al. [18] reformulated the traditional DMS model to account for the effect of tower tilt. This is done by splitting the freestream velocity into a component parallel and perpendicular to the tower caused to tilt by rolling and pitching motions of the floating VAWT. Generally, the DMS model is widely used in aeroelastic analysis due to its simplicity and computational efficiency.

Actuator Cylinder Flow Model

The AC flow model is developed by Madsen [19] during 1979 to 1982, this was done in an effort to extend the Actuator Disk concept for HAWTs into an approach coinciding with the 2D swept area of a VAWT. The 2D cylinders are stacked to model the swept volume of a VAWT rotor. Blade element theory is used to calculate the aerodynamic loads on the blade, which are then applied as volume forces on the AC both normal and tangential to the rotor plane. The AC representation and the (expected) blade element and volume forces are shown in Figure 2.9.
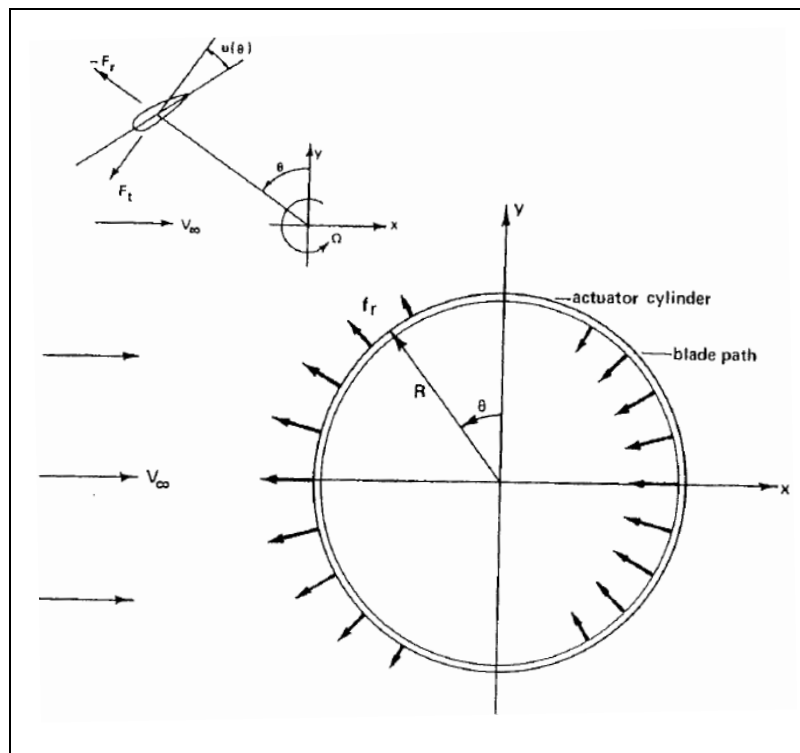
Figure 2.9: Representation of a 2D VAWT by an Actuator Cylinder [19]

The induced velocities in the flow field are related to the volume forces through combining the equation of continuity with the Euler equations. In the solution there exists both a linear and non-linear part. For a more efficient model Madsen [19] suggested a modified linear solution that excludes the non-linear terms in the induced velocity calculation. However, Madsen et al. [20] argued that the accuracy of the modified linear solution could be improved by an additional

correction factor. Recently Cheng et al. [21] proposed a different correction factor to further improve the accuracy of the modified solution at higher tip-speed ratios. The linear solution with modifications from Madsen [19], Madsen et al. [20] and Cheng et al. [21] are from now on referred to as modified solution I, II and III, respectively. There are still uncertainties with the accuracy of the AC flow model. One of these is that it neglects discrete vortices from the upwind blade circulation. This affects the downstream blade but the overall consequences are expected to be minor according to Larsen & Madsen [22].

Model Comparison

In a comparison between six different numerical models that deal with VAWT aerodynamics, it is argued by Ferreira et al. [23] that the AC flow model is more accurate than the DMS model. This code-to-code comparison is designed such to isolate the aerodynamic models and to make distinction between instantaneous (azimuth dependent) results and integral (rotor-averaged) results. When compared against the other numerical codes, including more complex 2D and 3D vortex models, the DMS model came forward as fundamentally incorrect. Larsen & Madsen [22] confirm this by stating that the AC flow model physically gives a more correct solution, arguing that a tandem of ADs do not coincide with the actual swept volume of a VAWT rotor. Additionally, the influence of the downstream half of the rotor on the upstream half is not captured by the DMS model. The AC flow model takes into account the interaction of a blade segment with its full surrounding. It is suggested that without an empirical correction the DMS model should be discontinued in VAWT aerodynamics [23]. For the previous arguments, the aerodynamics in this thesis work are calculated by the modified linear solution II and III of the AC flow model. The theoretical formulation underlying the AC flow model is explained in the following.

2.2.2 Actuator Cylinder Flow Theory

Coordinate System

In order to understand the basic working principles of the AC flow theory a coordinate system should be defined. The formulation of the coordinate system as presented in Larsen & Madsen [22] is considered logical and will be used throughout. All together the VAWT is described by the four coordinate systems shown in Figure 2.10.
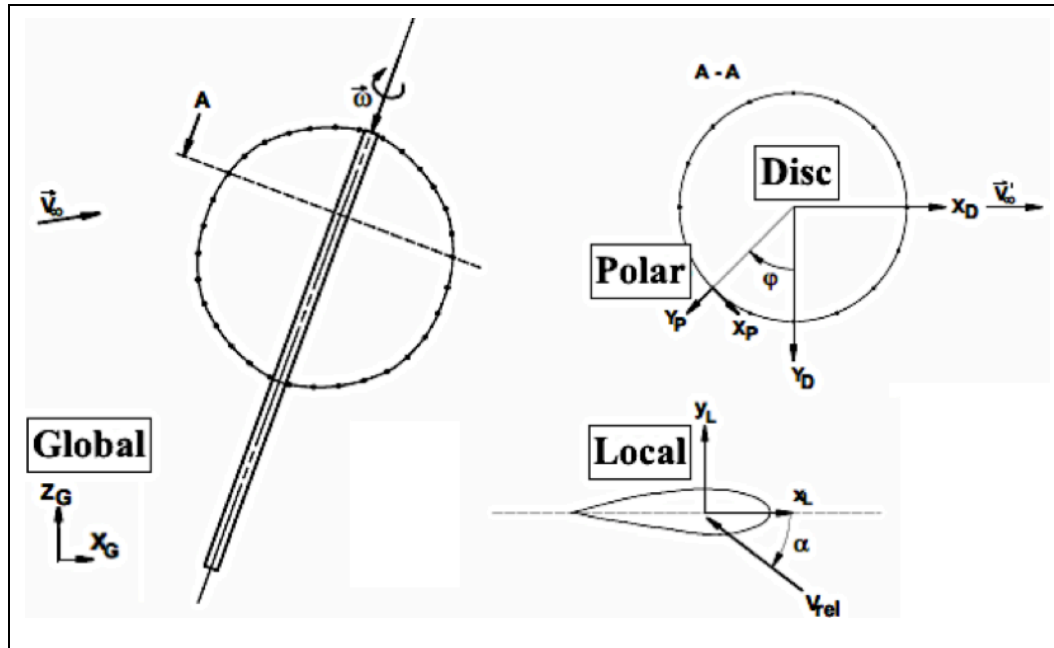
Figure 2.10: Definition of the coordinate system used for the AC flow model

The global coordinate system (G) has the y-axis aligned with the freestream velocity V_∞ and the z-axis pointing vertically down. The disc coordinate system (D) has the z-axis along the shaft rotation vector ω_s and its x-axis is aligned with the projection of V_∞ on the disc plane, named V_∞'. The polar coordinate system (P) describes the blade path in radial coordinates. At last, the local coordinate system (L) is defined such that the x_L-axis is parallel to the chord of the airfoil. The coordinate systems are interrelated with transformation matrices $\boldsymbol{T_{AB}}$ (from system A to B), the letter in variable subscript refers to the coordinate system in which the variable is defined.

Aerodynamic Load Calculation

The AC flow model assumes an ideal VAWT rotor and by that it considers an infinite amount of blades, similar as done in the classic BEM theory. Through blade element theory the aerodynamic loads on the blades can be calculated using the lift coefficient C_l, drag coefficient C_d and the relative wind speed V_{rel}. To fully describe the aerodynamic forces it is also necessary to know the moment coefficient C_m [24]. However, the moment coefficient has no direct influence on the lift- and drag forces – which are of interest in the AC flow model – and are therefore left out of the formulation. The performance coefficients (C_l and C_d) are a function of the angle of attack, Reynolds number and Mach number. Due to the complex flow around the blade, the airfoil data or performance coefficients are often determined in a wind tunnel [24]. The angle of attack is found when examining the direction of V_{rel} relative to the chord of the blade element, this is shown by the airfoil in Figure 2.10. The magnitude and

direction of the local inflow velocities (two components of V_{rel}) are dependent on the freestream velocity $V_{\infty,G}$, induced flow velocity $V_{induc,G}$ and profile velocity $V_{L,G}$. The index G indicates that the velocity components are defined in the global coordinate system. The local inflow velocity $V_{infl,L}$ in the local coordinate system is found from the superposition in Equation (2.9).

$$V_{infl,L} = \boldsymbol{T_{GL}}\left(V_{\infty,G} + V_{induc,G} - V_{L,G}\right) \tag{2.9}$$

The freestream velocity is determined when generating the wind kinematics of either a steady or turbulent wind environment. The induced wind velocity is based on the calculated induced velocity in a previous time step. At last, the profile velocity is determined from the instantaneous rotor speed and structural deformations.

The magnitude V_{rel} and direction α of the relative wind velocity can be determined utilizing Equations (2.10) and (2.11).

$$V_{rel} = \sqrt{V_{infl,L}(1)^2 + V_{infl,L}(2)^2} \tag{2.10}$$

$$\alpha = \tan^{-1}\left(\frac{V_{infl,L}(1)}{V_{infl,L}(2)}\right) \tag{2.11}$$

At last, the radial loading F_r and tangential loading F_t for any point on the circumference can be calculated in polar coordinates.

$$F_r = {}^1\!/_2\, \rho_{air}\, c\, V_{rel}{}^2\, C_l \tag{2.12}$$

$$F_t = {}^1\!/_2\, \rho_{air}\, c\, V_{rel}{}^2\, C_d \tag{2.13}$$

The aerodynamic loading in polar coordinates are used as input to the 2D flow problem described in the following.

2D Flow Problem

The aerodynamic loads from Equations (2.12) and (2.13) are made non-dimensional with the basic dimensions R, ρ_{air}, V_∞ and then imposed as body forces Q_r and Q_t onto the flow. The body forces are illustrated in Figure 2.11, which shows the typical direction of the force along the rotor periphery.
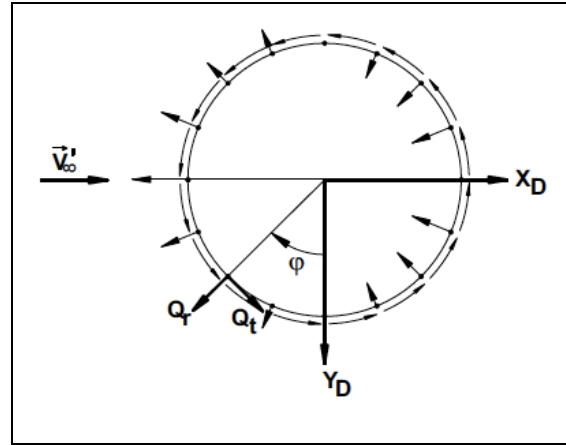
**Figure 2.11: Actuator Cylinder flow model
with typical body forces Q_r and Q_t [22]**

The non-dimensional body forces are given by Equations (2.14) and (2.15), here the radial force Q_r is defined positively outwards.

$$Q_t = -B\frac{c\,C_{d,P}}{4\pi\,R}\cdot\frac{V_{rel}^2}{V_\infty^2} \tag{2.14}$$

$$Q_r = B\frac{c\,C_{l,P}}{4\pi\,R}\cdot\frac{V_{rel}^2}{V_\infty^2} \tag{2.15}$$

The body forces presented are based on the local element being parallel to the rotating shaft. However, this is not the case when considering a VAWT rotor with curved or helical blades as shown in Figure 2.12.

An addition to the body forces is suggested by Cheng et al. [21] that takes into account the inclination of the local element. The body force formulation is presented in Equations (2.16) and (2.17). Note that here the blade loads $F_{n,A}$ and $F_{t,A}$ are defined in the cross-section plane of the airfoil, whereas the volume forces presented previously are utilizing $F_{n,B}$ and $F_{t,B}$ (see Figure 2.12). The addition made for the local element inclination is physically more correct and shows good agreement with experimental results [21].

$$Q_t = -B\frac{F_{n,A}}{2\pi\,\rho_{air}R\,V_\infty^2\sin(\beta)} \tag{2.16}$$

$$Q_r = B\frac{F_{t,A}}{2\pi\,\rho_{air}R\,V_\infty^2\sin(\beta)} \tag{2.17}$$
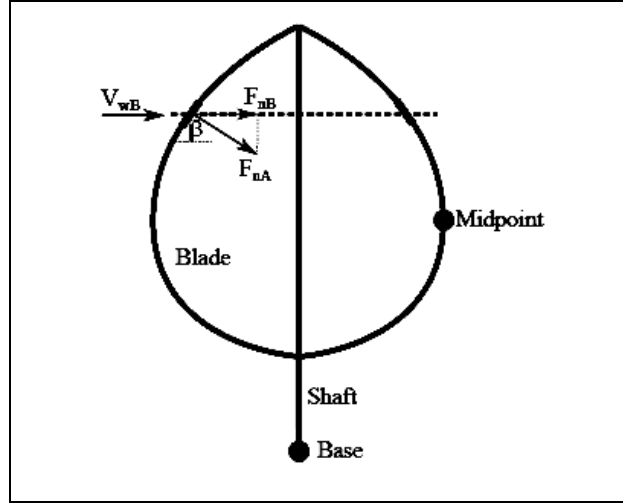
Figure 2.12: Illustration of the local element force acting on the blade of a Darrieus rotor [21]

In order to solve the 2D quasi-static flow problem the methods of Madsen et al. [20] are followed. The solution is built on the Euler equations in 2D, where the velocity component in x-direction v_x is written as $1 + w_x$ in order to create a linear and non-linear term. The equation of continuity is then combined with the Euler equations. Rewriting this solution yields a Poisson type equation for the pressure p given by Equation (2.18).

$$\frac{\partial^2 p}{\partial x^2} + \frac{\partial^2 p}{\partial x^2} = \left(\frac{\partial f_x}{\partial x} + \frac{\partial f_y}{\partial y}\right) + \left(\frac{\partial g_x}{\partial x} + \frac{\partial g_y}{\partial y}\right) \tag{2.18}$$

Here f is volume force and g is the induced or second-order force defined in the following.

$$g_x = -\left(w_x \frac{\partial w_x}{\partial x} + w_y \frac{\partial w_x}{\partial y}\right) \tag{2.19}$$

$$g_x = -\left(w_x \frac{\partial w_x}{\partial x} + w_y \frac{\partial w_x}{\partial y}\right) \tag{2.20}$$

The solution to the pressure field described by Equation (2.18) is found when integrating over the region where the volume forces are non-zero. This is realized by a double integral over the streamwise direction and the lateral direction. The pressure field induced by the volume forces f and the second-order forces g can be kept separated, and are named respectively $p(f)$ and $p(g)$.

Now that the pressure field is known, the velocities can be derived from the previously mentioned Euler equations. The final solution is shown in Equations (2.21) and (2.22). It should

be noted that the solution is a summation of a linear and non-linear part, which are terms dependent on respectively f and g.

$$w_x = -p(f) + \int_{-\infty}^{x} f_x dx' - p(g) + \int_{-\infty}^{x} g_x dx' \qquad (2.21)$$

$$w_y = \int_{-\infty}^{x} \frac{\partial}{\partial y} p(f) dx' + \int_{-\infty}^{x} f_y dx' - \int_{-\infty}^{x} \frac{\partial}{\partial y} p(g) dx' + \int_{-\infty}^{x} g_y dx' \qquad (2.22)$$

A linear solution can be worked out from the normal force loading, as its magnitude is much larger than the tangential loading [20]. Assuming piece-wise constant loading a linear solution can be found containing time-independent integrals. This allows for minimal computational efforts. Cheng et al. [21] presented a linear solution of the induced velocities that considers the tangential loading as well. The linear solution with and without the tangential loading term is compared and the difference is minor. However, including the tangential term is physically more correct and therefore adopted in the aerodynamic model of SIMO-RIFLEX-AC by Cheng et al. [25].

Modified Linear Solution

In order to perform aeroelastic simulations in numerical tools it is essential that the full AC flow model is linearized. As discussed previously, Madsen [19] provided a modified linear solution that was corrected by Madsen et al. [20] in 2013 for implementation in HAWC2. Further corrections were made by Cheng et al. [21] in 2016 for the implementation of modified solution III in SIMO-RIFLEX-AC. Initially, the accuracy of modified linear solution I by Madsen [19] was argued to be too low at higher loading.

Madsen et al. [20] performed a comparison between the results from the fully non-linear and modified linear solution I, it was found that the shape of the velocity induction curves correlate well. For this reason, it is suggested to only amplify the induced velocities computed by the linear model with correction factor k_a. The solution with this correction will be referred to as modified linear solution II. The amplification factor can be derived from the 2D Actuator Disk theory. When rewriting the linear AC flow model in notation of the AD theory, the relationship between the thrust coefficient C_T and induction factor a_{lin} appears to be as following.

$$C_T = 4a_{lin} \qquad (2.23)$$

Correcting this according to the induction in the BEM theory, it requires a_{lin} to be multiplied by $(1-a)^{-1}$. This is set as the correction factor k_a for modified linear solution II and given

by Equation (2.24). In an effort to predict the power coefficient more accurately at higher tip-speed ratios, Cheng et al. [21] proposed and adopted the correction factor k_a as given by Equation (2.25) for modified linear solution III.

$$k_a = \frac{1}{1 - a} \tag{2.24}$$

$$k_a = \begin{cases} \frac{1}{1-a}, & (a \leq 0.15) \\ \frac{1}{1-a} \cdot \left(0.65 + 0.35 \cdot e^{-4.5 \cdot (a-0.15)}\right), & (a > 0.15) \end{cases} \tag{2.25}$$

Modified linear solution II for induced velocities then becomes as following.

$$w_{x,j} = \frac{1}{1 - a} \left(\sum_{i=1}^{i=N} Q_{n,i} R_{w_x,i,j} - Q_{n,j}^* + Q_{n,(N-j)}^* \right) \tag{2.26}$$

$$w_{y,j} = \frac{1}{1 - a} \left(\sum_{i=1}^{i=N} Q_{n,i} R_{w_y,i,j} \right) \tag{2.27}$$

The inclusion of the tangential loading term, a different correction factor k_a and inclination of the local elements makes modified linear solution III as described by Equations (2.28) and (2.29).

$$w_{x,j} = k_a \left(\sum_{i=1}^{i=N} Q_{n,i} R_{w_x,i,j} + \sum_{i=1}^{i=N} Q_{t,i} R_{w_y,i,j} - \left(Q_{n,N+1-j}\right)^* - \left(Q_{t,N+1-j} \frac{y_j}{\sqrt{1-y_j^2}}\right)^* \right) \tag{2.28}$$

$$w_{y,j} = k_a \left(\sum_{i=1}^{i=N} Q_{n,i} R_{w_y,i,j} - \sum_{i=1}^{i=N} Q_{t,i} R_{w_x,i,j} \right) \tag{2.29}$$

The terms marked with a $*$ in Equations (2.26) and (2.28) should only be added for the downstream half of the rotor. The term N represents the modeled amount of sections along the rotor periphery. The influence coefficients R are time independent integrals and written as given by Equations (2.30) and (2.31).

$$R_{w_x,i,j} = \int_{\theta_i - 1/2 \Delta\theta}^{\theta_i + 1/2 \Delta\theta} \frac{-\left(x_j + \sin(\theta)\right)\sin(\theta) + \left(y_j - \cos(\theta)\right)\cos(\theta)}{\left(x_j + \sin(\theta)\right)^2 + \left(y_j - \cos(\theta)\right)^2} d\theta \tag{2.30}$$

$$R_{wy,i,j} = \int_{\theta_i - 1/2\Delta\theta}^{\theta_i + 1/2\Delta\theta} \frac{-\big(x_j + \sin(\theta)\big)\cos(\theta) - \big(y_j - \cos(\theta)\big)\sin(\theta)}{\big(x_j + \sin(\theta)\big)^2 + \big(y_j - \cos(\theta)\big)^2}\, d\theta \tag{2.31}$$

The terms x_j and y_j are defined as following.

$$x_j = -\cos\big(j\Delta\varphi - \tfrac{1}{2}\Delta\varphi\big) \qquad j = 1,2,\dots,N \tag{2.32}$$

$$y_j = \sin\big(j\Delta\varphi - \tfrac{1}{2}\Delta\varphi\big) \qquad j = 1,2,\dots,N \tag{2.33}$$

2.3 Dynamics of the Flow Field in a Darrieus Rotor

The rapidly changing angle of attack and 3D swept volume of an operational VAWT introduces challenges with respect to modeling the dynamic behavior of the flow. When simulating a more realistic environment with wind shear and atmospheric turbulence, it is important to account for dynamic inflow and a delayed equilibrium. The continuously varying angle of attack and different Reynolds numbers in the flow field stresses the requirement for a well-designed dynamic stall model. The wind kinematics of an unsteady non-uniform flow field are described in Section 2.3.1, the dynamic inflow phenomenon for VAWTs is discussed in Section 2.3.2 and the concept of dynamic stall on VAWTs is explained in Section 2.3.3.

2.3.1 Unsteady Non-Uniform Flow Field

In a realistic environment, the wind field is unsteady and non-uniform. The local wind speed is effected by turbulence and wind shear, an illustration of such wind field is shown in Figure 2.13.
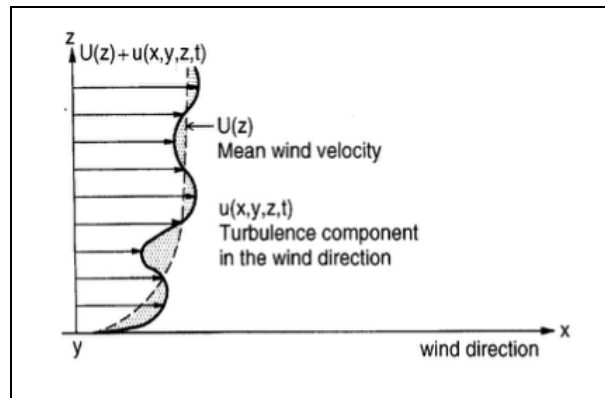
Figure 2.13: Illustration of a wind turbulence and wind shear [26]

Wind shear essentially is a variation of mean wind speed with height, and is a consequence of the flow feeling the presence or friction of the ground surface. A power law formulation can be used in order to scale the wind speed V_{ref} from a reference height z_{ref} to any desired reference height z.

$$V(z) = V_{ref} \cdot \left(\frac{z}{z_{ref}}\right)^{\alpha_{shear}} \tag{2.34}$$

The coefficient α_{shear} describes the degree of wind shear and depends on the roughness of the ground surface. Factors that influence ground surface roughness in the open sea are wave height, fetch and wave age [27]. The wind shear model that is applied in this thesis work is the

Normal Wind Profile (NWP), which specifies to use $\alpha_{shear} = 0.14$ according to the design standards of IEC61400-3 edition 1 [28].

The turbulence in a wind field describes local variations in wind speed and direction in space and time. The turbulence field is a system of vortices that vary in size and location, where the vector sum of velocities is zero in any direction. New vortices are mainly created by surface friction, but also partly by temperature effects. The friction generated turbulence covers vortices sized from $0.10 \, m$ to $500 \, m$ with a duration ranging between $1 \, s$ and $600 \, s$ [26]. The sizes of the vortices are important when considering the impact on an operational wind turbine. For example, a large vortex covers a significant part (or all) of the blade and generally causes a low-frequent variation in the local inflow. This means that a VAWT blade can feel the locally varying wind speed and direction twice on every revolution, for as long as the vortex is there. There are different analytical expressions that can describe the power spectral density of the atmospheric boundary layer [24]. One of these is the Kaimal spectrum, as given by Equation (2.35) [29].

$$S(V) = \sigma^2 \frac{4 \cdot \frac{f \cdot L}{V}}{\left(1 + 6 \cdot \frac{f \cdot L}{V}\right)^{5/3}} \tag{2.35}$$

Here the wind speed V is averaged over 10-minutes and frequency f is in Hz. The standard deviation σ relates to the amount of turbulence present in the wind field. The length scale L is set to $340.2 \, m$ for larger turbines ($z_{hub} > 60 \, m$) when applying the Normal Turbulence Model (NTM) from the IEC61400-1 standard [30]. Equivalent power spectral densities can be achieved using the formulation of e.g. the Mann turbulence model or Von Karman isotropic model.

2.3.2 Inflow Conditions for a VAWT Rotor

Dynamic Inflow

The modified linear solution of the AC flow model calculates the induced velocities shown in Equation (2.26) through (2.29). These solutions are based on a steady-state equilibrium and hence only contains time-independent terms for a given set of body forces. Due to the substantial mass flux passing through the rotor it would incorrect to assume an instant new equilibrium when the rotor loading (or body forces) are changing. For this reason, it is essential to introduce a dynamic flow model that accounts for the time delay before the induced velocities are in equilibrium with the aerodynamic loads.

As to date there is no sophisticated dynamic flow model for VAWTs, hence the flow model proposed by Larsen and Madsen [22] is taken. This dynamic flow model is originally designed to model transient aerodynamic loads during the blade pitching process for HAWTs [31], where the calculated steady-state induced velocities are low-pass filtered. More specifically, two first-order filter functions are applied in parallel that represent the near- and far-wake effect with a non-dimensional time constant τ^* of respectively 0.5 and 2.0. The weight of the near-wake filter is 0.6 and the weight of the far-wake filter is 0.4. The first-order filter can be formulated in discrete time domain as shown by Equation (2.36).

$$w_{filtered}(t_i) = w_{filtered}(t_{i-1}) \cdot e^{-\Delta t/\tau} + w_{unfiltered}(t_i) \cdot (1 - e^{-\Delta t/\tau}) \qquad (2.36)$$

The time constant τ is related to the non-dimensional time constant τ^* through rotor radius R and average wake velocity.

$$\tau = \tau^* \cdot \frac{R}{V_{wake}} \qquad (2.37)$$

Larsen and Madsen [22] suggest that improvements to this model are still to be done, especially with respect to finding the right time constants.

Curved Inflow

An additional effect of the vertical axis rotor is that the individual blade sections experience a curved inflow. This occurs due to the rotational velocity of the blades and essentially means that the angle of attack varies over the chord length. The influence of stream-curvature effects for VAWTs is covered in study by de Vries in 1979 [32]. It is found that the negative effective angle of attack is induced by stream curvature, which means more lift in the upstream blade positions and less lift in the downstream blade positions. A correction is suggested that takes the angle of attack 75% down the chord of the airfoil or $\alpha_{0.75}$, as illustrated by Figure 2.14.
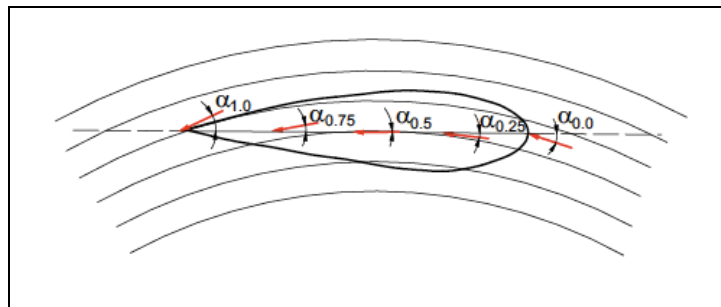
Figure 2.14: Illustration of the curved inflow on a VAWT blade element [22]

This correction is in line with the approach used HAWC2 for HAWTs, hence it is also adopted in the VAWT aerodynamic model to use $\alpha_{0.75}$. On the other hand, the aerodynamic model in the recently developed SIMO-RIFLEX-AC uses the angle of attack in the middle of the airfoil at $\alpha_{0.50}$.

2.3.3 Dynamic Stall

Dynamic stall is an effect that occurs by changing the angle of attack within a considerably small amount of time. This effect does not appear instantaneously on the aerodynamic loads, but will take place with a time delay proportional to c/V_{rel} [24]. The response of the aerodynamic load depends on whether the viscous boundary layer of the flow is attached or partly separated.

Effect of Static and Dynamic Stall

For attached flow the time delay can be estimated using the Theodorsen theory [33]. The attached flow region is shown in Figure 2.15 on the left side of the static stall angle of approximately 8°. When rapidly changing the angle of attack the lift is delayed, meaning that for a decreasing angle of attack the aerodynamic load is higher and vice versa.
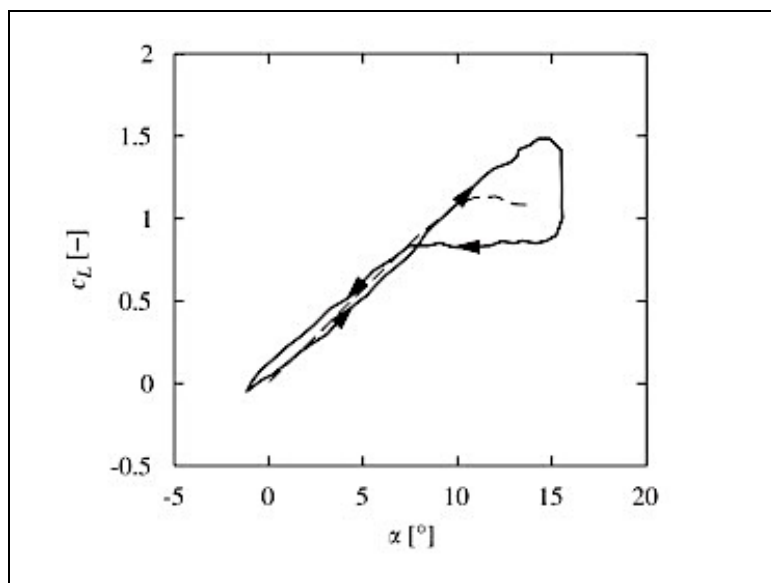
**Figure 2.15: Lift coefficient under static stall (dotted line)
and dynamic stall (continuous line) for attached flow [34]**

On the contrary, dynamic stall occurs on airfoils in detached flow conditions. For VAWTs this effect is increasingly important at lower tip-speed ratios, when the amplitude of angle of attack becomes large making the flow detach from the blade surface [14]. This means that the downstream half of the rotor is more sensitive to flow detachment, due to already being in the

unsteady wake of the upstream half. Figure 2.16 illustrates typical flow conditions around the rotor periphery of a VAWT at a tip-speed ratio of 2.14.
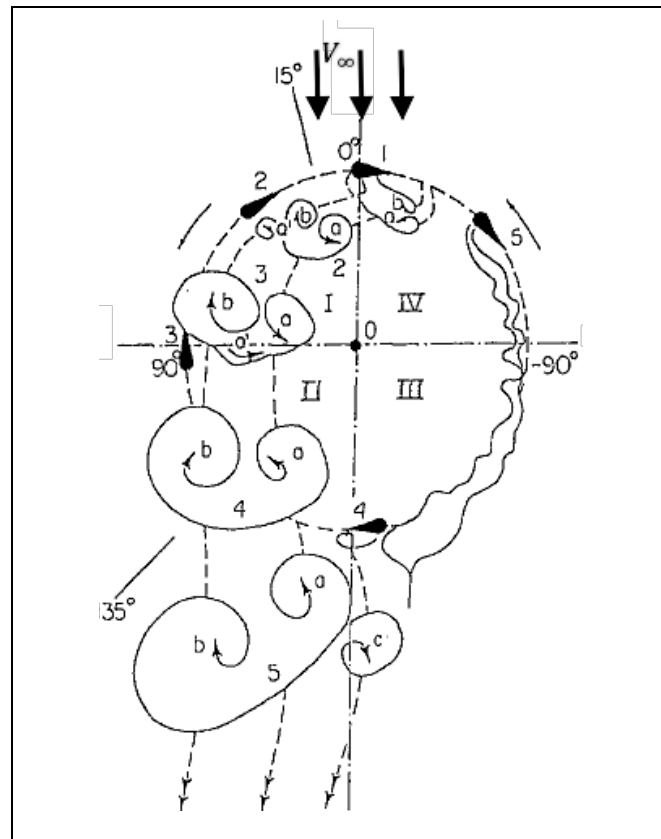
Figure 2.16: Schematic of the flow through a VAWT rotor under dynamic stall conditions at a tip-speed ratio of 2. 14, note that the freestream velocity enters at the top side [17]

When considering the delay of aerodynamic loads in dynamic stall conditions there is referred back to Figure 2.15. Dynamic stall occurs in the region on the right side of the static stall angle of 8° for this case. Opposite to the Theodorsen effect, the lift coefficient decreases significantly with a (rapidly) decreasing angle of attack.

Trailing Edge Stall

The mechanism of dynamic stall was first identified on helicopters, in which the inclusion of a dynamic stall model is essential. For the (smaller) variations of angle of attack in HAWT aerodynamics it is suggested to use at least a dynamic stall model for the lift, this is to avoid stability issues with respect to flapwise vibrations [24]. For VAWT aerodynamic load prediction it is even more important to include the effect of dynamic stall, which is also brought forward by this thesis work in Section 5.2. Under normal operating conditions the Mach number and rotational frequency are significantly lower for a wind turbine than for a helicopter,

this has lead to the development of specific dynamic stall models for wind turbines. In this thesis work the Stig Øye dynamic stall model is applied, developed by Øye in 1991 [35]. The type of stall that is included in this model is trailing edge stall, this is argued to be the most important phenomenon in terms of dynamic airfoil data [24].

Trailing edge stall starts with flow separation at the trailing edge and gradually increases upstream for increasing angles of attack. From the flow's point of view, trailing ege stall can be explained using Figure 2.17 [36]. Starting at the leading edge, the boundary layer will become turbulent at the transition point $\boxed{2}$. In case of a bubble, the boundary layer will become turbulent and reattach. At the separation point $\boxed{3}$ the flow separates from the airfoil and forms a turbulent shear layer at $\boxed{4}$. The pressure recovers in the region indicated by $\boxed{5}$ and a vortical wake is formed at $\boxed{6}$. Trailing edge stall causes lift force to drop (smoothly) at larger angles of attack.
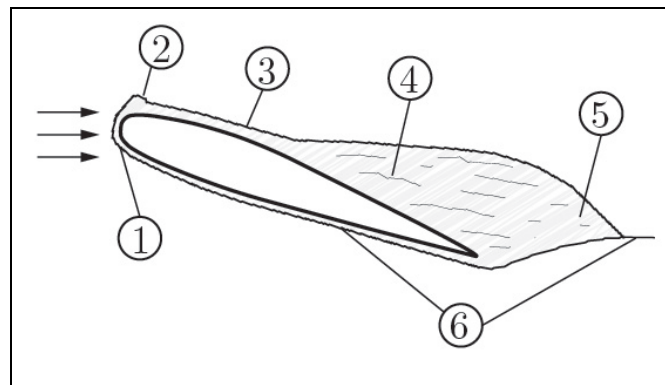
Figure 2.17: Schematic of trailing edge stall [37]

The degree of stall in trailing edge separation is described by Øye through a separation function f_s. Equation (2.38) shows how the lift coefficient under dynamic stall C_l is formulated as a function of the lift coefficient for inviscid flow without separation $C_{l,inv}$ and the lift coefficient for fully separated flow $C_{l,fs}$. Here $C_{l,inv}$ is often derived using static airfoil data in the linear region [24].

$$C_l = f_s \cdot C_{l,inv}(\alpha) + (1 - f_s) \cdot C_{l,fs}(\alpha) \tag{2.38}$$

The separation function f_s is found through a formulation of the separation function from static airfoil data and a time delay. The assumption is made that, given a sufficient amount of time, the value of the separation function f_s wil always try to get back to the static value f_s^{st} as described by Equation (2.39).

$$\frac{df_s}{dt} = \frac{f_s^{st} - f_s}{\tau} \tag{2.39}$$

This can be integrated analytically into Equation (2.40).

$$f_s(t_{i+1}) = f_s^{st} + (f_s(t_i) - f_s^{st}) \cdot e^{-\frac{\Delta t}{\tau}} \tag{2.40}$$

As mentioned previsouly, the time delay or time constant τ is approximately proportional to c/V_{rel}. Using this method the dynamic airfoil data is always 'chasing' the static airfoil data. Physically this describes the time delay that is needed for the viscous boundary layer to develop from one state to another upon a (sudden) change in the angle of attack. It should be kept in mind that the dynamic stall effect is more signficant at a higher freestream velocities. With a constant rotational speed this implies lower tip-speed ratios, and hence the amplitude of oscillation (or rate of change) of the angle of attack increases.

2.4 Wave Theory

2.4.1 Basic Potential Flow

In fluid dynamics a potential flow is described as a function of space and time by the velocity potential ϕ. The gradients of the velocity potential describes the velocity field, for example $u_x = \delta\phi/\delta x$. Hereby a characteristic is that the velocity field is irrotational. In the offshore practice it is common to assume the potential flow theory to be representative for the fluid. This means that an additional assumption of the fluid being incompressible and inviscid is made and that the Laplace equation can be satisfied. The pressure field, with respect to the ambient pressure, is described on the basis of Bernoulli's equation [38].

$$p + \rho \cdot g \cdot z + \rho \cdot \frac{\delta\phi}{\delta t} + \frac{\rho}{2} \cdot \Delta\phi \cdot \Delta\phi = 0 \tag{2.41}$$

By introducing the kinematic boundary conditions and the dynamic free-surface condition Equation (2.41) can be solved. For a velocity potential oscillating harmonically in time with a circular frequency ω, the solution at the mean sea level ($z = 0$) is as following.

$$-\omega^2 \cdot \phi + g \cdot \frac{\delta\phi}{\delta z} = 0 \tag{2.42}$$

The free-surface conditions are non-linear and can be simplified by linearizing the problem. Linear theory means that the velocity potential is proportional to the wave amplitude η_a. This is valid when the wave amplitude is small compared to the (characteristic) wavelength and the body dimensions. Higher-order wave theory is discussed afterwards in Section 2.4.3.

2.4.2 Linear Airy Wave Theory

Linear theory, often referred to as Airy wave theory, is valid until the mean sea level due to the simplifications that are made. For a propagating sinusoidal wave (component) the velocity potential can be described by Equation (2.43). This result is obtained from combining the free-surface condition with the impermeability condition at the sea bed and the Laplace equation. It should be noted that only the terms proportional to η_a are considered here.

$$\phi = \frac{g \cdot \eta_a}{\omega} \cdot \frac{\cosh\big(k \cdot (z + h)\big)}{\cosh(k \cdot h)} \cdot \cos(\omega \cdot t - k \cdot x) \tag{2.43}$$

When differentiated with respect to the horizontal or forward x-direction, the velocity field can be found. A further differentiation with respect to time results in the acceleration field according to linear theory.

$$u = \omega \cdot \eta_a \cdot \frac{\cosh(k \cdot (z + h))}{\sinh(k \cdot h)} \cdot \sin(\omega \cdot t - k \cdot x) \tag{2.44}$$

$$\dot{u} = \omega^2 \cdot \eta_a \cdot \frac{\cosh(k \cdot (z + h))}{\sinh(k \cdot h)} \cdot \cos(\omega \cdot t - k \cdot x) \tag{2.45}$$

The velocity and acceleration fields can be superimposed in order to describe the fluid flow in an irregular wave environment, which is a summation of regular waves with different phases, amplitudes and frequencies. As mentioned previously, the wave kinematics are only valid until the mean sea level. There are extrapolation methods design to compute the wave kinematics until the instantaneous surface level. Amongst these are assuming the kinematics constant above mean sea level, extrapolating the velocity/acceleration profile and (Wheeler) stretching the wave kinematics to the instantaneous surface level.

2.4.3 Second-order Stokes' Wave Theory

The second-order potential flow is found by utilizing the Stokes' expansion and essentially means that all terms up to η_a^2 are considered. As incident waves become steeper, higher-order effects become more significant. It is seen that by inclusion of the non-linear effects the wave crests are sharpened and the wave troughs are flattened [38]. The second-order wave effects can be illustrated by considering the quadratic velocity term in Bernoulli's equation.

$$\frac{\rho}{2} \cdot \Delta\phi \cdot \Delta\phi = \frac{\rho}{2} \cdot \left(\left(\frac{\delta\phi}{\delta x} \right)^2 + \left(\frac{\delta\phi}{\delta y} \right)^2 + \left(\frac{\delta\phi}{\delta z} \right)^2 \right) \tag{2.46}$$

When considering an idealized sea state consisting of two wave components oscillating with frequencies ω_1 and ω_2, the horizontal or x-component of the velocity can be written as following.

$$\frac{\delta\phi}{\delta x} = A_1 \cdot \sin(\omega_1 \cdot t + \epsilon_1) + A_2 \cdot \sin(\omega_2 \cdot t + \epsilon_2) \tag{2.47}$$

Here A_1 and A_2 describe the amplitude of the velocities based on the factors water depth, wave amplitude, wave number wave frequency and instantaneous position (see Equation (2.44)). The

ϵ represents a random phase. By considering the wave as a sum of two components the following squared velocity term is obtained and re-written.

$$\left(\frac{\delta\phi}{\delta x}\right)^2 = \frac{A_1 + A_2}{2} + \frac{A_1^2}{2} \cdot \sin(2 \cdot \omega_1 \cdot t + 2 \cdot \epsilon_1) + \frac{A_2^2}{2} \cdot \sin(2 \cdot \omega_2 \cdot t + 2 \cdot \epsilon_2)$$
$$+ A_1 A_2 \cdot \sin((\omega_1 + \omega_2) \cdot t + \epsilon_1 + \epsilon_2)$$
$$+ A_1 A_2 \cdot \sin((\omega_1 - \omega_2) \cdot t + \epsilon_1 - \epsilon_2)$$

$$(2.48)$$

In the square velocity term presented by Equation (2.54) there is three types of effects that can be recognized. The first type is the mean wave effect and corresponds to the term without an oscillatory component or $(A_1 + A_2)/2$, this is also known as Stokes' drift velocity. The second type is the sum frequency effect and corresponds to the terms oscillating with $2 \cdot \omega_1$, $2 \cdot \omega_2$ and $\omega_1 + \omega_2$. The third type is the difference frequency effect and corresponds to the last term oscillating with a frequency of $\omega_1 - \omega_2$. The latter is only present when $\omega_1 \neq \omega_2$ and introduces a slowly-varying velocity component.

It should be kept in mind that the second-order wave effects go with the square of the wave amplitude, this means that the significance is also of a lower magnitude in some situations. To illustrate this an example using a floating hemisphere – up-scaled to a $50\ m$ diameter – is given by Faltinsen [38]. The second-order horizontal drift force is found to be $10^2 \cdot \eta_a^2\ kN$, whereas the linear wave excitation force is found as $10^4 \cdot \eta_a\ kN$. Hence for a wave amplitude $\eta_a = 1\ m$ this translates to a second-order force that is 100 times smaller, but $\eta_a = 10\ m$ would translate this force being just 10 times smaller. Other than the magnitude, it is also important to note that the second-order wave theory introduces different forms of hydrodynamic loading on an offshore structure. A mean drift force can for example stress the mooring system of a floating wind turbine, whilst the sum- and difference frequency effects may excite modes that would not be excited when applying linear wave theory.

2.4.4 Statistical Behavior of Waves

Previously it is explained how the wave kinematics can be computed from given wave characteristics. This section discusses the theory behind modeling a set of harmonic components forming an irregular wave environment. The wave amplitude can be expressed by a wave spectrum.

$$\frac{1}{2}\eta_{a,j}^2 = S(\omega_j) \cdot \Delta\omega$$

$$(2.49)$$

Ocean waves are produced by wind, and when it blows for long enough a fully developed sea is reached. Based on the assumptions of a fully developed sea and anemometer measurements in the North Atlantic, the Pierson-Moskowitz (PM) spectrum was developed in 1964 and found to have the following form and constants [39].

$$S(\omega) = \frac{\alpha_{PM} \cdot g^2}{\omega^5} \cdot e^{-\beta \cdot \left(\frac{\omega_0}{\omega}\right)^4} \tag{2.50}$$

$$\alpha_{PM} = 8.1 \cdot 10^{-3} \ Hz, \qquad \beta = 0.74, \qquad \omega_0 = \frac{g}{1.026 \cdot V_{10}}$$

Later in 1973 it was discovered during the Joint North Sea Wave Observation Project (JONSWAP) that the wave spectrum is never fully developed. In order to correct for this a peak enhancement factor is introduced that would better fit the measured data on the North Sea [40]. The JONSWAP spectrum and corresponding definitions are shown in Equation (2.51).

$$S(\omega) = \frac{\alpha_{JS} \cdot g^2}{\omega^5} \cdot e^{-\frac{5}{4}\left(\frac{\omega_p}{\omega}\right)^4} \cdot \gamma^{e^{\frac{\left(\frac{\omega}{\omega_p}-1\right)^2}{2 \cdot \sigma^2}}} \tag{2.51}$$

$$\alpha_{JS} = 5.061 \cdot \frac{H_s^2}{T_p^4} \cdot (1 - 0.287 \cdot \ln(\gamma)), \qquad \omega_p = \frac{2\pi}{T_p}, \qquad \sigma = \begin{cases} 0.07 \ for \ \omega < \omega_p \\ 0.09 \ for \ \omega \geq \omega_p \end{cases}$$

The spectral and form parameter are given by α_{JS} and β, respectively. The significant wave height H_s is defined as the average of the one-third highest waves in the spectrum, whereas the peak period T_p defines at which frequency or period there is the highest energy content (peak) in the waves. The peakedness parameter γ is typically 3.3 for the North Sea. Figure 2.18 illustrates the addition that is made by Hasselmann et al. [40] in the JONSWAP spectrum.
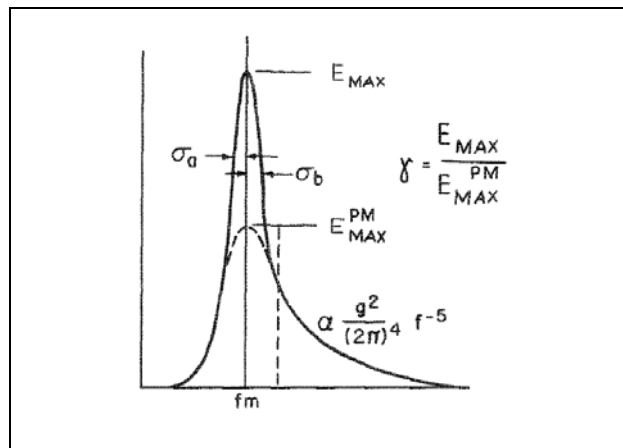
Figure 2.18: Peak enhancement in JONSWAP spectrum relative to the PM spectrum [40]

2.5 Hydrodynamic Loading

2.5.1 Potential Flow Theory

The hydrodynamic loads can be calculated by considering Bernoulli's equation for pressure in the potential flow theory. The order of terms that are considered in the pressure equation determine the accuracy of the hydrodynamic load predictions. The solution to the hydrodynamic problem can be obtained by integrating the pressure over the wetted body surface. In practice, this problem is often divided into the contributions of the incident waves and body motions on the pressure fields.

The incident waves restrain the body from moving and the pressure-contribution of this phenomenon is often referred to as the diffraction problem. The hydrodynamic loads caused by the incident waves are the wave excitation loads, these are composed of the Froude-Krylov and diffraction forces.

When the body is moving with the wave excitation frequency, the pressure field of the fluid is influenced by this. This is often referred to as the radiation problem. The effect of rigid-body motions can be described by considering the body motions in still water. When the body accelerates then waves are radiated away normal to the body's surface, this is called hydrodynamic added mass. The body's velocity induces radiation damping, which damps the motion as the name indicates. The hydrodynamic added mass and (linear) damping loads can be formulated as follows [38].

$$F_k = -\boldsymbol{A}_{kj} \cdot \frac{d^2 \eta_j}{dt^2} - \boldsymbol{B}_{kj} \cdot \frac{d\eta_j}{dt} \qquad (2.52)$$

Here $\boldsymbol{A}_{kj}$ and $\boldsymbol{B}_{kj}$ describe the added mass and (linear) damping coefficients of rigid-body motion j on the considered direction k. The coefficients are a function of the body shape, frequency of oscillation and the boundary conditions. At last there is the hydrodynamic restoring force that is an integral of the hydrostatic pressure on the body at its instantaneous position. The hydrodynamic restoring force is most significant for structures with a large water-plane area.

It should be noted that the potential flow theory is not able to compute viscous drag forces due to the assumption of an inviscid flow. Often this method is combined with the viscous drag forces as computed by the Morison equation, which is described in the next section.

2.5.2 Morison Equation

The Morison equation is a popular method for hydrodynamic load calculation due to its simplicity and efficiency. It is applicable on cylindrical elements in an oscillatory flow. This hydrodynamic model omits the effect of the body on the flow, but for slender structures ($wave\ length > 5 \cdot Diameter$) this effect is insignificant and hence the assumption of an undisturbed flow field can be justified. The Morison equation consists of two terms, being the inertial load and viscous drag load term. The inertial load is composed of the hydrodynamic added mass and Froude-Krylov force. The viscous forces describe the layer and fluid-skin friction present in the flow causing flow separation. The hydrodynamic force dF is calculated normal to the cylindrical body and is given per unit length utilizing Equation (2.53). Note that A refers to the cross-sectional area of the body and not the added mass coefficient.

$$dF = \rho \cdot A \cdot (C_m + 1) \cdot \dot{u}_w - \rho \cdot A \cdot C_m \cdot \ddot{x} + \frac{\rho \cdot D \cdot C_d}{2} \cdot (u_w - \dot{x}) \cdot |u_w - \dot{x}| \qquad \textbf{(2.53)}$$

There are three terms that can be distinguished in the Morison equation. The first represents the inertial load from water particle's acceleration $\dot{u}_w$ and is composed of the added mass term $\rho \cdot A \cdot C_m \cdot \dot{u}_w$ and the Froude-Krylov term $\rho \cdot A \cdot \dot{u}_w$. The second term describes the contribution from the body's acceleration $\ddot{x}$ on the radiation of outgoing waves. The third (non-linear) term represents the viscous drag force that is proportional to the (signed) square of the relative velocity $u_w - \dot{x}$ between the water particles and body. The added mass coefficient and drag coefficient are given by C_m and C_d, respectively. Sometimes the inertia coefficient is used in Morison's formulation, this is defines as $C_M = C_m + 1$.

2.6 Control Theory for Vertical Axis Wind Turbines

The geometry and involved aerodynamics of a vertical axis wind turbine require an alternative control approach. Theories regarding the control strategy and control algorithm are discussed in the following sections.

2.6.1 Control Strategy

In order to perform fully coupled aero-hydro-servo-elastic analyses a control strategy is required to regulate the rotor speed at all operational regions. As compared to a modern HAWT, the considered design does not have an active pitch system and hence the power output must be controlled through variable-speed operation. The *baseline* and *improved* controller will be discussed, hereafter referred to as respectively the *constant rotational speed* and *constant power* controller.

The constant rotational speed controller is developed by Merz and Svendsen [41] and recognizes two regions. The first region is before reaching maximum rotational speed Ω_{max}, in which the it aims to operate in optimal conditions or maximizing C_p. The second region considers wind speeds after reaching Ω_{max}, here the aim is to keep the rotor speed at approximately Ω_{max}. In order to obtain a maximum power coefficient in the first region, an optimum is found between the generator torque and rotor speed. The variation of the rotor-averaged generator torque against rotor speed is shown in Figure 2.19. The resulting reference rotor speed curve is presented in Section 3.3.4.
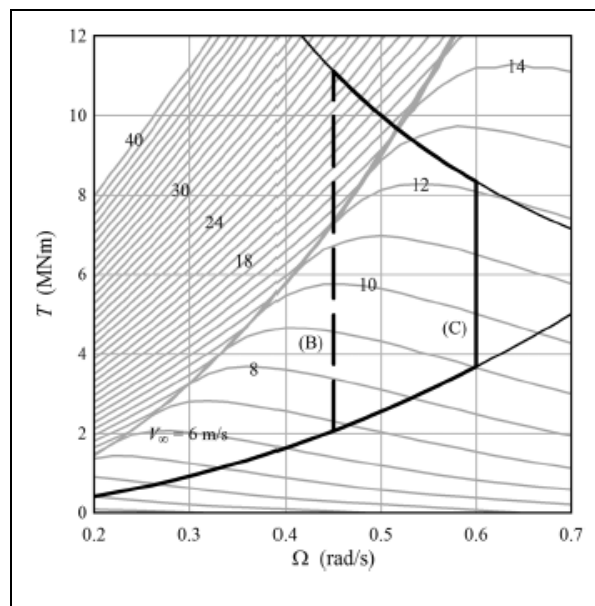
Figure 2.19: Generator torque against rotor speed, for maximizing C_p below Ω_{max} [41]

The constant power controller is designed by Cheng et al. [42] in an attempt to control the power output after rated wind speed and match the operational conditions of the NREL 5MW wind turbine. It is designed by simulating steady-wind operational conditions above rated wind speed at various (constant) rotational speeds.

2.6.2 Control Algorithm

A control strategy would be useless if there is no algorithm that can control the desired value of rotor speed. The architecture of the control algorithm is based on a proportionality-integral (PI) controller that minimizes the error between the measured rotor speed Ω_{mes} and reference rotor speed Ω_{ref}. A schematic of the the control algorithm is shown in Figure 2.20.
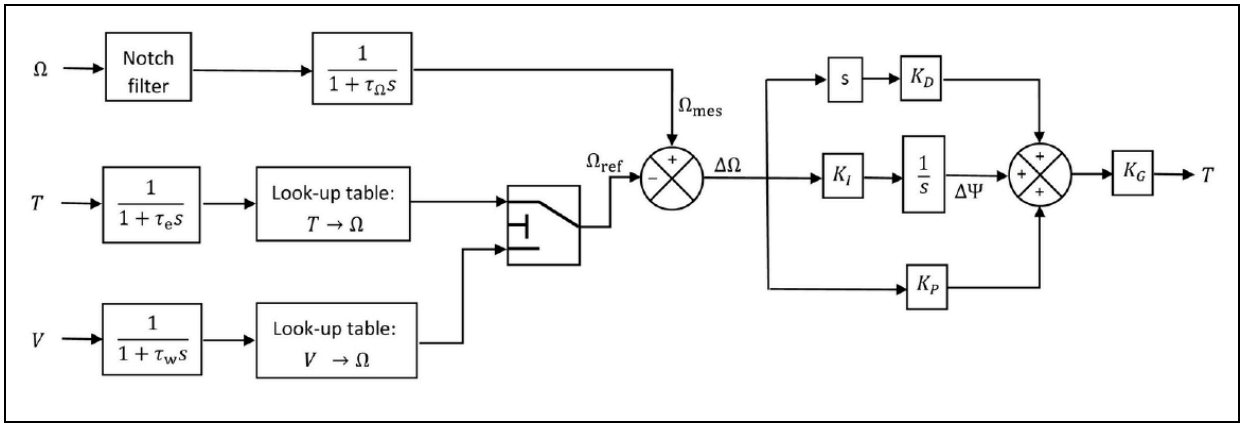
Figure 2.20: Schematic of control algorithm for a VAWT based on a PID architecture [2]

The measured rotor speed is passed through a notch filter and low-pass filter in order to take out high-frequent variations. The measured generator torque is also low-pass filtered in order to isolate the cyclic variations of aerodynamic loading. For turbulent wind conditions, the wind speed is low-pass filtered and used instead. The corresponding reference rotor speed is determined from a look-up table, such as the one for wind speed presented in Figure 3.6. The difference is then minimized by a PI controller ($K_D = 0$) and a resulting generator torque T_{gen} is then fed back into the system. The formulation of the PI controller is as follows.

$$T_{gen} = K_G \cdot \left(K_P \cdot \left(\Omega - \Omega_{ref} \right) + \int_0^t K_I \cdot \left(\Omega - \Omega_{ref} \right) dt \right) \tag{2.54}$$

Here K_G is the generator stiffness, K_P the proportionality coefficient and K_I the integral coefficient. The proportional term accounts for the present value of the error and the integral term accounts for a past value of the error. For example, an error will accumulate over time if the correction is not strong enough in the previous loops. This is recognized by the integral term and will apply a stronger correction to account for this error accumulation.

3 Methodology

Chapter 3 is devoted to the approach and methods applied in this thesis work. Starting with a short description of the site in Section 3.1, the Darrieus rotor and the spar platform are introduced in Section 3.2. This introduction includes the presentation of results from a modal analysis for the land-based VAWT and free decay test for the spar VAWT concept. Two fully coupled simulation tools HAWC2 and SIMO-RIFLEX-AC used for the dynamic analyses in this thesis work are described in Section 3.3. The comparison is done to identify differences and possible sensitivities in the codes, which are then used to formulate a logic set of load cases in Section 0.

3.1 Site Conditions

3.1.1 Introduction to the Site

The area that is considered in this study is the northern North Sea, a potential candidate for floating wind turbines off the Norwegian coast due to its large water depths. A site is selected, because then the dynamic responses of the spar VAWT can be evaluated under realistic environmental conditions. Wind-wave data is available from measurements at the semi-submersible oil platform Vestlefrikk, owned by Statoil. The oil platform has been operational since 1989 in the area west of Bergen (Norway), the location is shown in Figure 3.1.

Figure 3.1: Location of studied site [43]

Some general information about the considered site is given in Table 3.1.

Table 3.1: General information about the studied site in the northern North Sea [44]

Location	Vestlefrikk, Norway
Mean 1-hour wind speed at $10\,m$	$7.5\,m/s$
Water depth	$320\,m$

3.1.2 Correlation of the Wind-Wave Environment

Johanessen et al. [44] has performed a study on the correlation of wind-wave data at the oil platform. Measurements in the period 1973-1999 are analyzed and a joint probability density function was proposed that correlates the significant wave height H_s and peak period T_p for a given 1-hour mean wind speed at $10\,m$ reference height V_{10}. The conditional distribution of H_s for a given V_{10} is described by a set of Weibull parameters.

$$a_{shape} = 2.0 + 0.135 \cdot V_{10} \tag{3.1}$$

$$B_{scale} = 1.8 + 0.100 \cdot (V_{10})^{0.1322} \tag{3.2}$$

As indicated by the subscripts, a_{shape} and B_{scale} denote respectively the shape and scale parameters of the distribution. The conditional distribution can be used to calculate the expected value for H_s through a gamma-function as shown by Equation (3.3). The peak period T_p is estimated for a given wind speed and correlated H_s as formulated by Equation (3.4).

$$H_s = B_{scale} \cdot \Gamma(\frac{1}{a_{shape}} + 1) \tag{3.3}$$

$$T_p = (4.883 + 2.68 \cdot (H_s)^{0.529}) \cdot \left(1 - 0.19 \cdot \left(\frac{V_{10} - 1.764 + 3.426 \cdot (H_s)^{0.78}}{1.764 + 3.426 \cdot (H_s)^{0.78}}\right)\right) \tag{3.4}$$

The given joint distribution by Johannessen et al. [44] requires the mean wind speed at $10\ m$ height. This height is a common reference value in onshore and offshore engineering due to measurement instruments being installed at $10\ m$. If necessary, the mean wind speed can be scaled with respect to height using the wind shear formulation described in Section 2.3.1. As an example, a wind speed of $V_{10} = 7.5\ m/s$ would scale up to a wind speed of $V_{hub} = 10.03\ m/s$ at $79.78\ m$. In this thesis work, the hub height is defined as the vertical center of the VAWT blades and used as the reference height for wind speed.

3.2 Wind Turbine Models

The dynamic analysis performed in this study involve two wind turbine models, referred to as the land-based VAWT and spar VAWT. A description of the models is given in Sections 3.2.1 and 3.2.2, respectively. Included in the introduction of the land-based VAWT model is the results from a modal analysis, presenting the fundamental eigenmodes and corresponding eigenfrequencies of the structure. Additionally, a decay test is conducted in order to find the natural frequencies of the spar VAWT model, this is presented in the respective section.

3.2.1 Land-Based VAWT Model

Structural and Operational Properties

The land-based VAWT considered is the 5MW Darrieus rotor developed by Vita in 2007 through 2011 [3] in the DeepWind project. There are several aspects that have driven the choice of this concept, being (1) the simplicity of design, (2) possibility of using blades with Troposkien shape, (3) power extraction efficiency and (4) a relatively long track record of research and development. The baseline design comprises a rated power of 5 *MW* in order to
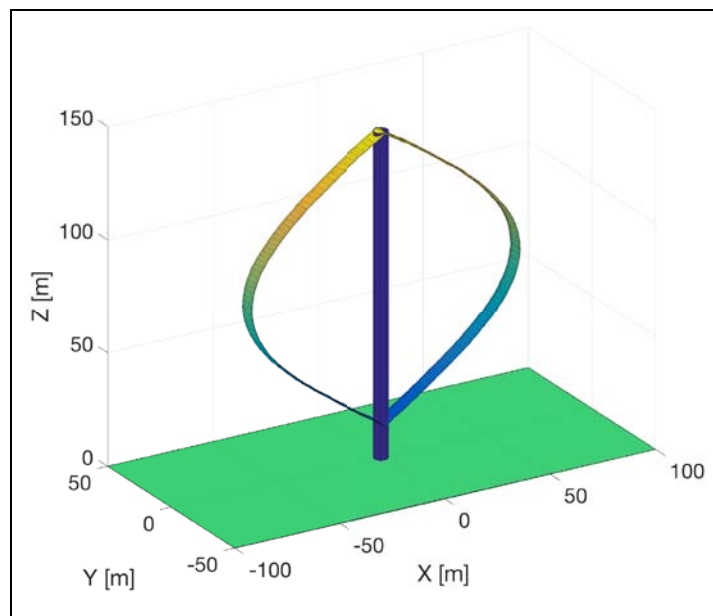
Figure 3.2: Land-based VAWT concept with DeepWind's two-bladed Darrieus rotor

compete with the market for offshore wind energy (in 2011) and allowing for comparative studies with the NREL 5MW reference turbine (HAWT). An illustration of the design is shown in Figure 3.2. It should be noted that this design is the land-based equivalent of the spar VAWT concept presented in Section 3.2.2, and not a design optimized for the onshore application.

Table 3.2: Structural properties of the two-bladed Darrieus 5MW rotor by DeepWind [3]

Rotor radius	$63.74\ m$
Hub height	$79.78\ m$
Rotor height	$129.56\ m$
Swept area	$10{,}743\ m^2$
Airfoil type	NACA0018
Chord	$7.45\ m$
Rotor mass	$305.0\ tonne$
Shaft / Tower mass	$449.2\ tonne$
Center of mass	$(0.0\ m, 0.0\ m, 75.6\ m)$

The design uses the NACA0018 airfoil due to the wide availability of data. Using this airfoil, it is found that maximum power is obtained at a rotor solidity $B\ c/R$ between 0.20 and 0.25. The solidity of the current design is 0.23. The operational conditions for the VAWT are presented in Table 3.3. It should be noted that the DeepWind rotor is designed without the inclusion of a dynamic stall model.
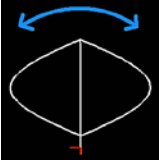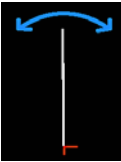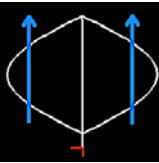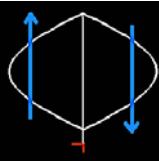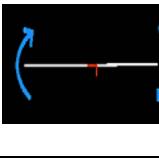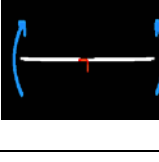
Table 3.3: Operational conditions for the two-bladed Darrieus 5MW rotor by DeepWind [3]

Rated power	$5\ MW$
Cut-in wind speed	$5\ m/s$
Cut-out wind speed	$25\ m/s$
Rated wind speed	$14\ m/s$
Maximum rotational speed	$0.551\ rad/s$ ($31.6\ deg/s$ or $0.0877\ Hz$)

Fundamental Eigenmodes from Modal Analysis

In order to learn more about the characteristics of the land-based VAWT a modal analysis is performed, revealing information about the eigenmodes and eigenfrequencies of the rotor configuration. The modal analysis is done in HAWC2 and compared against the results obtained in Riflex and Abaqus by Wang [14]. Abaqus is the most sophisticated tool for investigating the structural dynamics, hence the differences are presented using the Abaqus results as benchmark. The six fundamental eigenmodes and corresponding eigenfrequencies are presented in Table 3.4. It should be noted that for this analysis the turbine is considered without transmission and generator components and with the shaft brake engaged [45].

Table 3.4: Fundamental eigenmodes of the land-based VAWT by HAWC2, Riflex and Abaqus, the relative error (in brackets) is given with respect to the eigenfrequency computed by Abaqus

	Modeshape		Eigenfrequency [*Hz*]		
			Abaqus [14]	HAWC2	Riflex [14]
Mode 1		*Front view*	0.2074 (–)	0.2052 (-1.06%)	0.2043 (-1.49%)
Mode 2		*Side view*	0.2231 (–)	0.2221 (-0.45%)	0.2195 (-1.61%)
Mode 3		*Front view*	0.2698 (–)	0.2771 (+2.71%)	0.2683 (-0.56%)
Mode 4		*Front view*	0.2719 (–)	0.2783 (+2.35%)	0.2694 (-0.92%)
Mode 5		*Top view*	0.3420 (–)	0.3721 (+8.80%	0.3516 (+2.81%)
Mode 6		*Top view*	0.4214 (–)	0.4753 (+12.79%)	0.4276 (+1.47%)

The overview of the modal analysis results in Table 3.4 shows the first tower modes (Mode 1 and 2), the first flatwise blade modes (Mode 3 and 4) and the first lead-lag blade modes (Mode 5 and 6). The agreement between the three codes is quite good for the first four modes however, HAWC2 shows a significant difference in the natural frequencies of the lead-lag modes. This can be related to the different structural formulation that is implemented in HAWC2, as further described in Section 3.3. At last it is important to note that the modal analysis is done for non-operational conditions, hence with a stationary rotor. Centrifugal stiffening and gyroscopic effects are phenomena that occur when the blades start rotating. The centrifugal stiffening is most important for the flatwise blade modes, since the percentual increase in stiffness is much greater than for lead-lag bending [45]. On the other hand, gyroscopic effects can create significant frequency shifts with respect to the tower modes and lead-lag blade modes.

3.2.2 Spar VAWT Model

Properties of the Spar Floater

Where the land-based VAWT is assumed to be rigidly connected to the ground, the spar VAWT comprises a design with the Darrieus rotor fixed on a spar floater. The floater is based on the OC3 spar floating originally designed to support the NREL 5MW reference turbine [46]. A spar floater with heavy ballast located at the bottom provides good stability characteristics with respect to pitching and rolling motions. The mooring system consists of catenary chains with delta lines and added clump weights to resist the aerodynamic yaw moment. The mooring system provides the restoring stiffness. An illustration of the spar VAWT is shown in Figure 3.3. Additionally the definition of the mooring system is given [42].
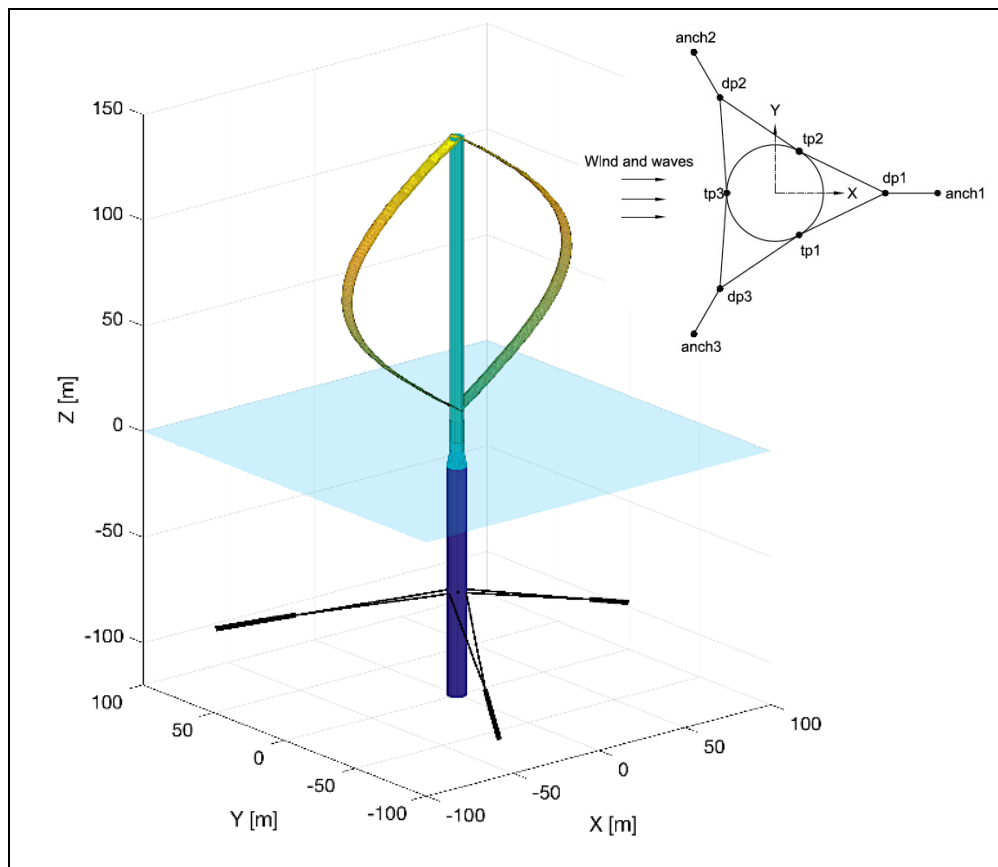
Figure 3.3: Spar VAWT concept with two-bladed Darrieus rotor

As mentioned previously, the spar floater is originally designed for a 5MW HAWT. In order to compensate for the difference in mass with the concept in Figure 3.3, the original ballast was modified by Cheng et al. [47] to maintain an equal draft and displacement with the 5MW Darrieus rotor mounted on top. A conical section is implemented between $4\,m$ and $12\,m$ below MSL in order to reduce hydrodynamic loads [46]. The properties of the modified spar floater are summarized in Table 3.5.

Table 3.5: Properties of the OC3 floater modified for the spar VAWT concept [46] [47]

Draft	$120\ m$
Diameter below taper	$9.4\ m$
Waterline diameter	$6.5\ m$
Hull mass, including ballast and generator	$7{,}308.3\ tonne$
Center of mass (floater)	$(0.0\ m,\ 0.0\ m,\ -89.8\ m)$
Displacement	$8{,}027\ m^3$
Center of buoyancy	$(0.0\ m,\ 0.0\ m,\ -62.1\ m)$
Moment of inertia in roll and pitch	$6.36 \cdot 10^7\ tonne/m^2$
Moment of inertia in yaw	$1.59 \cdot 10^5\ tonne/m^2$

Natural Frequencies from Free Decay Test

A free decay test is done to determine the natural frequencies of the platform motions. The spar VAWT is placed in an environment with virtually no wind ($V = 0.1\ m/s$) and no waves ($H_s = 0.01\ m$, $T_p = 10.0\ s$). An external force or moment is applied at the combined center of mass of the floater and rotor, located at $(0.0\ m,\ 0.0\ m,\ -74.3\ m)$ in the global coordinate system. The external force or moment is applied in the examined degree of freedom in order to give it an initial displacement. The force or moment consists of a ramp starting at $t = 50\ s$ and is then held constant until the structure is 'released'. At this moment the decay test starts and the platform motions are recorded for a sufficient amount of time to capture multiple oscillations. More specific details about the magnitude and length of the external forces and moments are summarized in Table 3.6.

Table 3.6: Input details for the free decay test of the spar VAWT

	External force	$t_{sim}\ [s]$	$t_{ramp}\ [s]$	$t_{cons}\ [s]$
Surge and Sway	$500\ kN$	1000	100	200
Heave	$6000\ kN$	600	50	100
Roll and Pitch	$48000\ kNm$	400	50	100
Yaw	$17000\ kNm$	400	50	100

Due to the symmetry of the spar VAWT, the force or moment required for realizing an initial displacement is identical for some of the platform motions. The external forces and moments are illustrated in a time series in Figure 3.4.
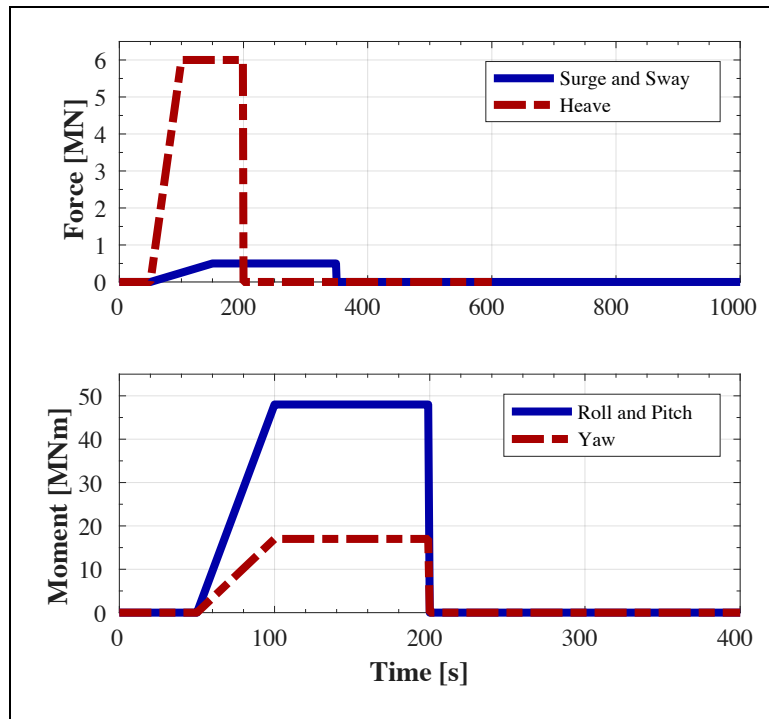
Figure 3.4: External forces and moments applied on the spar VAWT for the free decay tests

The free decay tests are conducted in the fully coupled numerical tool SIMO-RIFLEX-AC. After releasing the spar VAWT from its initial position, the motion response is analyzed to evaluate the natural period. Figure 3.5 shows the platform response of the spar VAWT. The red line indicates the rigid-body motions from time-domain simulations and the black dots represent the detected peaks. The time period in between the peaks gives the natural period of the corresponding DOF. The resulting natural periods and frequencies are summarized in Table 3.7. Due to the axisymmetric properties of the spar floater, the platform motions of sway and roll are very similar to respectively surge and roll. The natural periods in Table 3.7 are compared to the results presented by Cheng [2]. Generally, the results seem to agree well with an exception of the yaw natural period. The natural period presented by Cheng is 8.5 *s*, which is 14.5% longer than the 7.42 *s* obtained in this thesis work. This difference is unexpected since the same spar VAWT model and same numerical tool is used to conduct the free decay test. The difference may be explained by the absence of mechanical braking in the decay test presented here. Nevertheless, the order of magnitude seems correct and the absence of mechanical braking would not be relevant during operational conditions.
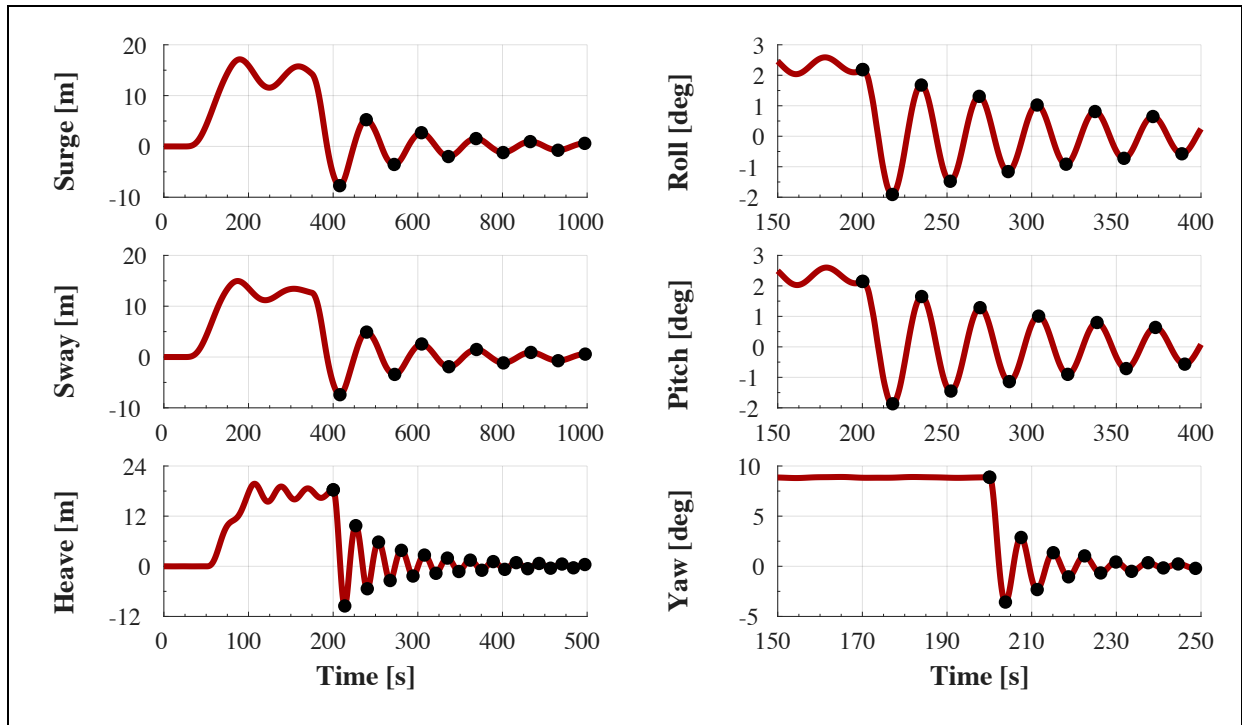
Figure 3.5: Platform motions of spar VAWT during the free decay tests

Table 3.7: Natural frequency and period of the rigid-body motions of the spar VAWT

	Natural frequency [Hz]	**Natural period [s]**
Surge	0.00775	129.0
Sway	0.00776	128.9
Heave	0.0370	27.0
Roll	0.0292	34.3
Pitch	0.0289	34.6
Yaw	0.135	7.42

3.3 Numerical Simulation Tools

The amount of publicly available simulations tools capable of performing fully coupled analyses on floating VAWTs is limited. In this thesis work two of these simulation tools are used to conduct fully coupled aero-hydro-servo-elastic analyses on the land-based and spar VAWT. The wind turbine models were presented in Section 3.2. The selected tools are the HAWC2 by DTU Wind Energy and the SIMO-RIFLEX-AC code by NTNU/MARINTEK. A description of the codes is given in the sections hereafter in which the aerodynamic, hydrodynamic, structural and control models are discussed individually.

3.3.1 Aerodynamics

Aerodynamic Model

The aerodynamic loads are calculated using the AC flow model. A set of 30 stacked cylinders is used to cover the swept volume of the two-bladed Darrieus rotor. As described in Section 2.2, a modified linear solution to the 2D flow problem has been proposed (and improved) for the implementation in aeroelastic codes. Reference has been made to the modified linear solution I, II and III. To date HAWC2 works with the modified linear solution II and SIMO-RIFLEX-AC implemented modified solution III. To recapitulate, both aerodynamic models use the modified linear solution as initially proposed by Madsen in 1982 [19]. The modified linear solutions implemented in the codes differ on the improvements that have been adopted more recently. HAWC2 corrects the induced velocities with a simple correction factor k_a (see Equation (2.24)) resulting in the induced velocities described by Equations (2.26) and (2.27). The SIMO-RIFLEX-AC code adopts the proposal by Cheng et al. [21] and accounts for the tangential loading term, inclination of blade elements and an additional correction to the induced velocities at higher tip-speed ratios. All together this results in the modified solution III given by Equations (2.28) and (2.29) and the correction factor k_a given in Equation (2.25).

Dynamic Inflow Model

The unsteady and non-uniform wind environment is modeled by the NWP and a turbulence model. The wind turbulence in HAWC2 is generated internally based on the Mann turbulence model. SIMO-RIFLEX-AC uses TurbSim [46] to generate a wind field based on the Kaimal spectrum.

The dynamic inflow is modeled using the proposed solution by Larsen and Madsen [22]. This is not a tailored solution for VAWT aerodynamics, because the dynamic inflow model is taken from HAWT aerodynamics. Nevertheless, it is used in HAWC2 and SIMO-RIFLEX-AC to

account for the delayed equilibrium between aerodynamic loads and induced velocities because a better alternative is lacking.

As the path of the VAWT rotor is curved, research has brought forward that the blade may experience a curved inflow. In order to account for this, HAWC2 takes the angle of attack at 75% of the chord or $\alpha_{0.75}$. SIMO-RIFLEX-AC does not account for curved inflow and uses the angle of attack at the midpoint of the airfoil or $\alpha_{0.50}$. It is expected that this difference causes a slight delay of loads in HAWC2. To be more precise, it corresponds to a delay of 1.67° with respect to the azimuth angle.

Dynamic Stall Model

It has become evident that a dynamic stall model is essential for an accurate prediction of aerodynamic loads. Due its significance, it is chosen to modify the Beddoes-Leishman dynamic stall model in SIMO-RIFLEX-AC such to match the Stig Øye dynamic stall model implemented in HAWC2. This means that a new set of dynamic airfoil data is used in SIMO-RIFLEX-AC and that the static airfoil data is provided for one Reynolds number only due to a limitation in HAWC2.

3.3.2 Hydrodynamics

Introducing a spar floater adds hydrodynamic loads into the system. The hydrodynamic model in HAWC2 and SIMO-RIFLEX-AC is quite different in terms of complexity. Wave kinematic in HAWC2 are computed using Airy wave theory, whereas in SIMO-RIFLEX-AC potential flow theory is applied. It was discussed in Section 2.4 that Airy wave theory is not able to model non-linear wave effects. The irregular wave climate is modeled according to the JONSWAP wave spectrum in both codes. Wheeler stretching is an option but not applied in this thesis work.

HAWC2 uses the Morison equation to calculate all hydrodynamic loading on the hull of the spar floater. The Morison equation is given by Equation (2.53) and described in Section 2.5.2. The added mass coefficient and drag coefficient used by HAWC2 are $C_m = 0.97$ and $C_d = 0.6$. The spar VAWT design contains a non-physical simplified mooring system, hence no hydrodynamic loads are acting on this. With no current present this should have a minor effect on the overall hydrodynamic loading, since wave kinematics are most significant near the water surface.

As mentioned earlier, the SIMO-RIFLEX-AC code contains a more sophisticated hydrodynamic model by combining the potential flow theory with the Morison equation. The

added mass, radiation damping and first order wave forces for the spar hull are obtained from a potential flow model. Additionally, the mean drift forces and second-order difference-frequency wave forces are also included in the hydrodynamic model for the spar VAWT. The difference-frequency forces are estimated using Newman's approximation [2]. Morison equation is applied to slender elements that are not included in the potential flow model, for the spar VAWT concept this refers to the the mooring lines. SIMO-RIFLEX-AC uses the hydrodynamic coefficients as given by Bachynski et al. [48]. Here it is proposed to use $C_m = 1.0$ and $C_d = 1.0$ for the mooring lines, the spar hull uses a C_m from the frequency-dependent potential flow results and $C_d = 0.6$.

3.3.3 Structural Dynamics

The structural formulation in HAWC2 and SIMO-RIFLEX are both based on a finite element method. HAWC2 applies the multi-body system described in Section 2.1.2. The current model of the Darrieus rotor uses 75 elements for each blade and 10 elements to model the tower. RIFLEX is the module in SIMO-RIFLEX-AC that models the blades, tower, shaft and mooring system. The structural model uses a finite element method to construct the spar VAWT as computationally efficient as possible. The blades are modeled as flexible beam elements with two symmetric planes to distinguish between the flatwise and edgewise stiffness. The tower and shaft are modeled as axisymmetric beam elements, and the mooring lines are constructed as non-linear bar elements. The spar floater is considered as a rigid body and master-slave definitions are used to connect the motions between the tower base and fairleads [14].

Structural damping is included through Rayleigh damping in both codes. The theory on Rayleigh damping is covered in Section 2.1.2. The damping model can be described by the mass- and stiffness-proportionality coefficients, which are respectively 0.0 and 0.03 in RIFLEX. This is different than in HAWC2 where the Rayleigh coefficients are specified for the individual structural components and degrees of freedom. An overview of the proportionality coefficients implemented in HAWC2 is given in Table 3.8.

The numerical integration is performed utilizing the Newmark-β method in both HAWC2 and SIMO-RIFLEX-AC. The time step is taken as $0.0025\ s$ in all types of simulations to ensure that the iterations will converge. The Newmark-β factors in HAWC2 are $\gamma = 0.51$ and $\beta = 0.256$, whilst SIMO-RIFLEX-AC utilizes $\gamma = 0.505$ and $\beta = 0.256$. The values lay close to the integration method of constant average acceleration method, which is equivalent to the Newmark-β method with constants $\gamma = 0.5$ and $\beta = 0.25$.

Table 3.8: Proportionality coefficients for Rayleigh damping in HAWC2

	Proportionality coefficient					
	M_x	M_y	M_z	K_x	K_y	K_z
Basis	0.5	0.5	0.5	0.03	0.03	0.03
Bearing	0.0	0.0	0.0	0.03	0.03	0.03
Shaft	0.0	0.0	0.0	0.003	0.003	0.003
Tower	0.0	0.0	0.0	0.003	0.003	0.003
Blades	0.0	0.0	0.0	0.0023	0.002	0.002
Spar	0.0	0.0	0.0	0.001	0.001	0.001

3.3.4 Control Dynamics

Two controller models regulating the rotor speed of a VAWT were presented in Section 2.6 with the corresponding control algorithm. A baseline controller keeps the rotational speed constant after rated wind speed, and an improved version attempts to keep the aerodynamic power constant in the higher wind speed region. Generally, the constant power controller is not used in this thesis work because it introduces sensitivities to rotor speed when comparing the VAWT models and numerical simulation tools. Nevertheless, its functionality is shortly addressed in Section 4.1.3 and the reference rotor speed curve is presented together with the curve from the constant rotational speed controller in Figure 3.6.
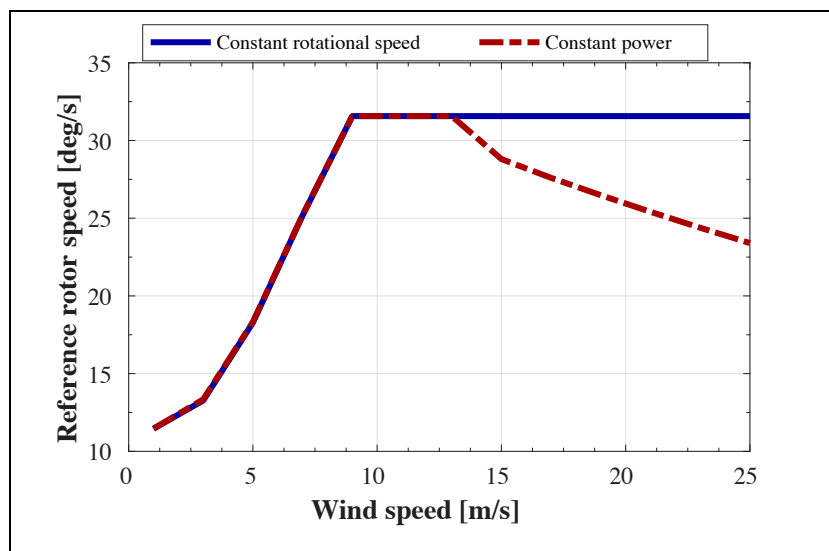
Figure 3.6: Reference rotor speed curve for the constant rotational speed and constant power controller

With reference to the control algorithm formulation in Section 2.6.2, the constants are defined as $K_G = 1.5 \ MNms/rad$, the gain values are $K_p = 0.06$ and $K_I = 0.0005$ in both codes.

3.4 Load Cases

At this point the site is introduced, the wind turbine models are presented and the numerical tools are described. This section contains the last part of the methodology in which the load cases are identified. In selecting load cases it is important to keep in mind the expected and desired output of the time-domain analyses. More details on the environmental conditions in the model comparison and code-to-code comparison are discussed in Sections 3.4.1 and 3.4.2, respectively.

3.4.1 Comparison of Land-Based VAWT and Spar VAWT

Numerical Tool Selection

In the first part of this study the land-based VAWT is compared against the spar VAWT. This is done to investigate the effect of fixing the Darrieus rotor on a spar floater and hence introducing a wave environment and floater motions to the system. With respect to numerical tool requirements, it is important that a sophisticated hydrodynamic model is available for an accurate prediction of the (added) hydrodynamic loading and platform response. Furthermore, an optimal comparison between the wind turbine models requires that numerical instabilities are at a minimum. Based on the previous requirements, the SIMO-RIFLEX-AC code is selected for conducting the fully coupled analysis in part one of this thesis work. As discussed in Section 3.3.2, the addition of potential flow theory in the hydrodynamic module SIMO is more comprehensive than only the Airy wave theory and Morison equation in HAWC2. Also, Verelst et al. [49] encountered numerical instabilities with fully coupled analysis of a spar VAWT in HAWC2. It is important to note here that the spar VAWT considered is the DeepWind concept with a rotating platform, which obviously poses complex (numerical) challenges to the structural and hydrodynamic models.

Table 3.9: General conditions that apply for the load cases in the model comparison

Simulation tool	SIMO-RIFLEX-AC
Controller	Constant rotational speed
Dynamic stall model	Yes
Structural elasticity	Flexible
Wind shear	NWP

3.4 Load Cases

General Conditions

Before presenting the load cases, there is some general conditions that are valid in all simulations of the model comparison. These are summarized in Table 3.9.

Load Case 1 to 3

Load cases should be selected to investigate variables that are expected to be influenced by the hydrodynamic loading and the platform motions of the spar VAWT. However, at first it is important to create understanding of the performance of the wind turbine models through its steady-state conditions. The load cases are presented in Table 3.10 and discussed hereafter. The value in brackets for the simulation time t_{sim} refers to the spar VAWT in case it is different from the land-based VAWT.

Table 3.10: Load cases LC1, LC2 and LC3 for the model comparison between the land-based VAWT and spar VAWT

	V_{hub} [m/s]	Turbulence	H_s [m]	T_P [s]	Seeds	t_{sim} [s]
LC1.1 – LC1.13	1,3,5,…,25	-	-	-	-	1600 (4000)
LC1.14	14	-	-	-	-	1600 (4000)
LC2.1a – LC2.1c	8	-	2.55	9.86	3	3000 (4000)
LC2.2a – LC2.2c	14	-	3.62	10.29	3	3000 (4000)
LC2.3a – LC2.3c	20	-	4.87	10.86	3	3000 (4000)
LC3.1a – LC3.1c	8	NTM	2.55	9.86	3	4000
LC3.2a – LC3.2j	14	NTM	3.62	10.29	10	4000
LC3.3a – LC3.3c	20	NTM	4.87	10.86	3	4000

Load case 1 (or LC1) considers a steady wind field only, with wind speeds ranging from 1 m/s to 25 m/s (cut-out) with intervals of 2 m/s. Also LC1.14 with rated wind speed is added. The main interest goes out to the general behavior of the VAWT aerodynamics and AC flow model. Also the power performance of the Darrieus rotor, mean offsets of the spar VAWT motions and the resulting structural loads are interesting to study and compare.

Load case 2 (LC2) adds an irregular wave environment into the system. A mild (LC2.1), medium (LC2.2) and severe (LC2.3) environment is created. Each environmental state is repeated three times using a different wave seed, the seed is denoted by the letter behind the

load case (e.g. LC2.1b). Obviously, this addition of waves only influences the spar VAWT response, which shows the intention of this load case to investigate the influence of the hydrodynamic loading. The effect of the hydrodynamic loading on the platform motions and structural loads is studied. With this the significance of the wave-induced loading is evaluated against the wind-induced loading. It is expected that mainly the standard deviations in structural loading and responses are affected by the introduction of a wave environment.

Load case 3 (LC3) represents a realistic environment with turbulent wind and irregular waves. The medium environment of LC3.2 is repeated for 10 different seeds, this is in order to study the sensitivity to the number of seeds used. However, the main addition in LC3 is the added wind turbulence which introduces a stochastic component to the wind inflow in space and time. From the equations and theories presented in Section 2.2 it is hard to tell how the Darrieus rotor responds to such highly dynamic environment. Hence first the dynamic response of the rotor and floater is studied, followed by an assessment of the aerodynamic excitation loads. The model comparison will be concluded by comparison of the internal structural loads at the blades and tower base. It is expected that LC3 will reveal the relative impact of the aerodynamic and hydrodynamic loads on the spar VAWT.

3.4.2 Comparison of HAWC2 and SIMO-RIFLEX-AC

Whereas the previous load cases were set up to study the general behavior of the VAWT and the spar platform, load cases 4 to 6 consider a comparison between two numerical tools. The models used in HAWC2 and SIMO-RIFLEX-AC to conduct fully coupled dynamic analyses on a spar VAWT were extensively described in Section 3.3. The challenge in designing a set of load cases for the code-to-code comparison lays in isolating the different models.

General Conditions

All load cases 4 to 6 consider a mild, medium and severe environment, similar to what was done in LC2 and LC3. Also, wind shear is again modeled by the NWP and the rotor speed controller by the constant rotational speed controller.

However, it is not possible to get the input conditions in HAWC2 and SIMO-RIFLEX-AC identical, as would be desired for comparative reasons. Turbulent wind and irregular waves are both stochastic phenomena that contain a factor of randomness, also referred to as the seed being used. The wind environment is generated internally by HAWC2 and externally in SIMO-RIFLEX-AC, hence it is not possible to make the stochastic event identical in both codes. The same goes for the irregular wave environment climate, where SIMO-RIFLEX-AC generates a

wave field internally through SIMO and HAWC2 uses a DLL to compute Airy wave kinematics. To conclude, the comparisons in this second part of the thesis will be limited to statistical values and power spectra. These analyses should not be affected significantly by the use of a different seed in the stochastic events.

Load Case 4 to 6

Load cases in the second part of this thesis work are designed such to isolate the different models implemented in the two codes. The resulting load cases are presented in Table 3.11 and explained afterwards.

Table 3.11: Load cases LC4, LC5 and LC6 for the code-to-code comparison between HAWC2 and SIMO-RIFLEX-AC

	V_{hub} [m/s]	H_s [m]	T_P [s]	Turbulence	Seeds	t_{sim} [s]
LC4.1 – LC4.3	8, 14, 20	-	-	-	-	1600
LC5.1	8 − 22	-	-	-	-	4000
LC6.1a – LC6.1c	8	2.55	9.86	NTM	3	4000
LC6.2a – LC6.2c	14	3.62	10.29	NTM	3	4000
LC6.3a – LC6.3c	20	4.87	10.86	NTM	3	4000

Load case 4 (LC4) simulates the land-based VAWT in a steady wind environment. The structural elasticity is set to stiff and the dynamic stall model is disabled. These steps are all taken to isolate the aerodynamic models in HAWC2 and SIMO-RIFLEX-AC to the extent that is possible. LC4 considers three different wind speeds, which allows us to compare the functionality of the aerodynamic models at a low, moderate and high tip-speed ratio.

Load case 5 (LC5) is aimed at comparing the dynamic stall model in the two codes. The original Beddoes-Leishman dynamic stall model in SIMO-RIFLEX-AC is modified to perform equally to the Stig Øye dynamic stall model in HAWC2, however this is not yet verified. A stepped wind environment is modeled in order to introduce sudden shifts in the angle of attack. The response to this sudden shift should assess the performance of the dynamic stall models. The significant effect of dynamic stall in VAWTs was already mentioned in Section 2.3.3, and LC5 provides the opportunity to show this effect in fully coupled time-domain simulations. For this purpose, LC5 is simulated with and without dynamic stall. It should be noted that the structural elasticity is also set to stiff in order to exclude the influence of the structural models.

Load case 6 (LC6) is dealt with last before concluding this thesis. Essentially it considers the same turbulent wind and irregular wave environment as presented for LC3. However, for providing a clear overview it is shown again in Table 3.11 and here with 3 seeds for LC6.2 rather than the 10 seeds for LC3.2. Also, LC6 is now implemented in the HAWC2 code and applied to the spar VAWT only. To summarize, this ultimate load case tests and compares the fully coupled aero-hydro-servo-elastic capabilities of HAWC2 and SIMO-RIFLEX-AC. As addressed previously, the results from the dynamic analyses considering LC6 can be compared on a statistical- and spectral power density level only.

4 Results and Discussion: Comparison of Land-Based VAWT and Spar VAWT

The first part of this thesis work studies the influence of mounting the two-bladed Darrieus rotor on the modified OC3 spar floater. Three load cases LC1, LC2 and LC3 are carefully designed and applied on both the land-based and spar VAWT models. Fully coupled dynamic analysis is performed using the SIMO-RIFLEX-AC code. Generally, the constant rotational speed controller and modified Beddoes-Leishman dynamic stall model is used throughout Chapter 4. The results from LC1, LC2 and LC3 are presented and extensively discussed in the respective Sections 4.1, 4.2 and 4.3.

4.1 Steady Wind of LC1: Basis for Understanding

Load case 1 contains a steady wind field that is applied on the land-based and spar VAWT in order to understand the dynamic response characteristics of a (floating) vertical axis wind turbine in steady-state conditions. The results and discussions of the dynamic analyses involving LC1 are divided into four sections. Section 4.1.1 introduces the global dynamic response of the Darrieus rotor and spar platform in transient and steady-state conditions. The aerodynamic excitation forces are compared in Section 4.1.2, and the resulting power performance of the VAWT models are analyzed in Section 4.1.3. The internal structural response in terms of bending moments at the tower base and in the blades is covered by Section 4.1.4. Generally, the dynamic analyses in LC1 considers the responses of the land-based and spar VAWT models at 14 wind speeds individually. Where necessary, a selection of the most critical or interesting results is presented.

4.1.1 Global Dynamic Response

The steady wind environment in LC1 allows for analysis of the steady-state conditions as a function of wind speed. Steady-state conditions are reached after the transient response of the rotor and platform motions are damped out, and essentially describes the stable dynamic equilibrium between the (floating) VAWT system and the environment.

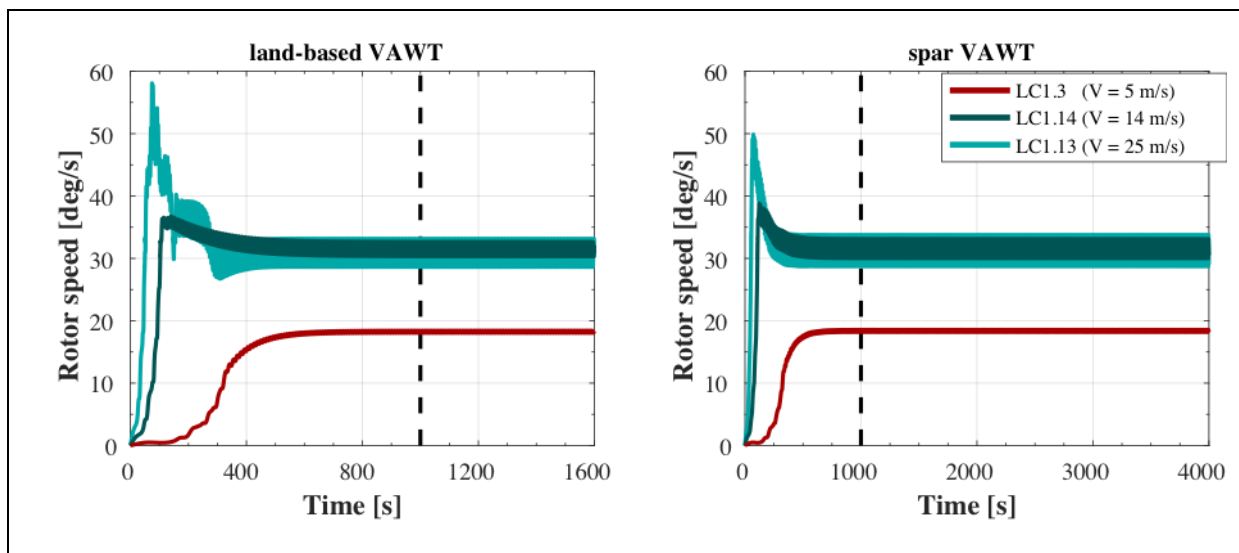**Figure 4.1: Rotor speed of the land-based and spar VAWT (LC1.3, LC1.13 and LC1.14)**

Time Series of Rotor Speed and Platform Motions

The rotor speed of the land-based and spar VAWT is presented at a low, medium and high wind speed Figure 4.1. The response shows that the Darrieus rotor takes up to $1000\ s$ to reach steady-state conditions, where the cut-in wind speed of $5\ m/s$ is most critical. It is seen that

64

the spar VAWT experiences a smoother response in the transient region with respect to rotor speed. When considering the spar VAWT it is not only the rotor that experiences start-up behavior. The floating platform is initially located where it would be for a stress-free configuration and introducing aerodynamic loads would shift the equilibrium position. The steady-state responses of the spar floater at cut-in wind speed (LC1.3) are shown in Figure 4.2. The first $500\ s$ are intentionally left out to improve the readability of the results.
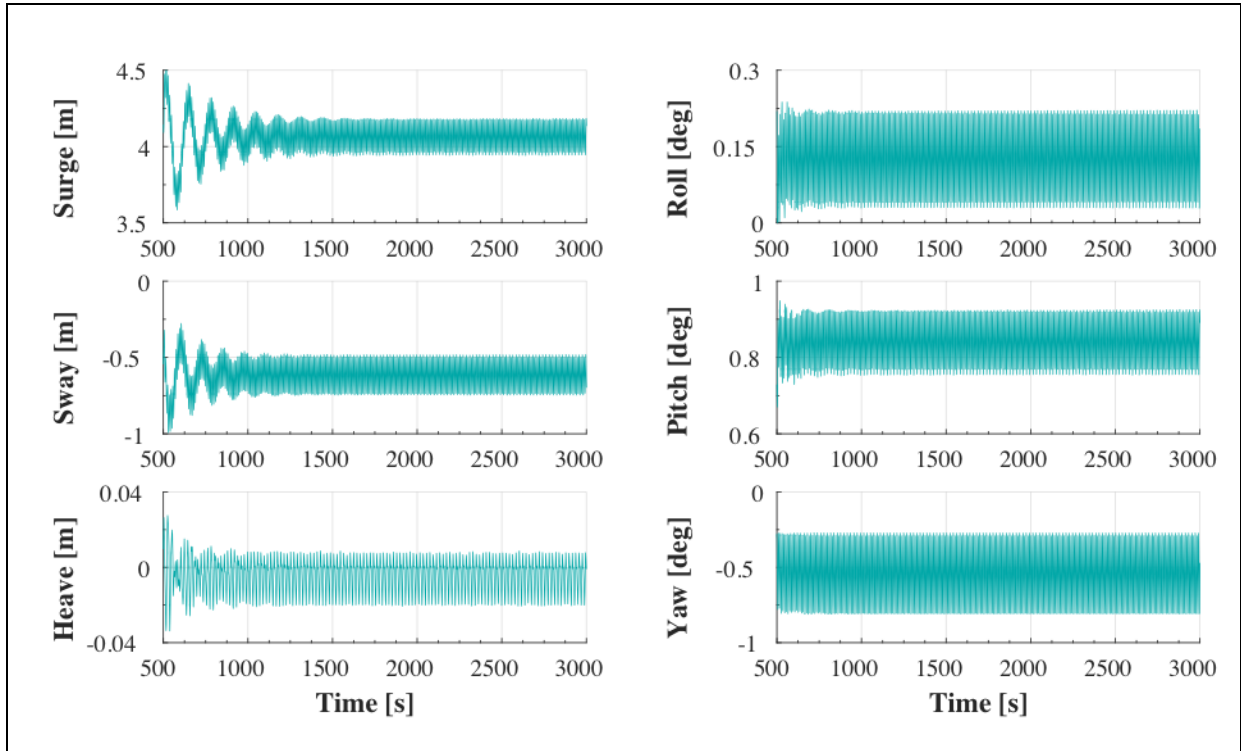
Figure 4.2: Rigid-body motions of the spar VAWT at $V_{hub} = 5\ m/s$ (LC1.3)

The platform response is found to be more critical than the rotor response for determining the transient duration. Whereas steady-state conditions of the rotational DOFs are reached at approximately $1000\ s$, the translational DOFs require a longer time period of approximately $2000\ s$. The length of the transient response is related to the natural frequency and degree of damping in the corresponding rigid-body motion. With respect to natural frequency, surge and sway have the relatively longest natural periods with $129\ s$. The heave response amplitude is small and can be related to the coupling with surge and sway.

The steady-state response can also be presented in terms of a statistical mean and standard deviation. For this reason, it is important to define the time period at which the response is analyzed. It is determined that the land-based VAWT is in steady-state after ultimately $1000\ s$, hence the last $600\ s$ can be used. For the spar VAWT it is important that not only the drivetrain, but also the platform motions are in stable equilibrium with the surroundings. Reaching steady-

state is governed by the surge and sway platform motions, and occurs ultimately at 2000 s. The exact time period that is analyzed differs per load case and is slightly shortened. This is to make sure that the analyzed time period consists of an integer number of rotational cycles. The land-based VAWT steady-state period is approximately 600 s and covers more than 50 rotational cycles. This is sufficient for statistical analysis.

Statistic Analysis of Rotor Speed and Platform Motions

The mean value and standard deviation of rotor speed are presented for both the land-based and spar VAWT in Figure 4.3. The results from the individual load cases or wind speeds are connected by a trending line.
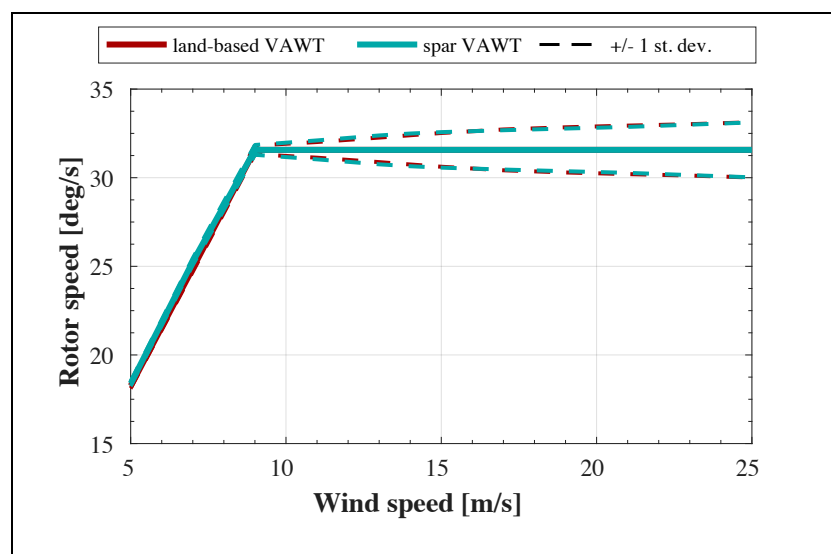
Figure 4.3: Steady-state statistics of rotor speed for the land-based and spar VAWT (LC1)

For the steady wind cases of LC1 it is seen that the mean rotor speed agrees with the implemented control strategy of the constant rotor speed controller (see Section 2.6.1). Virtually no differences are found in the statistical results of the VAWT rotor when mounted on the spar floater. The standard deviation of rotor speed increases with wind speed, up to 1.6 deg/s at the cut-out wind speed.

The platform motions of the spar VAWT are presented in a similar style in Figure 4.4. The response shows that the standard deviations are relatively small compared to the mean offsets. The mean offsets of surge, sway, pitch and yaw increase quadratically with wind speed in the optimal operational region (up to 9 m/s). Surge results in the largest mean displacement leading up to 38.9 m at the cut-out wind speed. Pitch and yaw come forward with the largest steady-state rotational offsets, up to respectively 7.5° and 10.0°. The magnitude of offsets –

especially surge and yaw – may indicate that the mooring system should be re-designed for increased stiffness. However, it is important to keep in mind that the constant rotational speed controller results in higher aerodynamic loads above rated wind speed than what the (spar) VAWT concept is designed for.
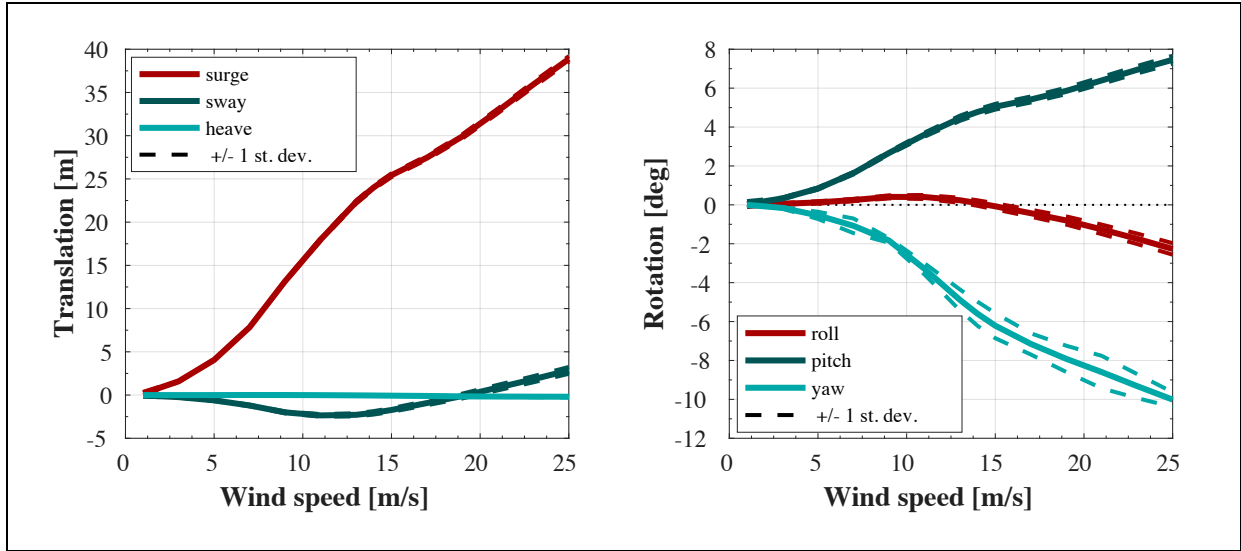
Figure 4.4: Steady-state statistics of rigid-body motions (LC1)

The coupling of motions in translational DOFs seems insignificant, the surge- and sway induced in heave is not noticeable at the scale presented here. The variation of yaw offset can be observed in the responses of all other DOFs except heave. This can be explained from a reference point of view. Whereas the wind direction is aligned with the surge DOF in the zero-stress configuration, a yaw offset rotates the reference system relative to the wind. This induces sway and roll responses from aerodynamic thrust.

Effect of Yaw Response on Rotor Speed

Figure 4.4 shows a standard deviation of the yaw response that should not be ignored. The variations in yaw are excited by generator torque and therefore indirectly influenced by variations in rotor speed. It is interesting to investigate how this yaw response relates to rotor speed with time or azimuth angle. Ultimately, the wind flow observes a rotational speed that is a summation of the rotor speed and yaw response. This is referred to as the global rotational speed Ω_G and formulated as following.

$$\Omega_G(t) = \Omega(t) + \dot{\eta}_6(t) \tag{4.1}$$

The global rotational speed Ω_G is compared to the rotor speed Ω in Figure 4.5. Time series and corresponding azimuth angles are presented at a wind speed of $21\,m/s$, where the yaw

variations are strongest. The land-based VAWT is presented by the solid lines and the spar VAWT by the dashed lines. This is the convention applied throughout all time series snapshots in which the two VAWT models are compared. It should be noted that the yaw displacement of the spar VAWT is not included in the azimuth position, because azimuth is defined in the shaft's reference system.
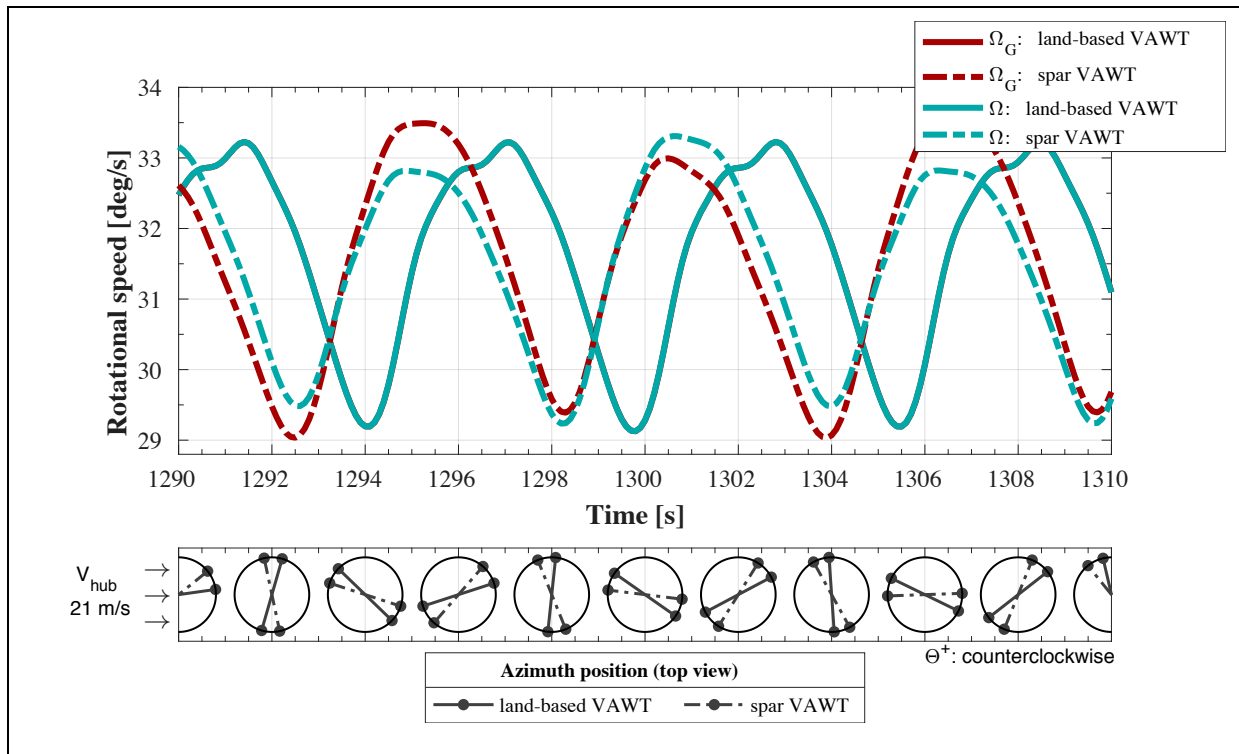
Figure 4.5: Global rotational speed for the land-based and spar VAWT in LC1.11

Obviously, the global rotational speed of the land-based VAWT is unchanged with the inclusion of yaw. It is seen that both the rotor speed and global rotational speed (thus yaw) respond at the 1P frequency. Interestingly enough it shows that the variation of rotor speed is 180° out of phase with yaw response. On another note, the flattened peaks on the rotor speed curve of the land-based VAWT are likely related to dynamic stall. Dynamic stall occurs at low tip-speed ratios, hence the combination of a high wind speed of 21 m/s and high instantaneous rotor speed may trigger this phenomenon. One can wonder why the (higher) peaks on the global rotational speed curve of the spar VAWT are not flattened, this is because dynamic stall relates to the changing rate of the angle of attack. The rate of change is likely smoothened or decreased due to the DOF in yaw, which could lead to a reduction in aerodynamic loads at high wind speeds.

4.1.2 Aerodynamic Excitation Loads

In a wind-only environment it is aerodynamic loading that causes a structural response. The excitation forces in LC1 can therefore be recognized as aerodynamic thrust and aerodynamic torque. The thrust force is parallel to the wind direction and torque is defined similarly as the rotor shaft and yaw DOF.

Understanding Rotor Speed and Torque Variations

In order to understand the variation of rotor speed and generator torque from the aerodynamic excitation, time series for the land-based VAWT is shown in Figure 4.6. The results of rotor speed, aerodynamic- and generator torque are presented at the rated wind speed of $14 \ m/s$. As a general remark, when the explanation of a certain concept does not require to show specific wind speeds or load cases, then the results at the rated wind speed are presented. This convention is used throughout Chapters 0 and 5.
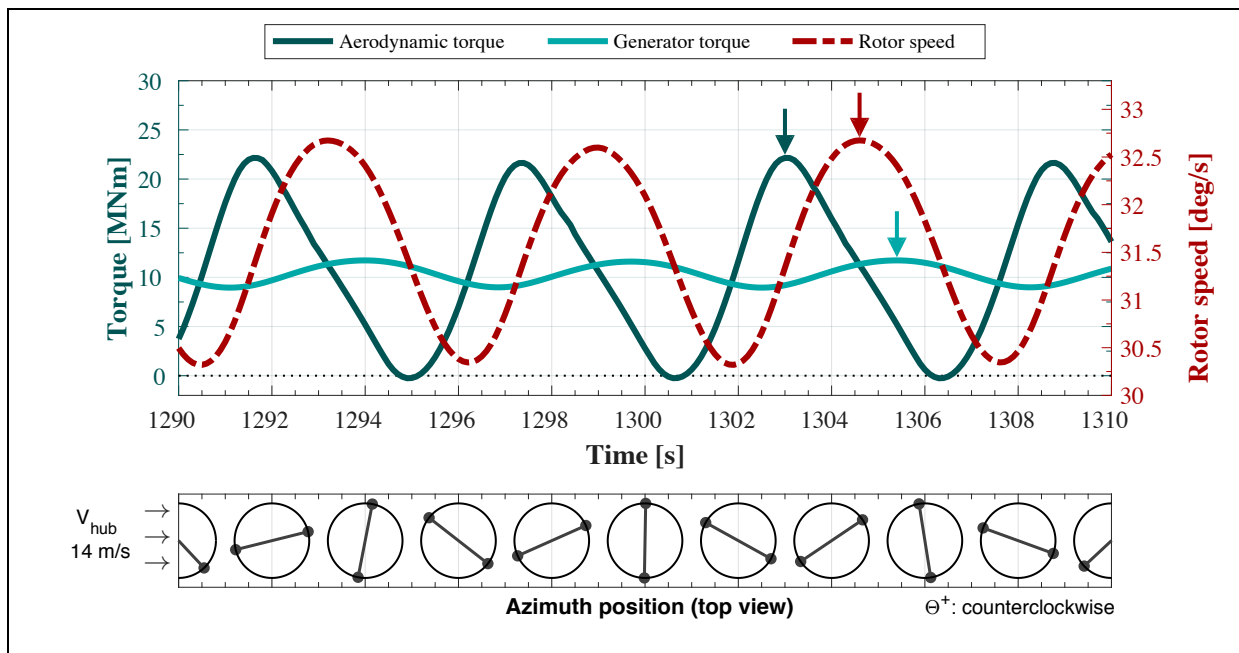
Figure 4.6: Aerodynamic torque, generator torque and rotor speed for the land-based VAWT (LC1.14)

The variation of the aerodynamic torque is a consequence of the VAWT rotor geometry and the rotor response itself. The blade path causes the angle of attack to vary from a (negative) minimum to a (positive) maximum. This induces cyclic variations in aerodynamic loads that accelerate the Darrieus rotor. The rotor inertia makes that time is needed for the rotor speed to get into a new equilibrium with the instantaneous aerodynamic loads. This results in a reduction of amplitude and introduces a lag in the rotor speed response, as illustrated by the arrows in Figure 4.6. For the generator torque this means an amplitude reduction of approximately 10

times with respect to the aerodynamic torque amplitude at rated wind speed. This indicates that a very heavy rotor would benefit the generator power output by making it nearly constant in time.

Thrust-Induced Tower Tilt

In this chapter the focus lays in understanding the global dynamic response of the spar VAWT, this means that rotor-averaged aerodynamic loads are of main interest. An effect of a mean thrust force on the spar VAWT is that it responds with a mean offset in the roll and pitch platform DOFs. In return, the mean platform offsets affect the aerodynamic loads and that is investigated in this section. The thrust force is presented against time and azimuth angle in Figure 4.7. In order to capture the most significant effect of the spar offsets, the results are shown at cut-out wind speed.
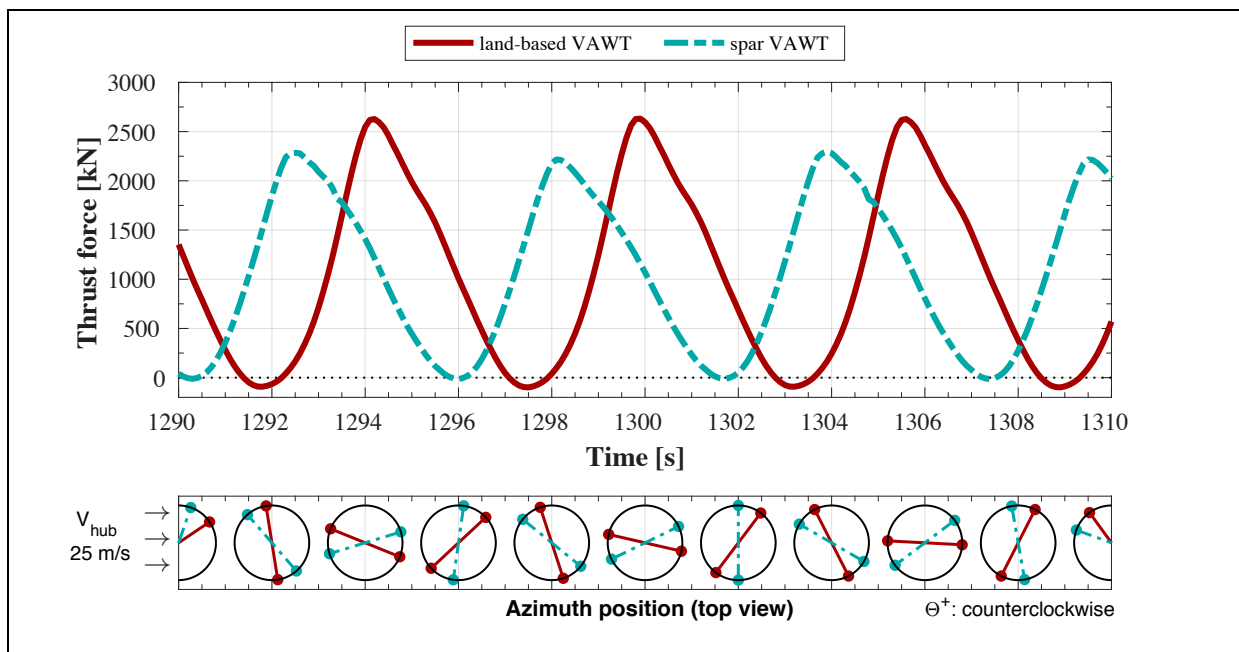
Figure 4.7: Thrust force for the land-based and spar VAWT (LC1.13)

It is interesting to observe that the thrust force maxima are notably lower for the spar VAWT. The peaks occur at an azimuth angle just under 90°. Note that the rotor thrust is given in the global coordinate system, hence a rotation of the shaft or platform reference system is not relevant for explaining the differences in Figure 4.7. Instead, the reduction of these peaks is expected to relate to both tower tilting and the yaw response. The effect of the yaw response was discussed with respect to rotor speed in Section 4.1.1.

Let us look at tower tilting. Wang et al. [18] concluded that the effect is negligible for steady tilt angles lower than 10°. The roll and pitch offsets peak at respectively $-2.3°$ and $7.5°$ when

subjected to the cut-out wind speed. In order to make a better evaluation of tower tilt the projected rotor area is investigated. The rotor area is projected in the vertical plane and normalized with rotor area. Due to the symmetry of the rotor it is only depending on the roll and pitch angles. The relationship is given by Equation (4.2), which is based on the assumption that the rotor area can be described by an ellipse.

$$\frac{A_{proj}}{A_{rot}} = \sqrt{1 - (\sin^2 \eta_4 + \sin^2 \eta_5)} \tag{4.2}$$

Figure 4.8 presents the mean normalized projected rotor area of the land-based and spar VAWT against wind speed.
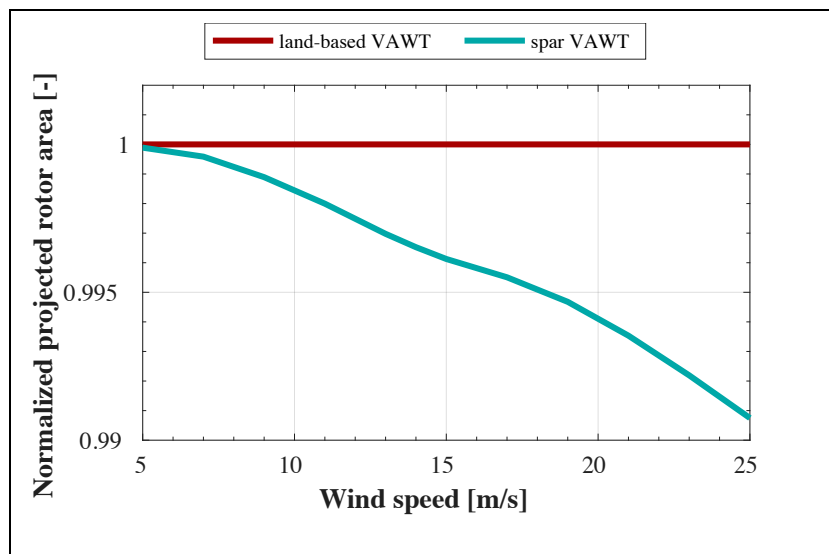
Figure 4.8: Mean normalized projected rotor area for studying the effect of tower tilt of the spar VAWT (LC1)

Obviously, the land-based VAWT shows no sensitivity to tower tilt as it is only subjected to elastic deformations. The normalized projected rotor area of the spar VAWT gradually increases with wind speed up to a maximum of approximately 0.991. There are two consequences of tower tilt on aerodynamic loading, being (1) a diminished 'wind area' captured by the rotor and (2) a different velocity component normal to the blade elements. This affected velocity component is not necessarily lower, but it is for instance reduced in the upstream area of the top half of the rotor. Here the blade elements are 'tilted' away from the inflowing wind. It should be noted that induced velocities are most significant at this rotor part due to wind shear. The aerodynamic model of SIMO-RIFLEX-AC accounts for this through local blade element inclination.

Statistic Analysis of Aerodynamic Loads

The time-averaged aerodynamic loads can be defined in both the rotor (or platform) and global reference system. The prior is interesting for analysis of structural loads such as tower base bending moments, whereas the latter is useful for assessing the global aerodynamic performance. The statistical results of thrust force and aerodynamic torque are presented against wind speed in Figure 4.9.
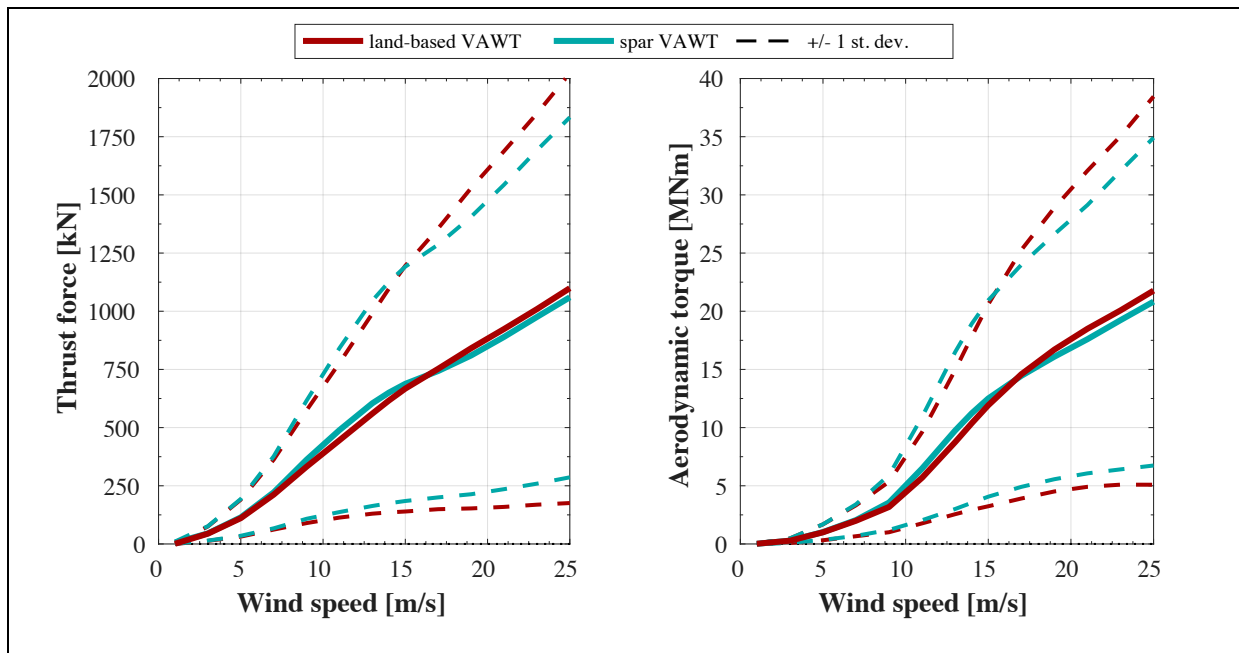
Figure 4.9: Steady-state statistics of thrust force and aerodynamic torque for the land-based and spar VAWT (LC1)

After rated wind speed the mean value (and standard deviation) of both thrust and torque is lower for the spar VAWT when compared to the land-based VAWT. In Figure 4.4 it was seen that the roll and pitch continue to increase after this wind speed. Also, the standard deviation of the yaw response becomes significant. The results generally agree well with the theories discussed previously for explaining the reduced aerodynamic loads at higher wind speeds for the spar VAWT.

Similar behavior is found in the analysis of the fore-aft rotor force, which is presented together with the side-side rotor force in Figure 4.10. As expected, the side-side rotor force has a near-zero mean at lower wind speeds. At higher wind speeds the side-side direction of the spar VAWT has a component in the streamwise direction, this is caused by the yaw offset. Figure 4.10 shows that significant standard deviations of aerodynamic loads are acting on both the side-side and fore-aft direction of the Darrieus rotor.
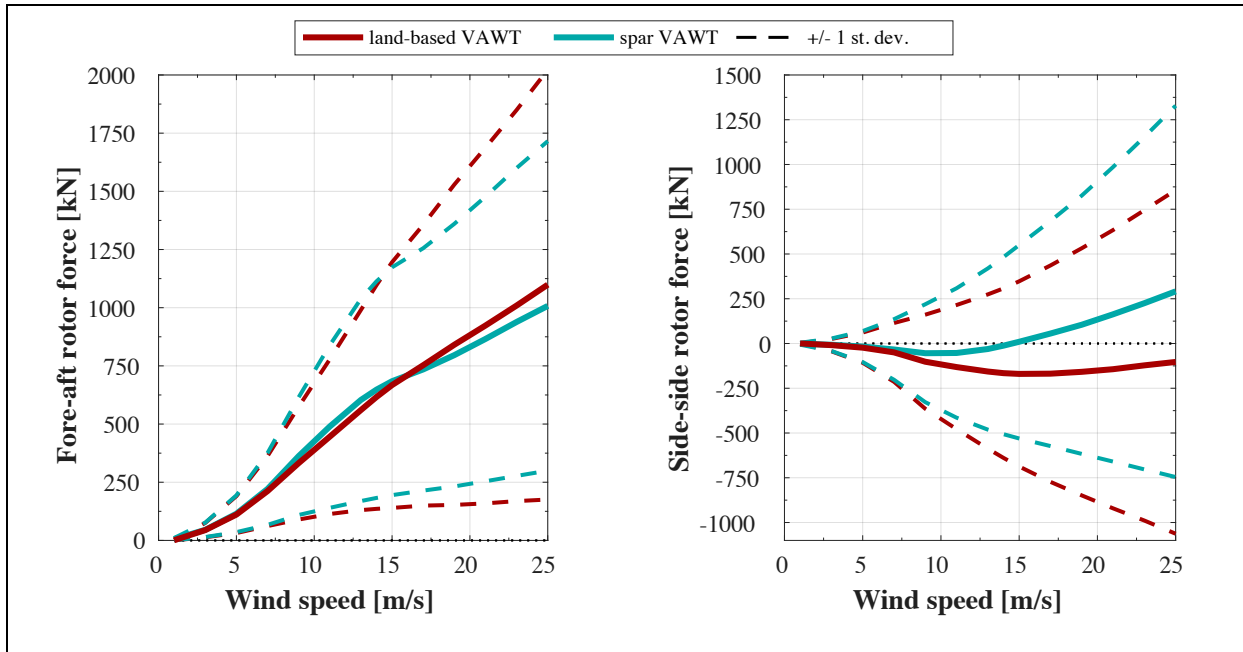
Figure 4.10: Statistical results of aerodynamic rotor forces for the land-based and spar VAWT (LC1)

4.1.3 Generator Power Performance

Response of Generator Torque and Power

The rotor speed and generator torque together form the power that the Darrieus rotor extracts from the wind flow. The actual electrical power output is also dependent on mechanical and electrical losses, although these are neglected in this study. The variation of generator torque with rotor speed was discussed previously, the resulting generator power is compared between the VAWT models in Figure 4.11. Once again, the results are presented at cut-out wind speed because the floater-induced response is most noticeable here. From the time series two observations can be made, being that (1) the generator power of the spar VAWT is lower at all azimuth angles and that (2) the spar VAWT introduces a 1P variation in the generator power response. The 1P variations is a side effect that was seen earlier in the (global) rotational speed of Figure 4.5 as well.

Interestingly enough, the additional 1P variations are not reflected by the standard deviations of generator power in Figure 4.12. The 1P variations are induced by the yaw response, and perhaps do contribute to the lower mean generator torque and power. The mean generator power is up to 4.9% lower for the spar VAWT at cut-out wind speed. Generally, the differences in generator torque and power directly relate back to the curves of aerodynamic loading in Figure 4.9.
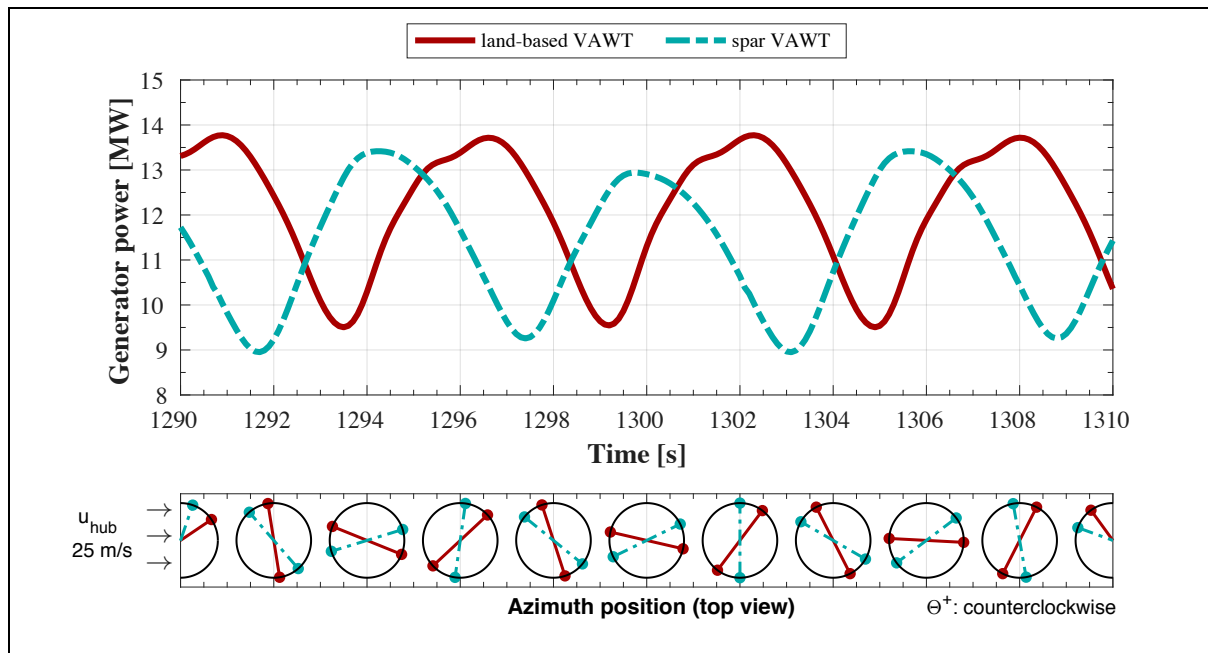
Figure 4.11: Generator power for the land-based and spar VAWT (LC1.13)

Thinking about the rated power of the VAWT studied here, one may notice that the generated power shown in Figure 4.12 significantly exceeds the design capacity. The mean value reaches up to 12 *MW*, which is a consequence of the controller that is applied here. The constant rotational speed control strategy does not fulfill the design's requirements, but is useful for comparative means.
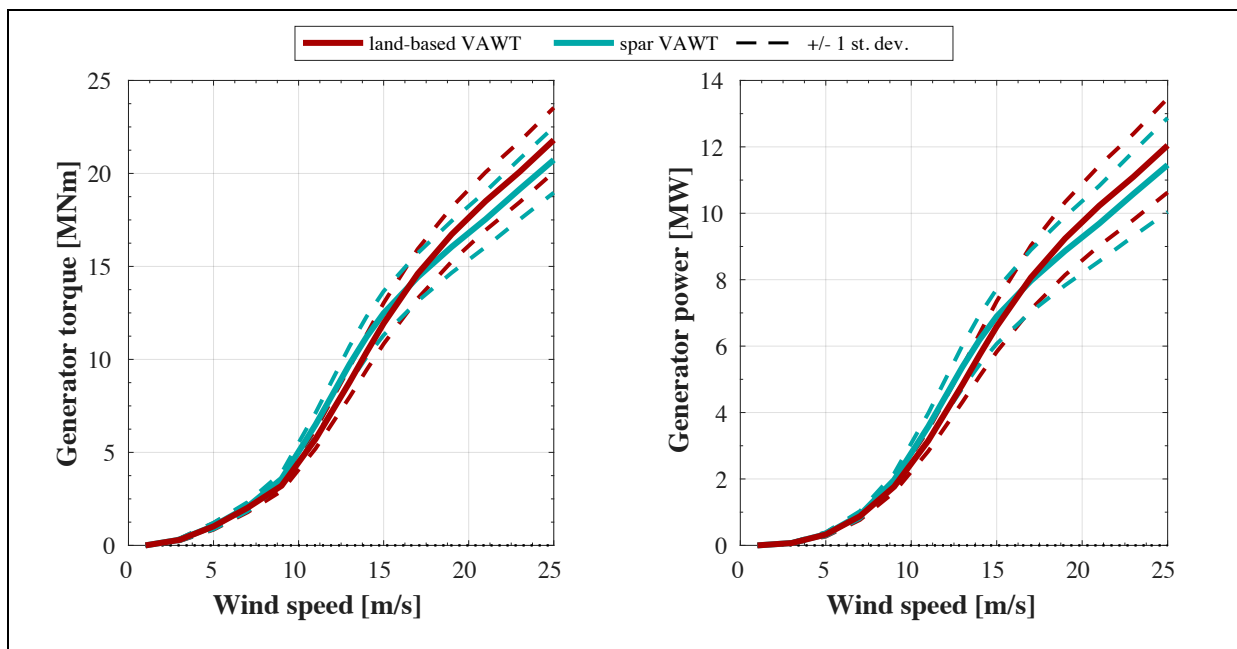
Figure 4.12: Steady-state statistics of generator torque and power for the land-based and spar VAWT (LC1)

Another effect of applying a constant rotational speed after rated wind speed is that the aerodynamic loads are larger than anticipated. This introduces large platform offsets which ultimately could mean that the differences between the land-based and spar VAWT are smaller than presented here. Also, phenomena such as dynamic stall may occur in a different fashion around the rotor periphery. Nevertheless, as mentioned previously, the constant rotational speed controller is being used for research purposes rather than simulating desirable operating conditions.

Constant Power Control

As discussed in Section 3.3.4, there is an improved controller that is designed to generate a constant power output. In the scope of creating a broad basis of understanding of the Darrieus rotor, the functionality of this improved controller is presented here. The land-based VAWT (only) is placed in the same steady wind environment of LC1. However, now the rotor speed is managed by a different control strategy. The resulting power curve is shown in Figure 4.13.
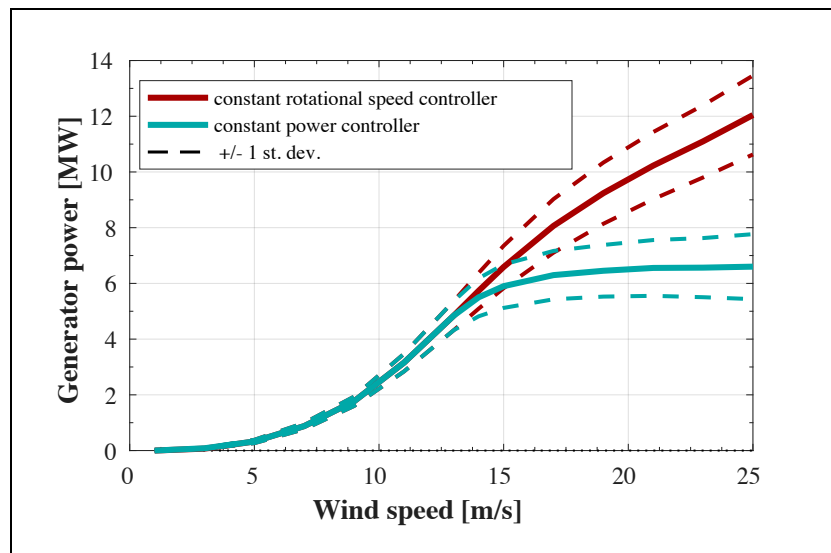

Figure 4.13: Statistical results of generator power using the constant power controller for the land-based VAWT (LC1)

The resulting power curve seems promising, as the generator power tends to a constant value above rated wind speed. The value it tends to is, however, higher than expected with a mean of 6.6 *MW*. The functionality of the controller seems stable, since the standard deviations are not (significantly) larger than for the constant rotational speed controller. The higher power output can be related to two conditions that were different in the design process of this controller. More specifically, the look-up tables of reference rotor speed are based on (1) aerodynamic loads as calculated by the DMS model and (2) the exclusion of dynamic stall. It is expected that the exclusion of dynamic stall is responsible for the larger part of the difference.

It should be noted that the controller is originally designed to deliver a constant aerodynamic power of 5.296 *MW*, similar to the NREL reference turbine [42]. At last, the power curve resulting from the constant power controller and excluding dynamic stall is shown by Figure 4.14.
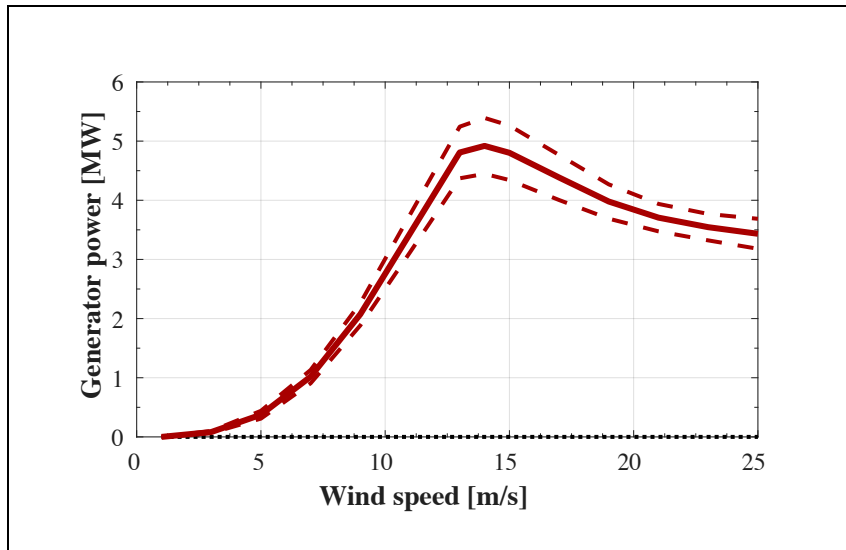
Figure 4.14: Generator power using the constant power controller and no dynamic stall for the land-based VAWT (LC1)

It can be seen that the exclusion of dynamic stall results in large shift of the power curve in this higher wind speed region. Reducing the rotor speed results in an even larger variation of angle of attack, which increases the importance of including dynamic stall in the aerodynamic load prediction of VAWTs. In general, the power curve shows a desirable trend and keeps the mean electrical power output under the 5 *MW* rated power. Despite this section on the constant power controller, it should be reminded that any further results are based on the constant rotational speed controller.

4.1.4 Internal Structural Loads

The dynamic properties of a wind turbine change when mounting it on a floating platform. This creates interest to analyze the internal structural response between the spar VAWT and its equivalent land-based VAWT. The aerodynamic excitation loads were presented in Section 4.1.2, the resulting bending moments at the tower base and mid-blade are discussed here. This is the last section and concludes the analysis of LC1.

Tower Base Bending Moments

Time series of the tower base bending moments at rated wind are presented for both VAWT models in Figure 4.15.
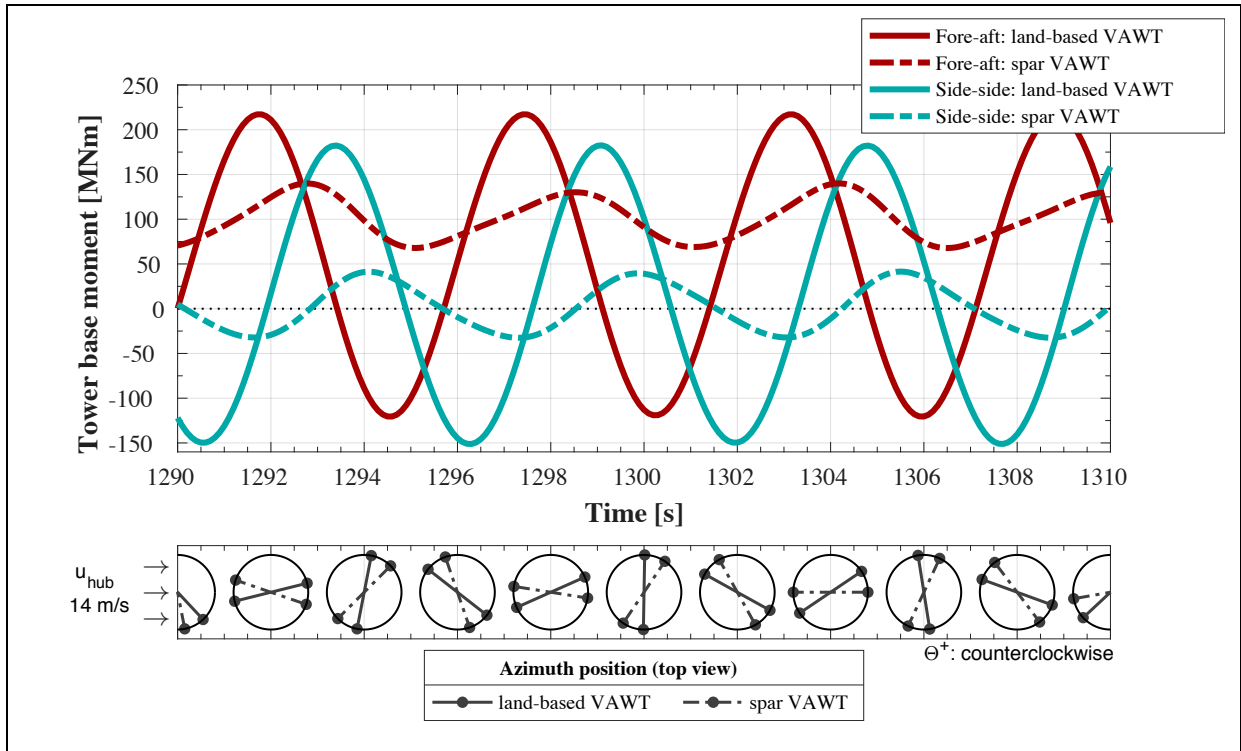
Figure 4.15: Tower base bending moments for the land-based and spar VAWT (LC1.14)

The steady-state response amplitude of both the fore-aft and side-side tower base bending moment are significant reduced for the spar VAWT. Due to the aerodynamic load variation around the rotor periphery, the fore-aft and side-side moments are approximately 90° out of phase. A 1P component is observed in the fore-aft moment of the spar VAWT, which is likely induced by the yaw response. Additionally, the spar VAWT shows a significantly higher mean value of the fore-aft tower base bending moment compared to the land-based VAWT. This shift in mean value is related to gravitational loads induced by an offset in platform pitch.

Results from statistical analysis of the tower base bending moments in the full wind speed range of LC1 are presented by Figure 4.16. The fore-aft and side-side bending moments are shown separately.

The same phenomena found for the response at rated wind speed are observed at other wind speeds too. The mean tower base bending moments of the land-based VAWT follow the trends of aerodynamic rotor forces presented in Figure 4.10. The spar VAWT is subjected to additional gravity-induced loads from platform offsets, where the additional mean fore-aft and side-side bending moments follow the trend of respectively pitch and roll (see Figure 4.4).

Figure 4.16: Statistical results of fore-aft and side-side tower base bending moments for the land-based and spar VAWT (LC1)

Regarding the standard deviation of tower base bending moments, a significant reduction is found in the tower of the spar VAWT at all wind speeds. This is because 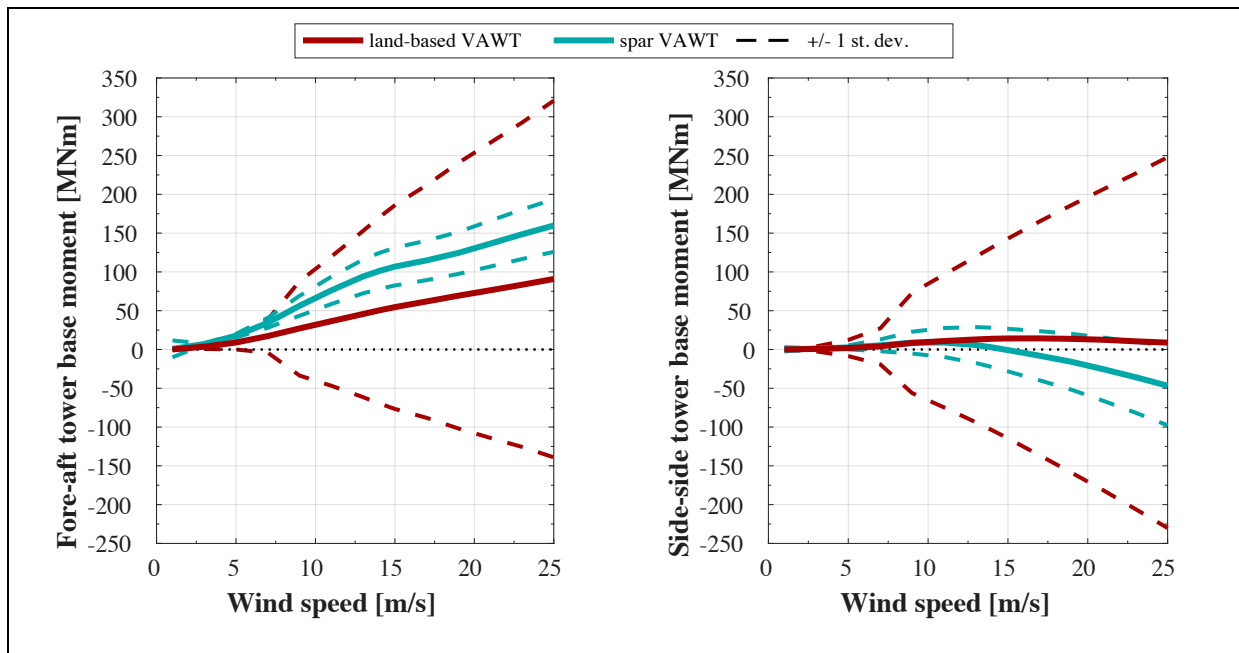the foundation below the tower of the land-based VAWT is modeled as rigid whilst the spar VAWT's 'foundation' stiffness is governed by the mooring system and hydrostatic forces (shift in metacentric height). This means that the energy from the fore-aft and side-side load cycles is mainly stored in the platform displacements for the spar VAWT, whilst it is stored in elastic deformations for the land-based VAWT. The latter is much stiffer introducing higher loads and lower displacement amplitudes. It is important to realize that this difference in stiffness also leads to a different set of eigenvalues. The first (stationary) tower modes are $0.204\ Hz$ and $0.220\ Hz$ as computed by RIFLEX, whilst the pitch and roll natural frequencies are both $0.029\ Hz$. The 2P frequency at maximum rotor speed is $0.175\ Hz$, which means that the aerodynamic rotor forces excite resonance conditions of the first tower modes (see Figure 2.2 for dynamic amplification). This explains the sudden increase of the tower-base bending moment standard deviations after the wind speed $9\ m/s$ – where maximum rotor speed is reached – for the land-based VAWT.

Mid-Blade Bending Moments

A second critical structural component of the VAWT system is the blades. In order to analyze the effect of the platform motions on the structural response, the bending moments at the mid-position of the blade are investigated. It would be interesting to compare the blade deflections as well, however, the element displacements are only available in the global coordinate system.

Tracing the global displacements back to local deformations is a tricky process (through floater displacement, azimuth position and tower deformations) and would lead to an unreliable estimate, hence it is excluded from this comparison.

The flatwise and lead-lag bending moments at the mid-blade are presented as time series in Figure 4.17. Please note that for the considered symmetrical airfoil the flatwise and lead-lag directions are equivalent to the flapwise and edgewise directions, respectively.
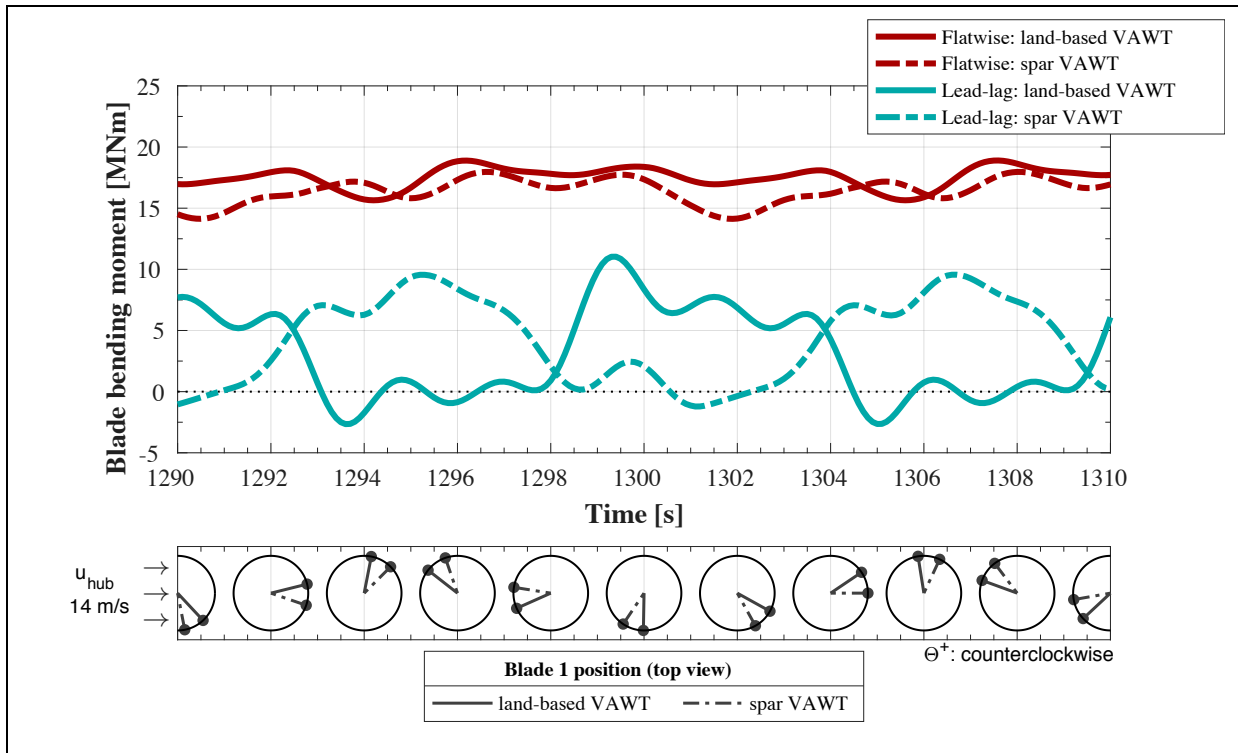
Figure 4.17: Time series of mid-blade bending moments for the land-based and spar VAWT (LC1.14)

The variations of the bending moments at the mid-position of blade 1 are very different than the regular 2P variations in the responses presented earlier in this chapter. The structural properties play an important role in the response of a lengthy Darrieus blade subjected to the (high) aerodynamic loading. This means that it is likely that one or more eigenmodes of the blades are excited. The individual blades are exposed to 1P loads, which dominates the response shown in Figure 4.17.

The statistical mean and standard deviation of the two bending moments are presented in Figure 4.18. First a general understanding of the flatwise and lead-lag responses is formed, this is followed by comparing the differences between the responses of the land-based and spar VAWT blade.
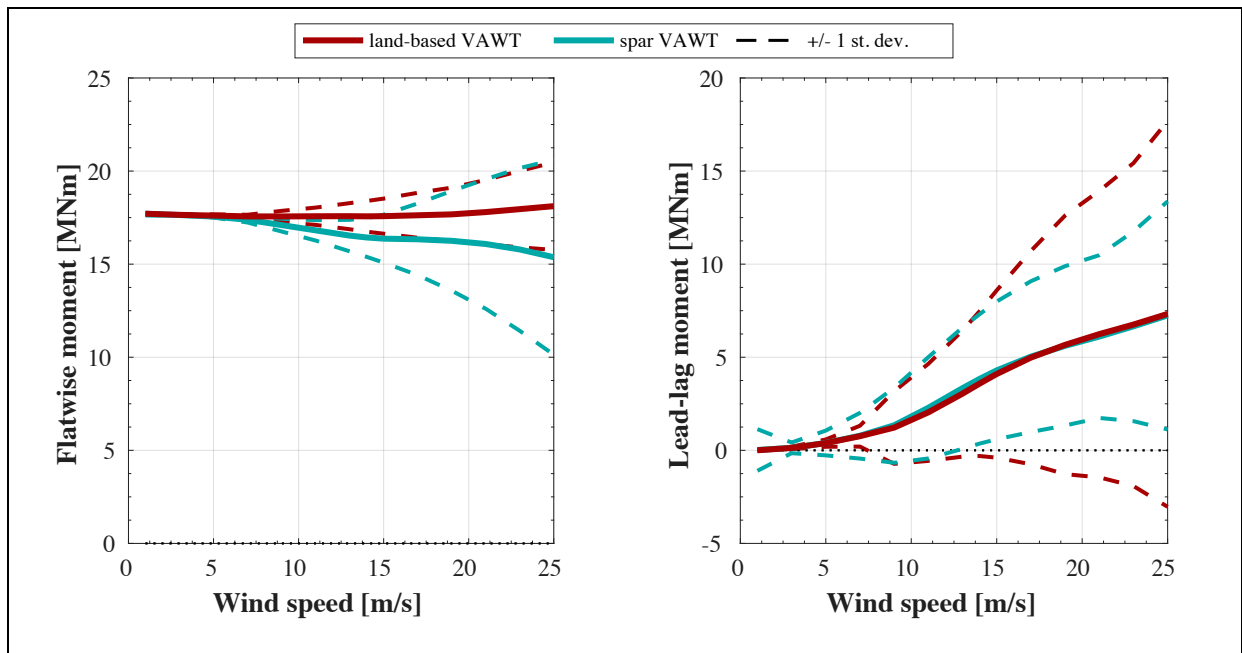
Figure 4.18: Statistics of mid-blade bending moments for the land-based and spar VAWT (LC1)

The mean flatwise moment remains fairly constant with change in mean wind speed. At the higher wind speed region, a slight increase is found for the land-based VAWT. This indicates that the mean flatwise moment is governed by its self-weight and that a smaller component is caused by aerodynamic loading. The standard deviation seems to be a result of both the aerodynamic normal force (1P) and one or several blade modes, as depicted by Figure 4.17. The flatwise response induced by centrifugal forces is likely negligible due to the (modified) Troposkien blade shape, because no trend gives this indication at lower rotor (or wind) speeds.

The magnitude of lead-lag moments is lower than the flatwise moments, and seems to be governed by the aerodynamic tangential loads (or aerodynamic torque). When the VAWT is upright, there is no gravitational components in the lead-lag moments. The general trends follow that of the aerodynamic torque (see Figure 4.9). Additionally, a sudden increase in standard deviation – such as for the tower base bending moments – is found for the lead-lag moments in the maximum rotor speed region. The first lead-lag modes correspond to mode 5 and 6 presented in Table 3.4, with eigenfrequencies of 0.351 *Hz* and 0.428 *Hz* as computed by RIFLEX at stationary conditions. With limited damping present in the blades this possibly points to resonance in the lead-lag response. In analysis of the internal structural response at LC2 the power spectra are presented, hence this will tell us more about the energy content at different frequencies.

Now that a better comprehension of the blade structural response is formed, there is good basis to compare the mid-blade bending moments of the land-based and spar VAWT. It was seen earlier that significant platform offsets take place at higher wind speeds, this causes that gravitational loads are transferred differently through the VAWT structure. This effect of is noticeable in both the mean value and standard deviation of the flatwise bending moment. The standard deviation of the lead-lag bending moment is likely reduced by the introduction of the yaw DOF for the spar VAWT.

4.2 Steady Wind and Irregular Waves of LC2: Wave-Induced Response

Load case 2 consists of a steady wind environment with an irregular wave environment correlated to the mean wind speed. Three different cases are considered with a low wind speed of $8\ m/s$ (LC2.1), rated wind speed (LC2.2) and high wind speed of $20\ m/s$ (LC2.3). The correlated wave environments are each computed for three different seeds. The statistical accuracy of using three seeds is studied in Section 4.3 for LC3.

The results considering LC2 focus on the addition of an irregular wave environment, and hence only influences the spar VAWT with respect to LC1. The explanations that relate to general VAWT phenomena are kept to a minimum here, the basis of understanding was formed through the (steady) wind-only environment in Section 4.1. Many output parameters can be presented for describing the dynamic response of the spar VAWT, but the following sections will only present results that are relevant and interesting to the studied subject. For LC2 this means that the addition of waves – presented in Section 4.2.1 – is studied through the global dynamic response (Section 4.2.2) and the internal structural loads (Section 4.2.3) only.

4.2.1 Describing the Irregular Wave Environment

In order to understand the influence of the waves on the dynamic responses it is important to describe the wave environment in more detail. Time series of the wave elevation at LC2 (seed a) are shown in Figure 4.19. The wave environment is characterized with a mean elevation of $0\ m$, whereas the (rate) of variation describes the severity of the sea state.
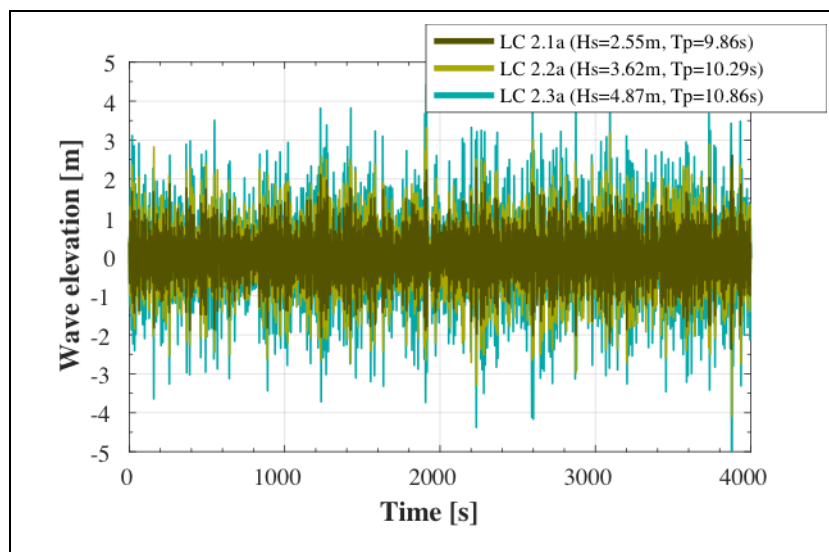

Figure 4.19: Time series of wave elevation in LC2.1a, LC2.2a and LC2.3a

Generally, the power spectral density of a time series describes the distribution of power as function of frequency. This is also referred to as *PSD* or simply *power spectrum*. The 'power' here is not a physical power, but its magnitude relates to the amount of energy that is present in the analyzed signal at the corresponding frequency. It is useful for distinguishing between the frequency content of time-varying responses such as the many presented in this thesis. The power spectrum of wave elevation is shown in Figure 4.20. Here the results of the different seeds are combined into one power spectral density.
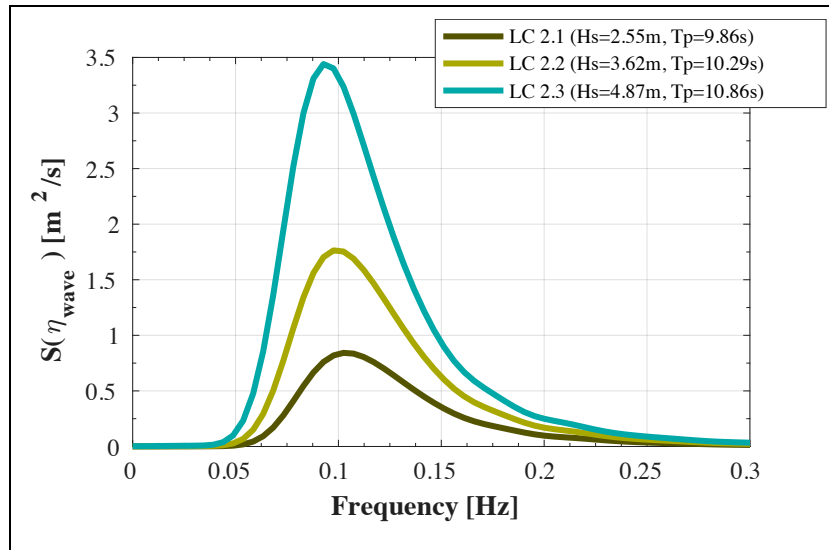
Figure 4.20: PSD of wave elevation in LC2

The energy content of the wave elevation grows with significant wave height H_s. The peak period T_p describes where peak of the spectrum is located, for the load cases considered this is all around approximately $0.10\ Hz$. Generally, energy content in the wave elevation stretches from approximately $0.05\ Hz$ to $0.25\ Hz$. In power spectral analysis of for instance the tower base bending moments it is expected that the hydrodynamic load spectrum will show. The spectra presented here are from the wave elevation time series, but are taken as representative for the wave-induced hydrodynamic loads. This is because first-order wave loads are proportional to the wave amplitude.

4.2.2 Global Dynamic Response

Time Series of Rotor Speed and Platform Motions

The environmental conditions have changed with respect to LC1. Waves are added to the system and the mildest load case has a wind speed of $8\ m/s$. This means that a different transient duration is expected, which is shortly analyzed by means of rotor speed and the

platform response. Time series of rotor speed at the governing load case is shown in Figure 4.21.
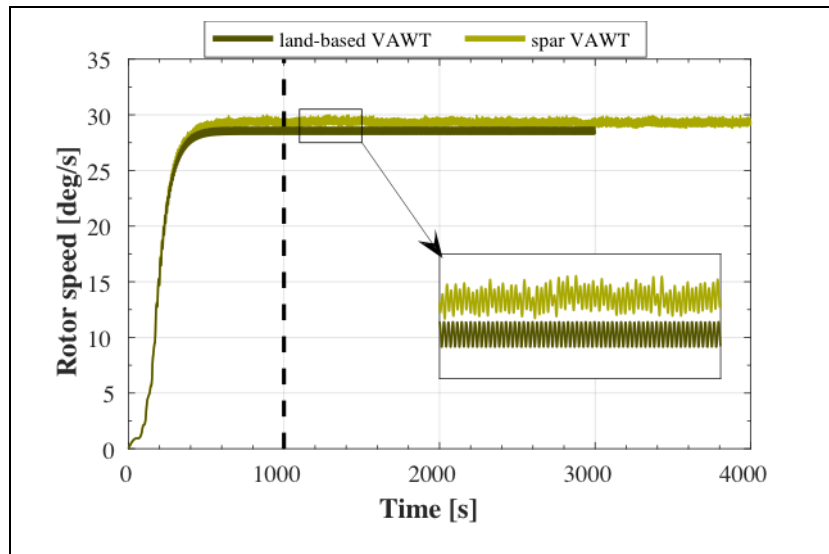
Figure 4.21: Time series of rotor speed for the land-based and spar VAWT (LC2.1a)

As the dashed line indicates, the transient response of rotor speed is well damped out at $1000\ s$. Additionally, it is noticed here that the steady-state value is slightly higher for the spar VAWT. This may be related to wave-induced rigid-body motions.

Regarding the transient response of the platform motions, it is surge and pitch that are governing. The full time series of these platform responses are given by Figure 4.22. The transient duration takes no longer than $1000\ s$, hence this is the time period that is left out in statistical and spectral analysis.

Figure 4.22: Surge and pitch platform motions (LC2.1a, LC2.2a and LC2.3a)

Response of Rotor Speed

The addition of waves does not pose a direct excitation on the rotor speed. However, the response may be influenced indirectly by platform motions. It can be checked whether the wave environment influences the rotor through analyzing the frequency content from spectral analysis. The power spectrum of rotor speed is given in Figure 4.23.
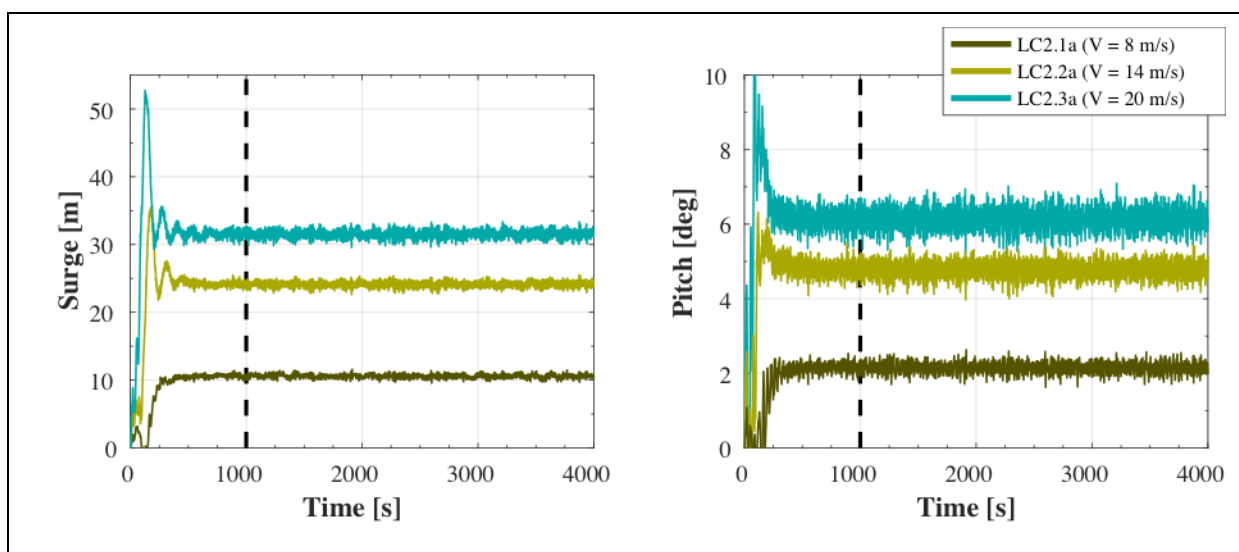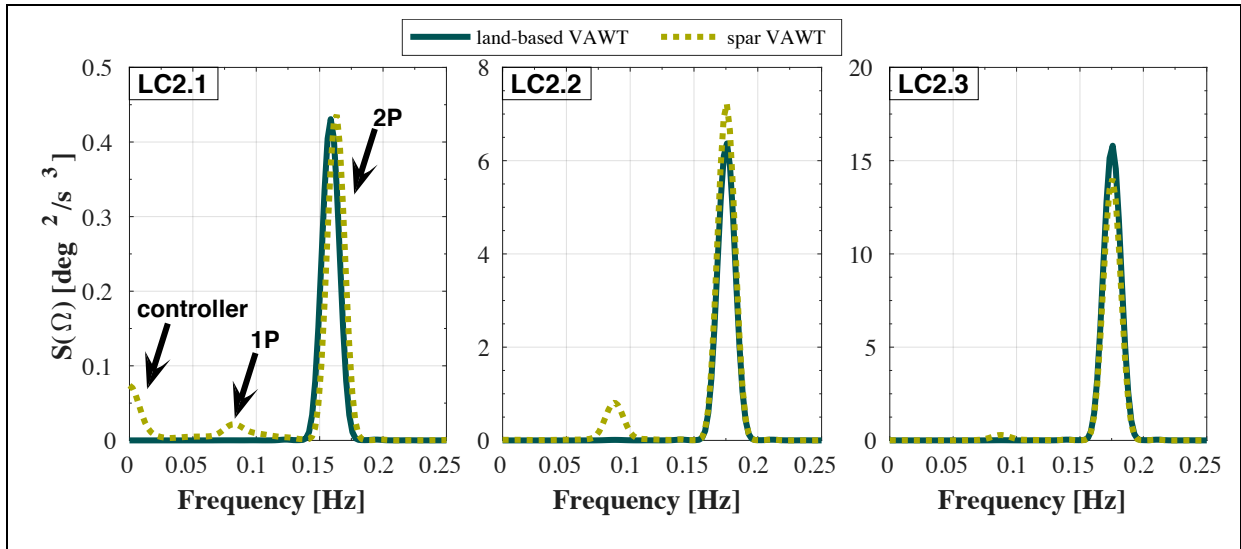

Figure 4.23: PSD of rotor speed for the land-based and spar VAWT (LC2)

The result shows that none of the platform motions (presented hereafter) or the wave spectrum has a significant presence in the rotor speed response. Only the 2P frequency is dominantly present in all results. The spar VAWT also shows a peak at 1P, this is related to the yaw DOF and may be enhanced by the wave spectrum that also covers this frequency. Interestingly enough there is also a low-frequent variation present in the spar VAWT rotor speed response at LC2.1. A spectral peak with this frequency content normally points to turbulent wind or second-order difference-frequency forces. However, the wind is steady and the platform responses show no such peak from hydrodynamic loads. It is therefore deducted that low-frequent variations are a result from the rotor speed controller. Note that LC2.1 lays in the operational region that maximizes C_p.

Response of Platform Motions

Next is to analyze the spar motions. The mean values and standard deviations are given in Figure 4.24. The results are roughly compared to the mean offsets at LC1 in Figure 4.4, no significant differences are observed here. The results presented in Figure 4.24 form a basis of comparison with LC3, which adds wind turbulence to the system.

Figure 4.24: Statistics of rigid-body motion in its six DOFs (LC2)

The time-varying platform motions can be described through its power spectral density, same as done for wave elevation and rotor speed. This tells us about the coupling of motions, and also about the significance 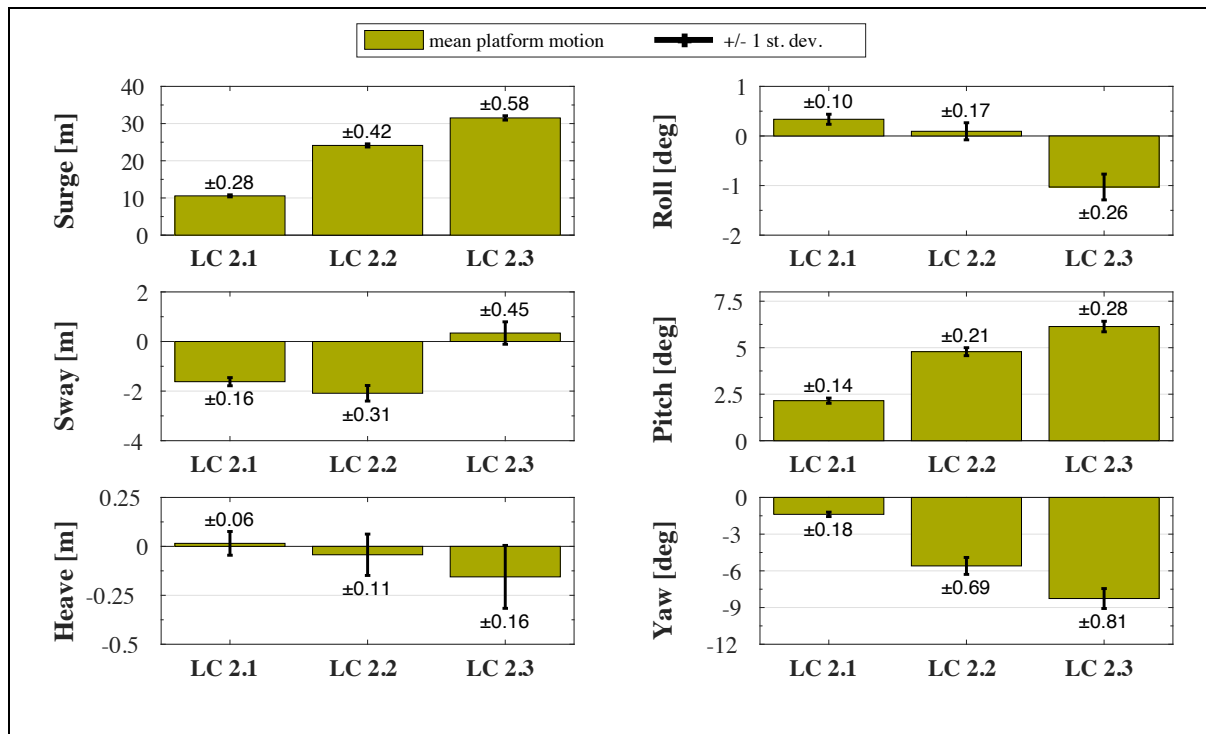of the aerodynamic- and hydrodynamic-induced platform response. The power spectra of platform motions are shown for LC2.2 in Figure 4.25.
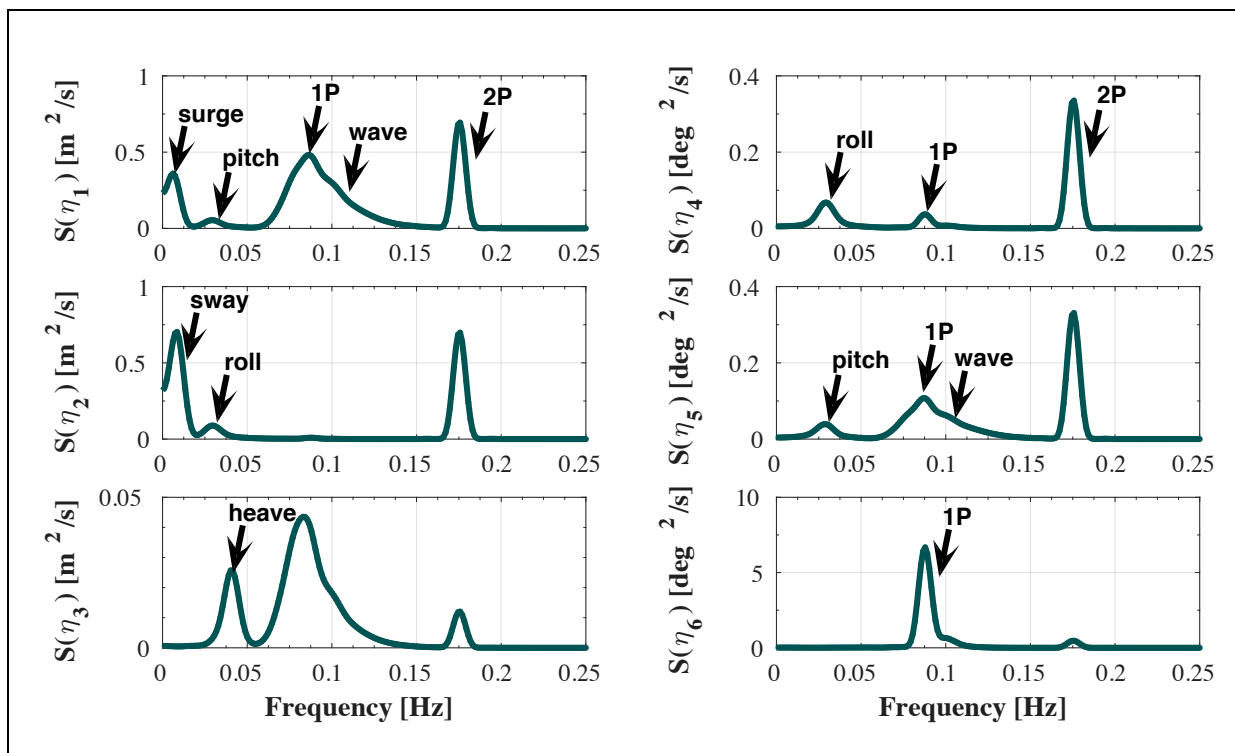
Figure 4.25: PSD of rigid-body motion in its six DOFs (LC2.2)

As indicated by the labels, many peaks can be recognized in the power spectra of platform motions. The natural frequency of each DOF can be found back in its own spectrum, except for the yaw natural frequency (0.135 Hz). Perhaps the latter is shown when plotting the power spectrum on a log-scale, however, this makes distinguishing between the significance of peaks less obvious. The natural frequencies of roll and pitch can be traced back in the power spectra of respectively sway and surge. This describes the coupling of platform motions. The wave spectrum is found in surge, heave and pitch, and has 'merged' with the 1P excitation that lays close to the peak period and within the wave spectrum. Energy content at the 2P frequency is present for all the floater motions. The results that are presented here consider the dynamic response at LC2.2. It should be noted that for LC2.1 and LC2.3 the power spectra are similar (i.e. same peaks), but the magnitude of peaks relative to each other are slightly different due to a change of energy content in the environment.

4.2.3 Internal Structural Loads

The wave environment induces a structural response of the spar VAWT which is studied through the bending moments at the tower base and mid-point of blade 1.
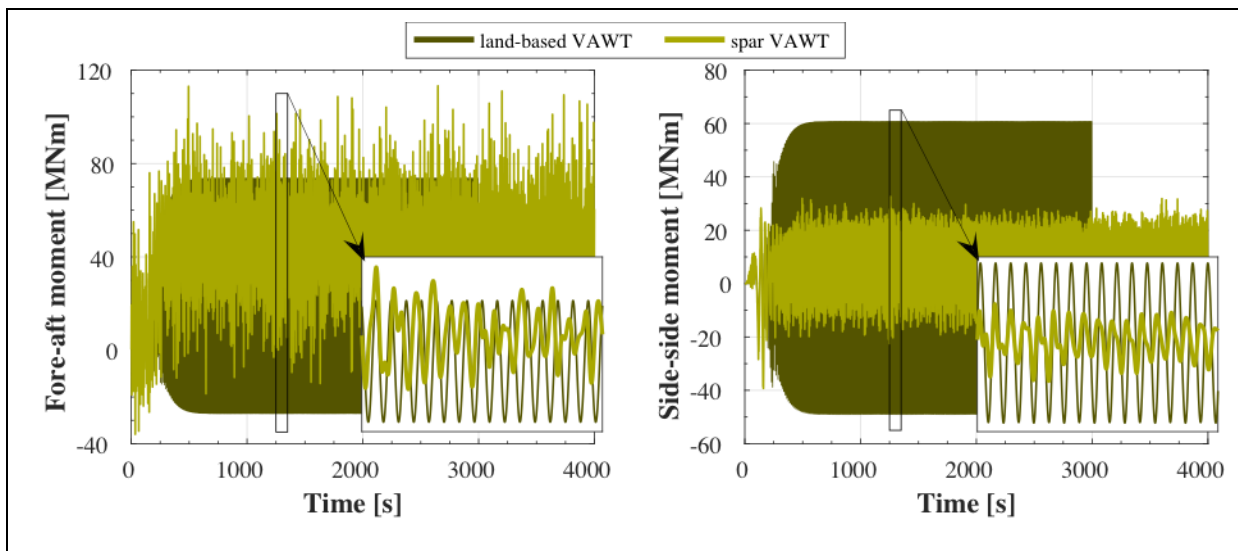
Figure 4.26: Fore-aft and side-side tower base bending moments for the land-based and spar VAWT (LC2.1a)

Tower Base Bending Moments

As observed in the previous section, the waves add new harmonic components to the platform motions. It is expected these additional motions are also felt at the tower base. The tower base bending moments are first illustrated through a time series in Figure 4.26. Here not only the

stochasticity in the spar VAWT response is shown, but also the significant amplitude in the the land-based VAWT response. The cause of the large difference in amplitude was discussed in Section 4.1.4. It is for this reason that the response is presented at LC2.1a ($V_{hub} = 8\ m/s$), where the resonant response of the land-based is smallest and the plot is clearer to read.

From analysis of the statistical results in Figure 4.27 it is found that the mean values of both bending moments are unchanged with the introduction of waves. The standard deviation, however, is increased significantly for the fore-aft bending moments at the tower base of the spar VAWT. In numbers, the standard deviation has increased by a factor 2.1 for LC2.1 and a factor 1.5 for LC2.2 and LC2.3. The additional standard deviation in the side-side bending moments are minimum with a change of less than 1 MNm. The side-side bending moment is only affected slightly because the wave direction is perpendicular to the side-side direction when the platform is not yawed.
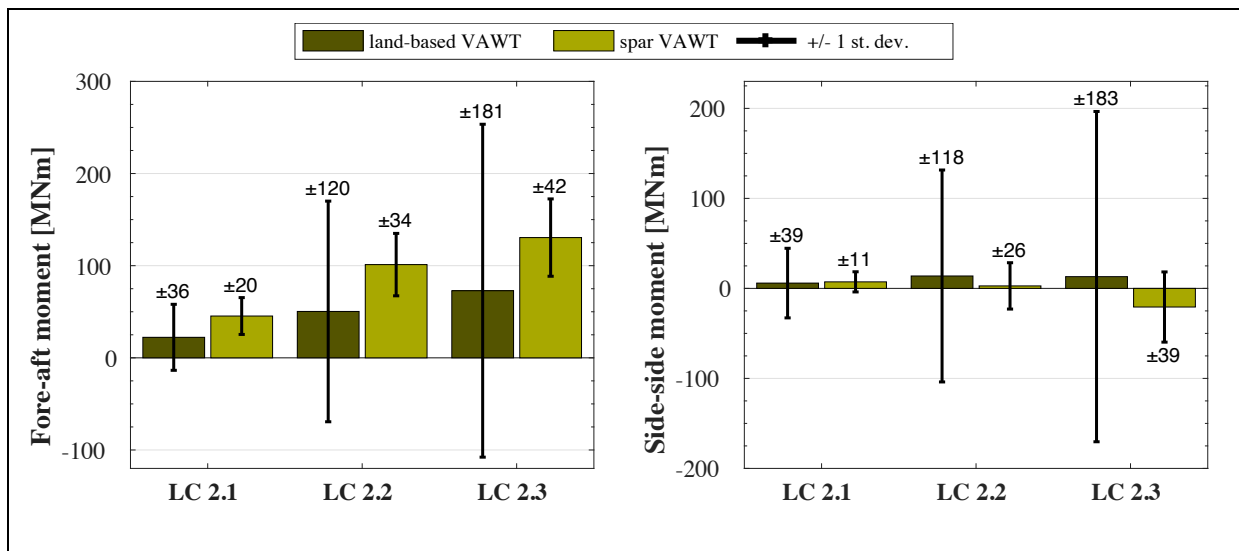
Figure 4.27: Statistical values of the tower base bending moments for the land-based and spar VAWT (LC2)

Knowing that the standard deviation of fore-aft bending moment is increased for the spar VAWT, it is of great interest to investigate its frequency-dependency. The power spectrum is presented at LC2.2 (rated wind speed) in Figure 4.28. The power spectra of the other two load cases are similar in shape but only different in magnitude. It is chosen to present the power spectral density of the spar VAWT again – but separately – on the right side of the figure. This is such that the peaks in the spar VAWT response are not dissolved under the large 2P peak in the land-based VAWT response.
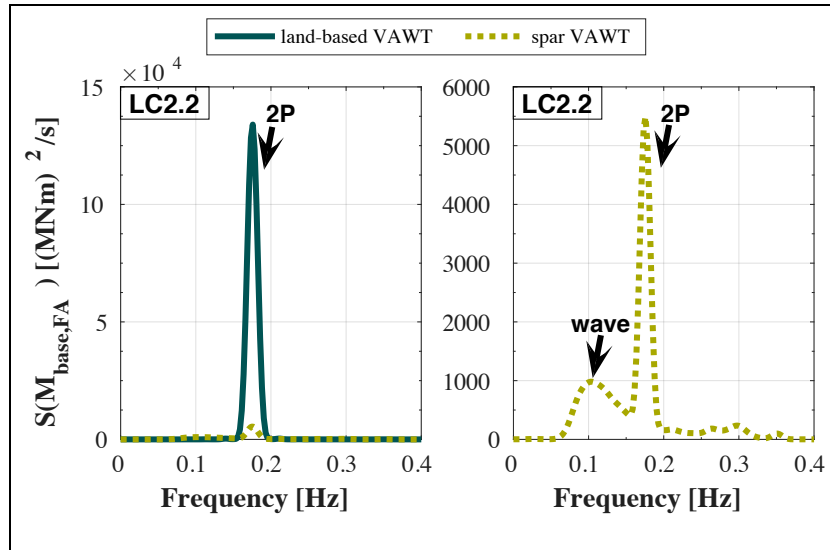
Figure 4.28: PSD of fore-aft bending moments in the land-based and spar VAWT's tower base (LC2.2)

It becomes evident that the wave spectrum is present in the PSD of the fore-aft bending moment at the tower base of the spar VAWT. Nevertheless, the 2P excitation from aerodynamic loads is still dominant for this response. There is also energy content at higher frequencies, but these are difficult to distinguish, possibly related to the blade modes. More on these higher frequent peaks are discussed for LC3 in Section 4.3.4.

Mid-Blade Bending Moments

Similar to the rotor speed, the hydrodynamics do not directly act on the blades, but they are indirectly felt through platform motions. There stochastic influence of the wave environment on the mid-blade bending moments are shown through a time series in Figure 4.29.
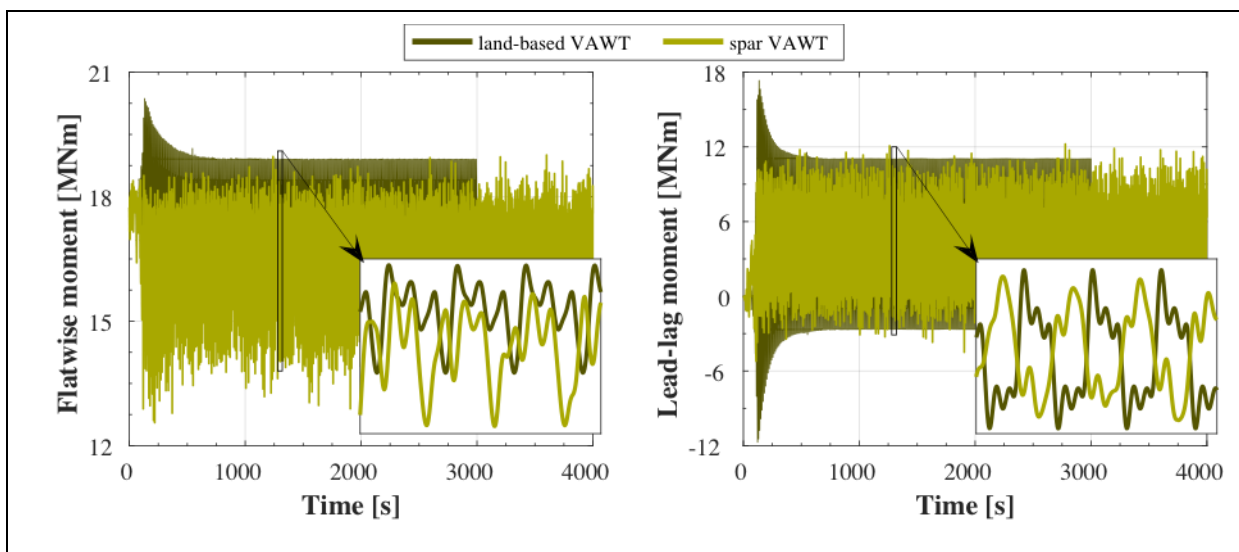
Figure 4.29: Mid-blade bending moments for the land-based and spar VAWT (LC2.2a)

4.2 Steady Wind and Irregular Waves of LC2: Wave-Induced Response

It is seen that the flatwise mid-blade bending moment has a higher amplitude content for the spar VAWT. This may be unexpected – knowing that the wind field is steady – but actually shows that the gravity-induced loads contribute to a large part of the response. The close up in Figure 4.29 shows the responses of the spar VAWT blade are fairly periodical within a shorter time interval. From statistical analysis is it found that the mean values are unaffected with respect to the wind-only environment of LC1. The standard deviations of the bending moment responses at the mid-blade are increased at all loads cases. The results are summarized in terms of a percentual increase with respect to LC1 in Table 4.1.

Table 4.1: Percentual increase in standard deviation of mid-blade bending moments for the spar VAWT at LC2 relative to LC1

	$\Delta\sigma(M_{flatwise})$	$\Delta\sigma(M_{lead-lag})$
LC2.1	+50.1%	+5.7%
LC2.2	+7.6%	+2.6%
LC2.3	+1.2%	+2.5%

It is mainly the flatwise bending moment at the mild wind-wave environment that is affected by the waves. This can also be observed in the power spectrum of the flatwise bending moment response in Figure 4.30. Hereafter the opportunity is taken improve the understanding of bending moments in the blades through the discussion of the spectral analysis.
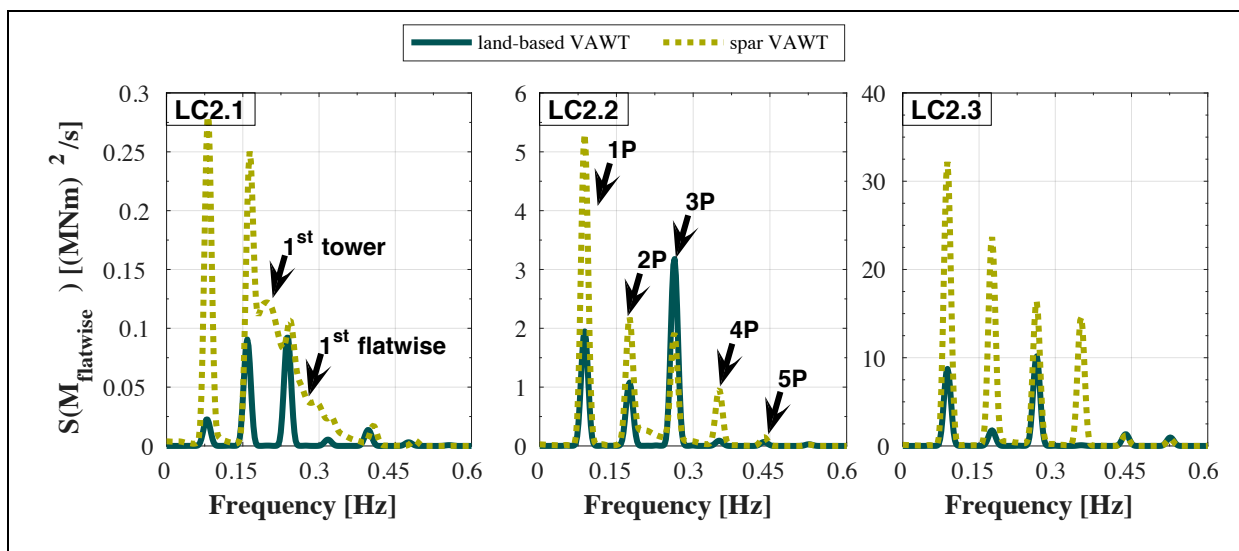
Figure 4.30: PSD of mid-blade flatwise bending moments for the land-based and spar VAWT (LC2)

The PSD shows interesting behavior with many (new) peaks. The land-based response also shows multiple peaks, which can be related to the multiple harmonics recognized in the time

series presented earlier (see Figure 4.29). The flatwise response is generally governed by the 1P, 2P, 3P and 4P frequencies. The first flatwise modes are close to the 3P frequency, but possibly shifted due to centrifugal stiffening. Upon comparison of the land-based and spar VAWT it shows that the latter contains higher energy content at almost all peaks. The increase in standard deviation of the flatwise response was mentioned before, it can be related to the gravitational loads being in phase with the aerodynamic loads and adding to the 1P excitation. The power spectra of the side-side bending moment is presented in Figure 4.31 and shows the opposite behavior.
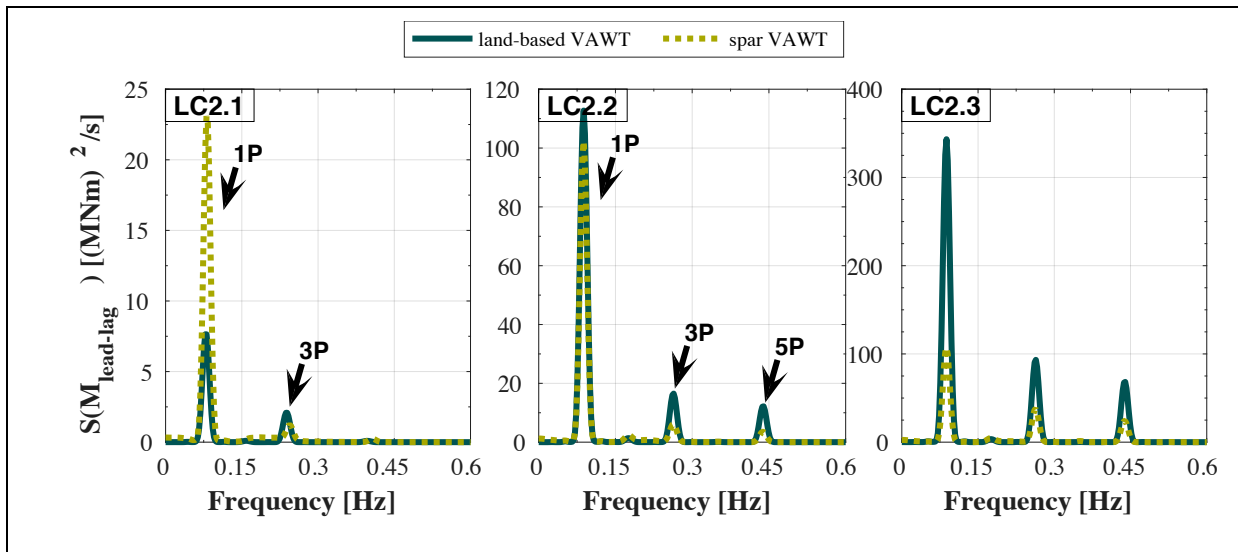
Figure 4.31: PSD of mid-blade lead-lag bending moments for the land-based and spar VAWT (LC2)

With an exception at LC2.1, the land-based VAWT contains higher peaks for the side-side bending moments at the mid-blade. This can be related to the yaw DOF of the spar VAWT. The peaks are found at the 1P, 3P and 5P frequencies. The aerodynamic loading can excite the 'twisting' lead-lag mode and the gravity-induced loads of the spar VAWT could excite the 'butterfly' lead-lag mode. These modes were presented in Table 3.4 as mode 5 and 6, respectively. It should be noted that it is difficult to comment on the eigenfrequencies of the lead-lag modes during operational conditions, since stiffening can occur from gyroscopic effects.

4.3 Turbulent Wind and Irregular Waves of LC3: Turbulence-Induced Response

The last load case in the model-comparison considers fully turbulent wind and irregular waves. It was seen previously that aerodynamic loading greatly affects the dynamic response of the (floating) VAWT, hence wind turbulence is an interesting addition to the analysis. Section 4.3.1 characterizes the turbulent wind field and presents a sensitivity study to the number of seeds that are used. This is followed by the global dynamic response of rotor speed and the spar floater motions in Section 4.3.2. The effect of wind turbulence on the aerodynamic loads and the internal structural loads is discussed in Sections 0 and 4.3.4, respectively.

4.3.1 Describing the Stochastic Wind-Wave Environment

Turbulent Wind Field

The wind turbulence is modeled according to the NTM. The turbulent field is then described by a set of parameters that can be used to generate the wind field. For a better understanding of what this actually looks like, Figure 4.32 shows the time series of wind speed at hub height at each of the three wind environments for one seed.
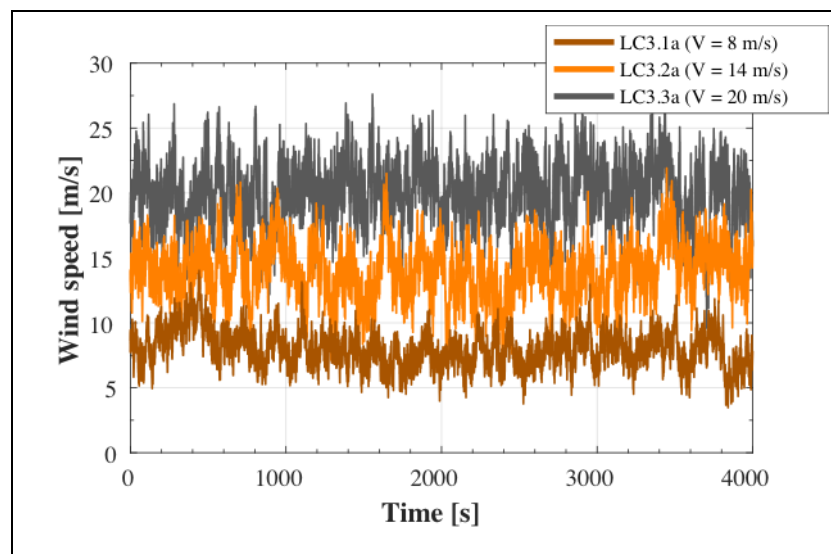
**Figure 4.32: Visual of wind speed at hub height in LC3.1a,
LC3.2a and LC3.3a**

The time history shows that the turbulent wind field contains both high-frequent and low-frequent variations with time. The low-frequent variations can cause short-term shifts in mean wind speed, whereas the high-frequent components can induce large-amplitude variations in local instantaneous wind speed. The wind environment is described by its PSD in Figure 4.33.

The power spectrum shows us that the wind turbulence contains most energy in the low-frequent variations.
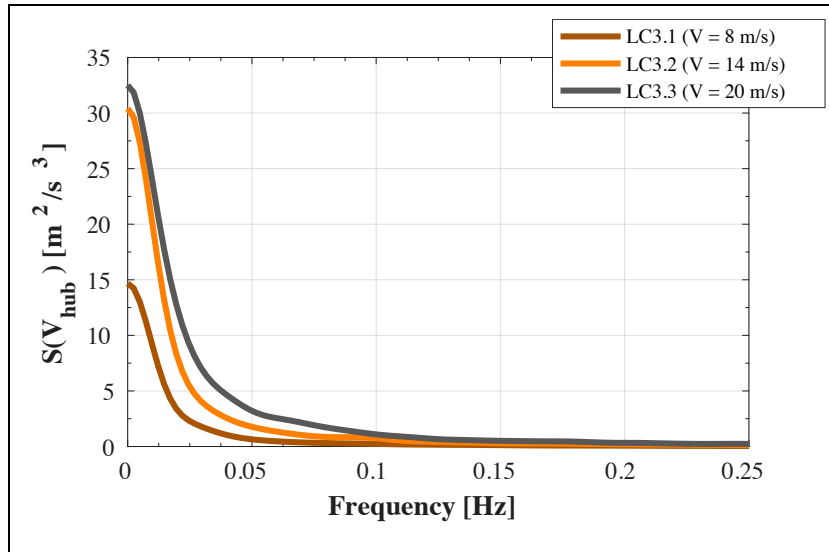
Figure 4.33: PSD of wind speed in the environments of LC3

Sensitivity to Number of Seeds

The seed that is used in generating the unsteady wind and wave environment is essentially just a set of random numbers that create stochasticity. A stochastic excitation can influence the statistics and spectral density of the resulting responses. For this reason, it is of great interest to investigate how the number of seeds influences the statics of the wind and wave environment. Load case 3.2 (rated wind speed) was repeated for 10 different seeds. The sensitivity to number of included seeds is shown for wind speed in Figure 4.34 and for wave elevation in Figure 4.35.
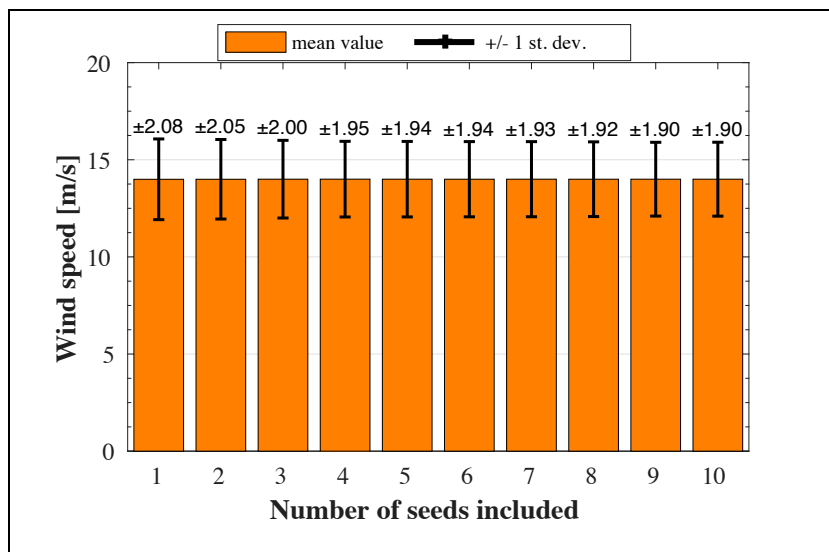
Figure 4.34: Wind speed at hub against number of seeds (LC3.2)

The 10 seeds that used in LC3.2 are selected randomly. The first three seeds are the same ones used for the analysis of any stochastic event in this thesis. It is seen that the mean values of wind speed and wave elevation are respectively $14.0\ m/s$ and $0.0\ m$, regardless of the amount of seeds included. On the other hand, the standard deviation does shows a dependency on the number of seeds for in particular the wind speed. The standard deviation of the individual seeds used here ranges between $1.71\ m/s$ and $2.08\ m/s$, hence it would require a substantial number of seeds to balance the stochasticity.
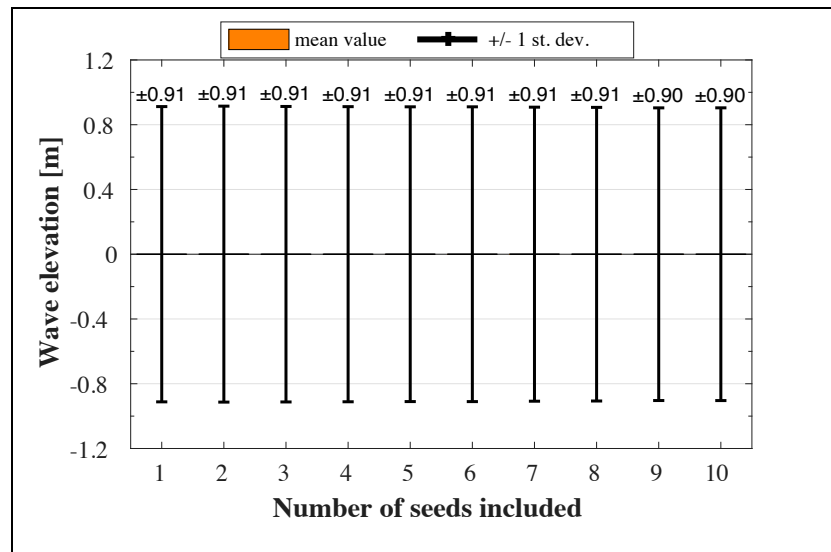
Figure 4.35: Statistics of wave elevation against number of seeds included (LC3.2)

4.3.2 Global Dynamic Response

It has been illustrated that the turbulent wind environment introduces significant low-frequent and high-frequent variations to the wind field. These fluctuations are felt by the VAWT rotor and are expected to induce different responses in rotor speed and platform motions as opposed to the steady wind cases. First the response is illustrated through a time series, which is followed by a presentation of the results of statistical and spectral analyses.

Time Series of Rotor Speed and Platform Motions

The time series of rotor speed at the mean wind speed of $8\ m/s$ (LC3.1a) is shown in Figure 4.36. It can be seen that the rotor speed is not sensitive to the large (local) instantaneous fluctuations that were observed in the wind speed time series. This is likely due to turbulence being a function of both time and space, which implies that the high-frequent variations from small eddies are different throughout the rotor surface. The large eddies that cause low-frequent variations can cover the full VAWT rotor. The enlarged time series between $1100\ s$ and

1500 s shows that additional high-frequent fluctuations are present in the spar VAWT rotor speed, this is likely due to the platform response.
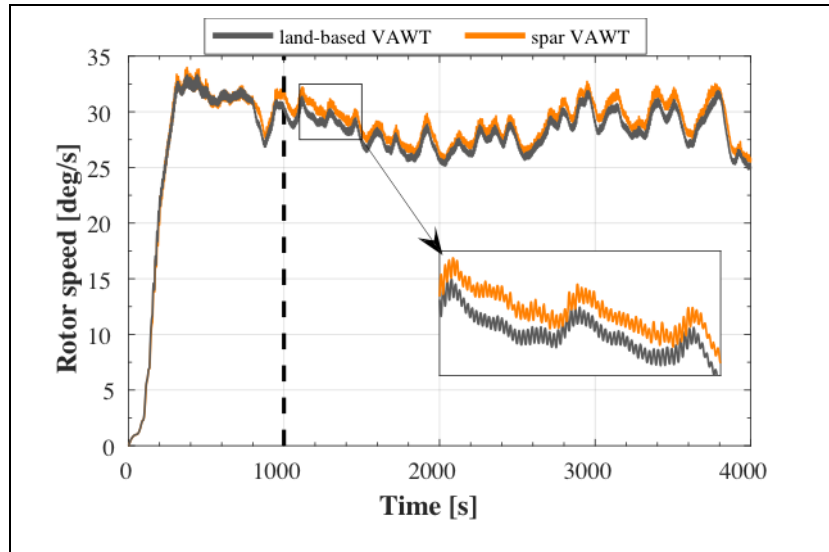
Figure 4.36: Time series of rotor speed for the land-based and spar VAWT (LC3.1a)

The time series of surge and pitch are shown in Figure 4.37. Again, both platform responses contain a highly dynamic content different from the responses in a steady wind-only environment in Figure 4.2. The fluctuations in the pitch motions seem more frequent than the surge motions, this is related to the natural frequency of the DOFs.
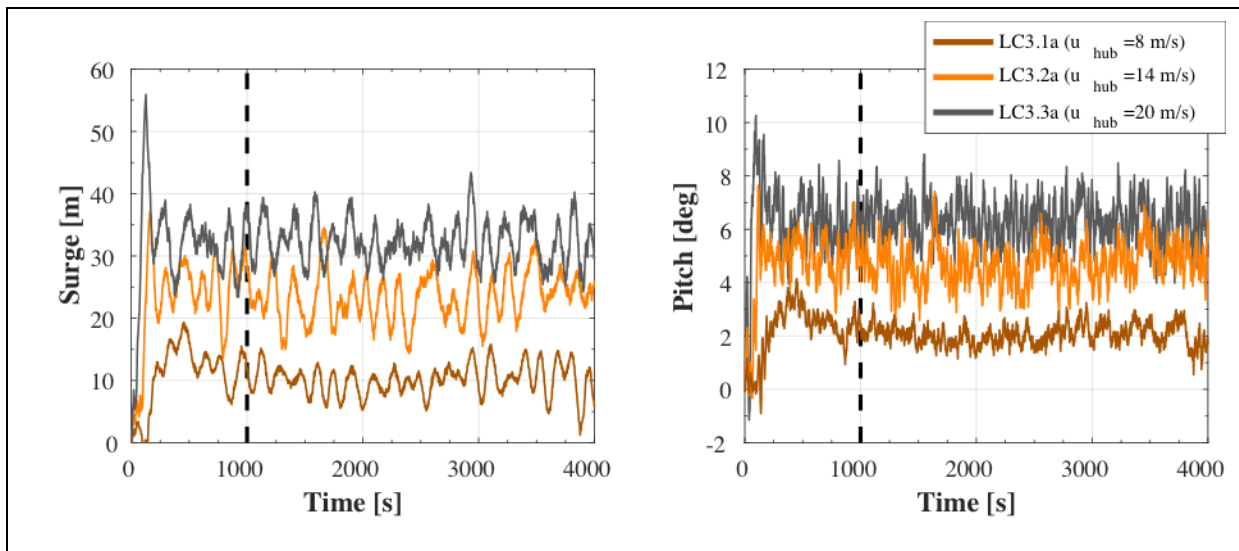
Figure 4.37: Time series of surge and pitch platform motion for the spar VAWT (LC3.1a, LC3.2a and LC3.3a)

The unsteady nature of the response makes it more difficult to determine when the transient effects have damped out. The unsteady environment generally increases the amount of damping in the system, hence it is save to stay with the transient duration determined for the

steady wind environment of LC2. The first 1000 s of all responses are ignored, as marked by the dashed lines in the time series above.
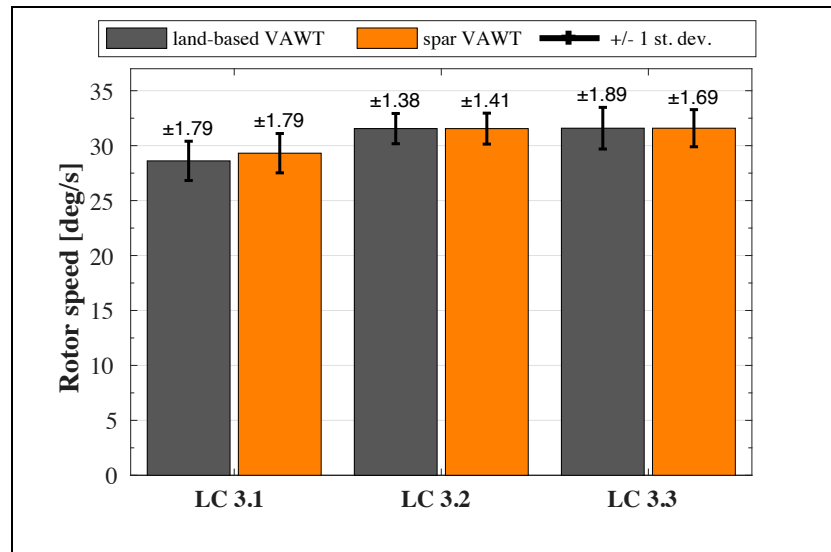
Figure 4.38: Statistical values of rotor speed for the land-based and spar VAWT (LC3)

Responses of Rotor Speed and Platform Motion

Statistical analysis is performed for rotor speed and it shows that turbulent wind increases the standard deviation. In contrast to the response at LC1 and LC2, the standard deviation at LC3 is of similar magnitude at all wind speeds. Overall, the standard deviation increased by a factor
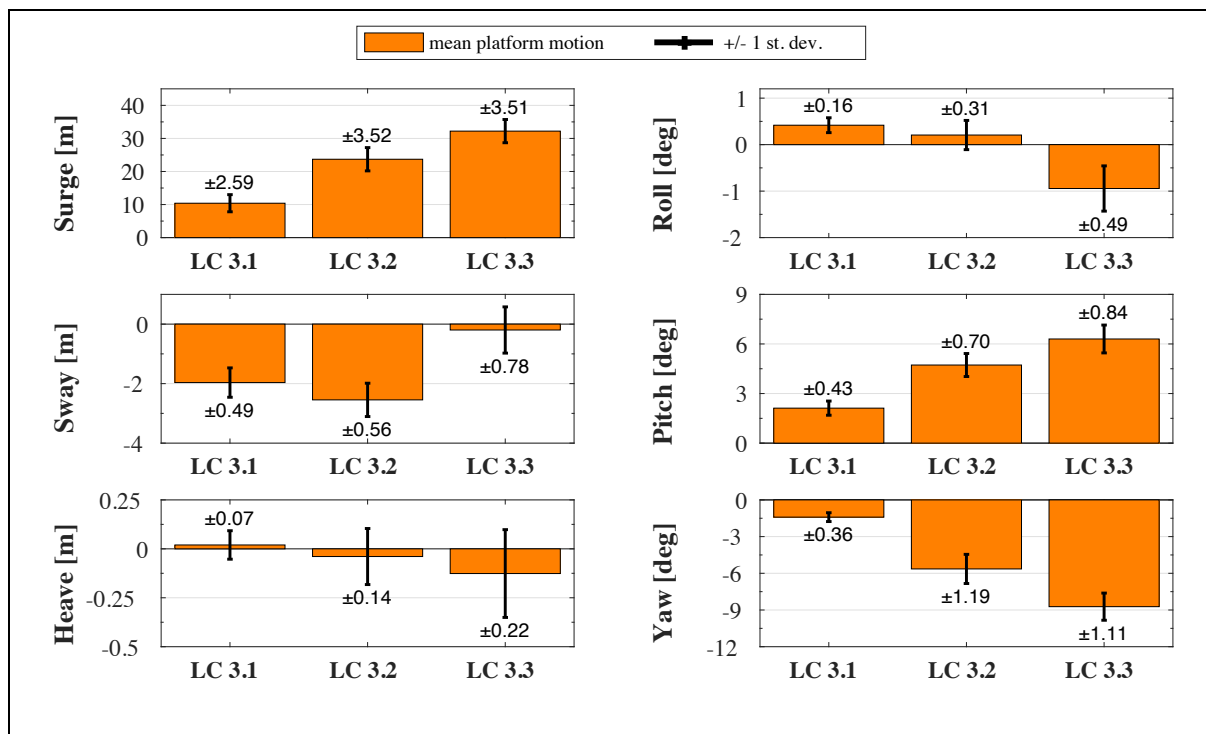
Figure 4.39: Statistics of rigid-body motion in its six DOFs (LC3)

of approximately 8 for LC3.1 and approximately 1.5 for LC3.2 and LC3.3. Likely this is related to the slowly-varying rotor speed response, which is (most of the time) not limited to a maximum value by the controller at LC3.1. Spectral analysis has brought forward that the dominance of the 2P effect is much diminished with the introduction of wind turbulence, particularly for the milder environmental conditions.

The statistical analysis of platform motions shows no change in mean values, but also the standard deviations of these responses have significantly increased. The prior is sensible, because the mean wind speed is unchanged with the introduction of turbulence. From Figure 4.39 it is seen that surge is affected most when compared to the platform motions at LC2 (see Figure 4.24). Furthermore, the pitch DOF is also excited by the turbulent wind. Overall, the standard deviation of surge and pitch are increased by a factor of approximately 10 and 3, respectively.
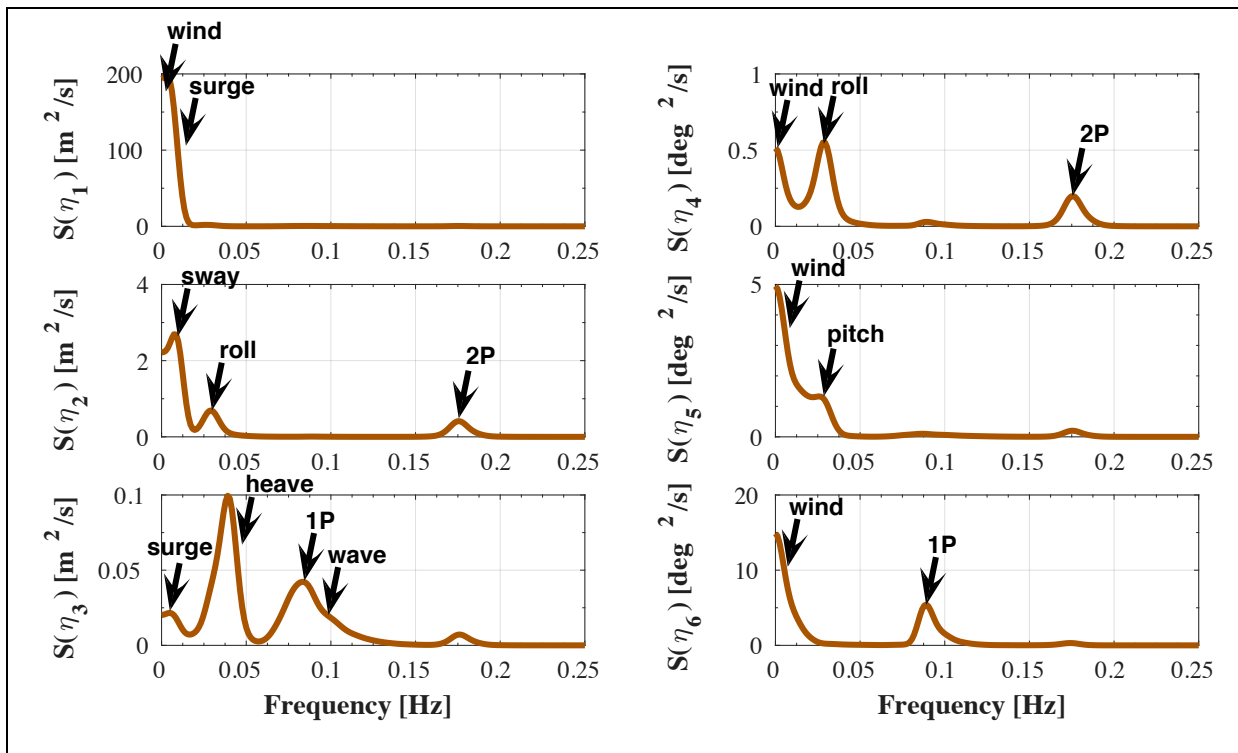
Figure 4.40: PSD of rigid-body motion in its six DOFs (LC3.2)

The power spectra of platform motions at LC3.2 is shown by Figure 4.40 in order to understand more about the frequency content of the variations in the response. From a general comparison with the steady wind cases it is observed that the 2P peak is is largely reduced, because it is has made space for the wind spectrum instead. As concluded from the statistical analysis, the wind spectrum is most dominant in the surge and pitch response. On top of this, the yaw is also

affected by the wind turbulence. It is interesting to notice that the significant energy in the surge response has left its traces in the heave response too. At last, the wave-induced platform responses have become insignificant with respect to LC2, with the exception in the heave DOF.

4.3.3 Unsteady Aerodynamic Loading

It was seen in the responses of rotor speed and platform motion that turbulent wind introduces quite a significant change. The excitation loads of these responses is still governed by the wind, hence this section presents the aerodynamic loads in the turbulent wind field environment of LC3. The wind-induced excitation loads on the system are rotor thrust and aerodynamic torque, the variation in time at (mean) rated wind speed is shown by Figure 4.41.
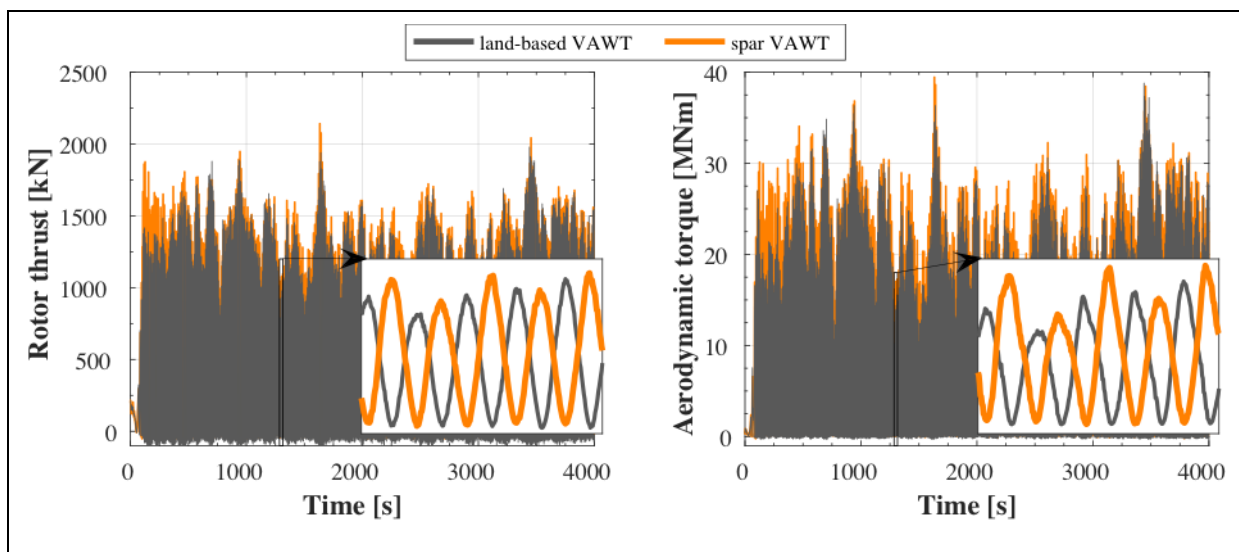
Figure 4.41: Rotor thrust and aerodynamic torque for the land-based and spar VAWT (LC3.2a)

The response of the two aerodynamic loads is very similar in time and also the responses between the VAWT models follow the same trends. The spar VAWT seems to be subjected to an additional 1P component. The minima of aerodynamic loads always tend to approximately zero.

Statistical analysis is done for the rotor-averaged aerodynamic loading at all load cases, the results are presented in Figure 4.42. It is interesting to observe that the statistical values of aerodynamic loading for the spar VAWT decrease with respect to the land-based VAWT at higher wind speeds. The reasoning was discussed for LC1 and it was concluded that it relates to tower tilting and the yaw DOF of the spar floater. Upon comparison of aerodynamic loading between LC3 and LC2, a slight increase in mean thrust is found for the lower wind speeds (LC3.1 and LC3.2). The mean rotor thrust at the higher wind speed of LC3.3 and the mean aerodynamic torque at all wind speeds decreased with values ranging between 0.7% – 5.9%,

considering both VAWT models. The standard deviation of aerodynamic loading decreased for all turbulent load cases (relative to LC2), with a decrease up to 4.2% for rotor thrust and 10.7% for aerodynamic torque.
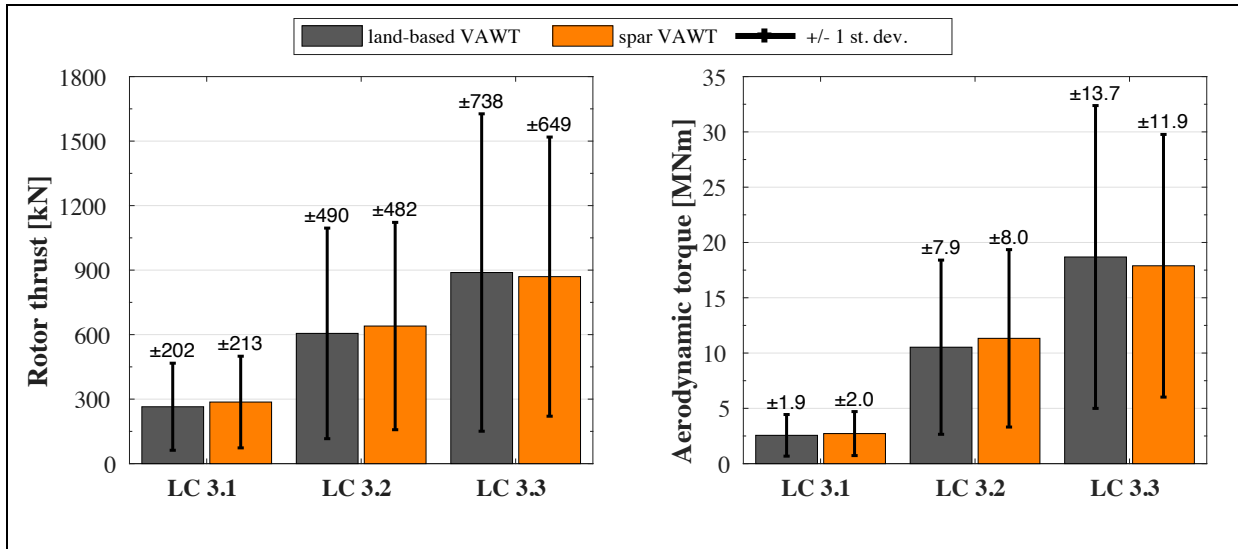
Figure 4.42: Statistical results of aerodynamic loads for the land-based and spar VAWT (LC3)

Results from spectral analysis shows that variation in aerodynamic loads is still dominated by the 2P effect. The wind spectrum is present in all power spectra, and a smaller peak at the 1P frequency is also found in the PSD of the spar VAWT's aerodynamic torque. The 2P peak for LC3.1 is wider than for LC2, because the short-term rotor speed response – and hence also the 2P frequency – varies slightly with time in the turbulent cases.

4.3.4 Internal Structural Loads

In the previous section it was discovered that wind turbulence generally decreases the standard deviation of aerodynamic loads. The influence of the more realistic wind environment on the internal structural loads is studied in this section. A comparison is made with the steady wind and irregular wave environment of LC2, with respect to the bending moments at the tower base and mid-blade.

Tower Base Bending Moments

Upon a first glance of the statistical analysis of the tower base bending moments in Figure 4.43 it shows the same trends as for the environment in LC2 (see Figure 4.27). Although, a more careful comparison shows that all standard deviations have decreased similarly as for the aerodynamic loading. With decreased values up to 11.9%, the land-based VAWT tower is slightly more affected by the turbulent wind than the spar VAWT tower with standard deviations reduced up to 9.1%. The mean fore-aft moments are not significantly changed.
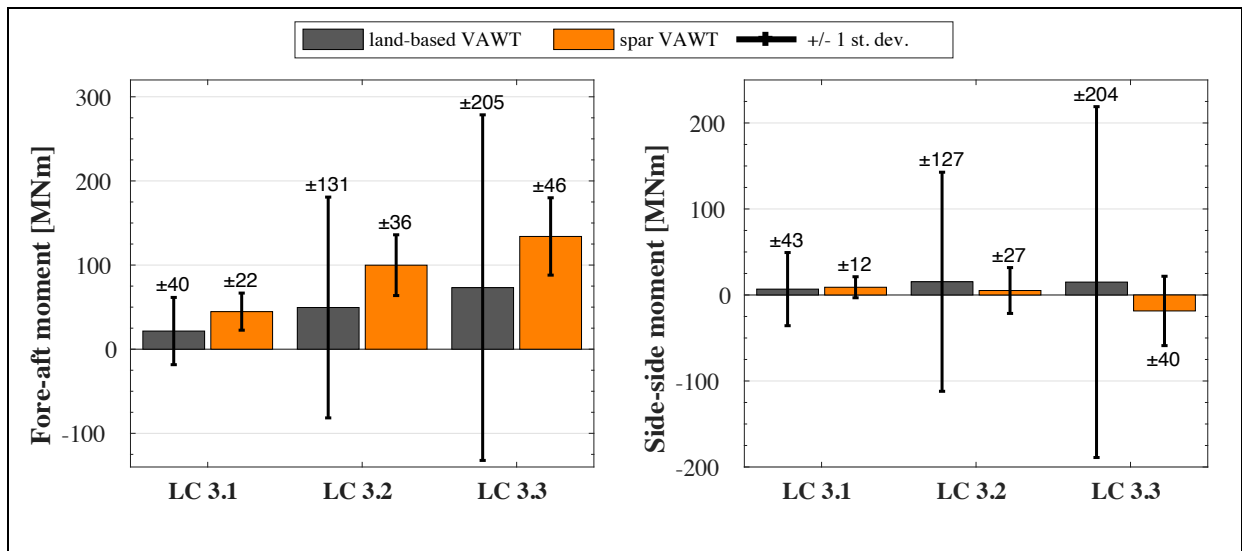
Figure 4.43: Statistics of tower base bending moments for the land-based and spar VAWT (LC3)

The power spectrum of fore-aft bending moments in turbulent wind contains additional peaks when compared to the response at LC2.2. Figure 4.44 shows that the PSD at LC3.2 contains (significant) energy at the wind speed spectrum for the spar VAWT. Even in turbulent wind, the land-based VAWT is still governed by the resonant 2P tower response. At last, the spar VAWT shows a peak at 0.30 *Hz* in the fore-aft bending moment spectrum. The smaller group of peaks in the same frequency region were difficult to distinguish for LC2.2 in Figure 4.28, but LC3.2 shows a better defined peak. Energy at this frequency has not been recognized in any other response. Also, it is present for the spar VAWT only. From this it is reasoned that it must be a (higher) tower mode of the rotor-spar combination.
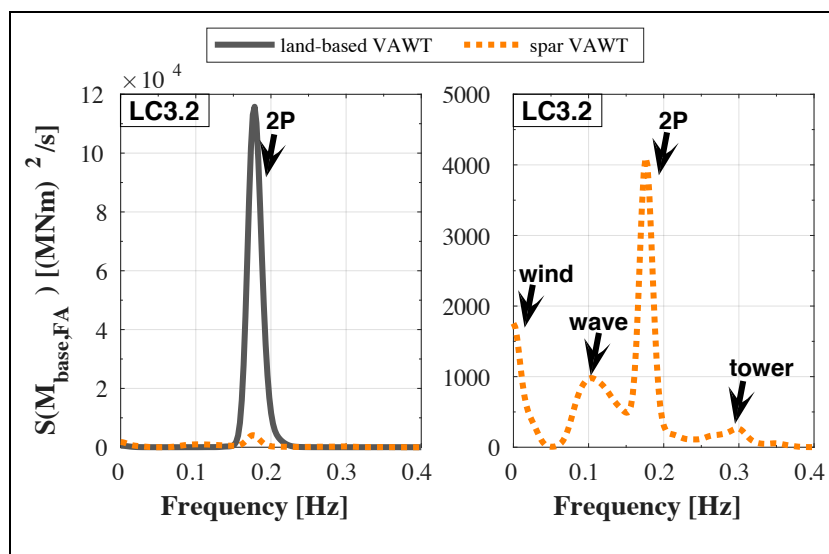
Figure 4.44: PSD of the fore-aft tower base bending moments for the land-based and spar VAWT (LC3.2)

Mid-Blade Bending Moments

The mean values and standard deviations from statistical analysis for mid-blade bending moments are given by Figure 4.45.
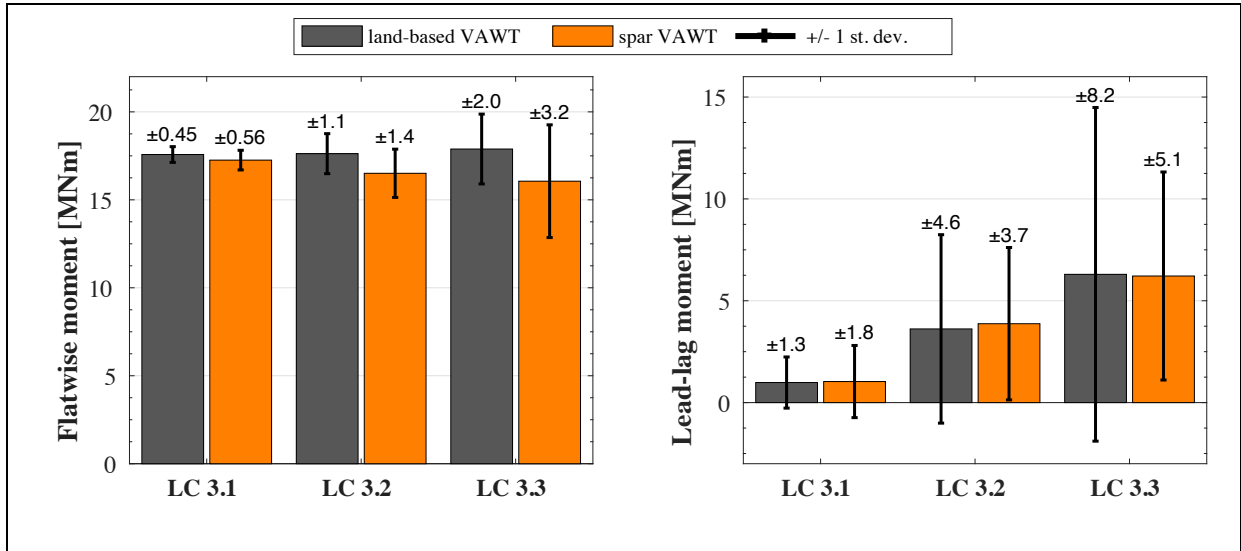
Figure 4.45: Mean values and standard deviation of mid-blade bending moments for the land-based and spar VAWT (LC3)

A notable decrease in mean flatwise bending moments occurs for the spar VAWT, this was also encountered earlier and related to the mean roll and pitch offset. The mean values are not affected significantly with respect to LC2, except a reduction of approximately 5% in the lead-lag moment at LC3.3. This is a result of the reduced aerodynamic torque discussed in the previous section. In contrast to the mean values, the standard deviations are significantly decreased with respect to the steady wind environment of LC2. For both the land-based and spar VAWT, the percentual changes in standard deviation of the mid-blade bending moments are summarized in Table 4.2.

Table 4.2: Percentual decrease in standard deviation of mid-blade bending moments for the spar and land-based VAWT at LC3 relative to LC2

	$\Delta\sigma(M_{flatwise})$		$\Delta\sigma(M_{lead-lag})$	
	Land-based	**Spar**	**Land-based**	**Spar**
LC3.1	-62.0%	-28.4%	-20.6%	-4.9%
LC3.2	-25.2%	-20.0%	-15.4%	-3.6%
LC3.3	-21.7%	-25.8%	-10.4%	-13.1%

Turbulent wind adds not only a stochastic variation in time, but also in space. In the steady wind field there is only spatial variation from wind shear. Such steady sheared wind induces

higher normal and tangential loads at the upper half of the blade than at the bottom half. This loading profile can for instance excite the first flatwise modes. It is therefore reasoned that the additional variation in space in a turbulent wind field is less likely to excite the blade modes.

5 Results and Discussion: Comparison of HAWC2 and SIMO-RIFLEX-AC

The second part of this thesis studies and compares the behavior of the numerical tools HAWC2 and SIMO-RIFLEX-AC. Three load cases are carefully designed in order to isolate different parts in the codes. LC4 and LC5 are set up to study the implementation of the AC flow theory and dynamic stall model, respectively, and both consider the rigid land-based VAWT in a steady wind field. LC6 simulates a realistic environment with fully turbulent wind and correlated irregular waves and considers the flexible spar VAWT. The constant rotor speed controller is applied in all load cases, which is done to minimize the sensitivity that would otherwise be introduced by the constant power controller. The results corresponding to LC4, LC5 and LC6 are presented and discussed in the respective Sections 5.1, 5.2 and 5.3.

5.1 Steady Wind of LC4: Comparison of the Aerodynamic Model

LC4 models the rigid land-based VAWT in a (sheared) steady wind environment. The focus lays in comparing the aerodynamic model as implemented in HAWC2 and SIMO-RIFLEX-AC. The environmental conditions are checked in Section 5.1.1. Prior to comparing the resulting aerodynamic loads in Section 5.1.3, understanding of the rotor response is gained by analyzing the rotor speed in Section 5.1.2. The effect of dynamic stall is not included in the analyses of LC4.

5.1.1 Inspecting the Wind Environment

Considering that in the second part of the study two different codes are used for generating the external environment, it is wise to check the resulting wind environment. It may seem unnecessary for steady wind cases, but a short check avoids unforeseen differences in the VAWT response. Time series of the three wind speeds 8, 14 and 20 m/s at hub height in respectively LC4.1, LC4.2 and LC4.3 are shown by Figure 5.1.
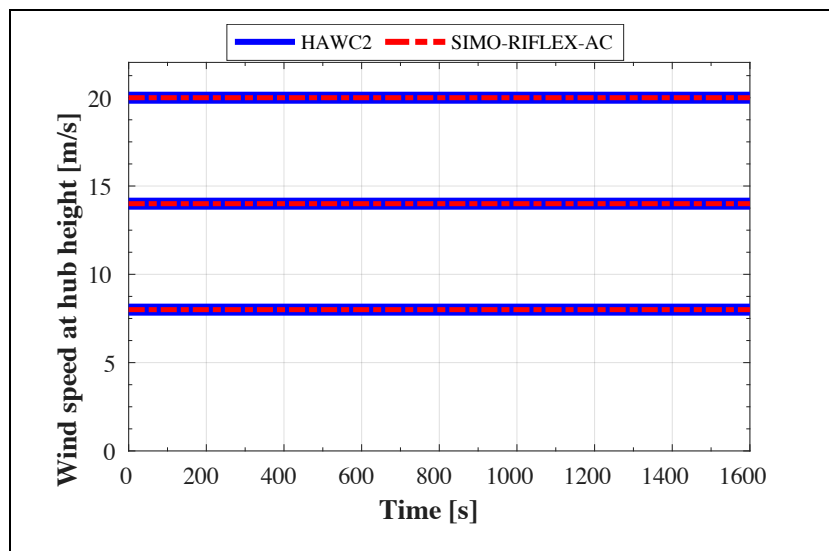
Figure 5.1: Wind speed at hub height in HAWC2 and SIMO-RIFLEX-AC (LC4.1, LC4.2 and LC4.3)

The wind is found to be steady as expected. There are no differences in the wind speed at hub height between HAWC2 and SIMO-RIFLEX-AC. Wind shear is more critical for a turbulent wind environment, therefore a correct implementation of the NWP is checked for LC6 in Section 5.3.1 (see Figure 5.18). There is shown good agreement between the codes with regard to the wind profile.

5.1.2 Response of Rotor Speed

The steady wind field of LC4 is applied to a rigid land-based VAWT. The structure contains only one degree of freedom in the rotational direction of the rotor. This narrows the system down to an equilibrium between aerodynamic loads, rotor inertia and generator torque from the controller. Figure 5.2 shows a time series of rotor speed at the low and high wind speeds of respectively LC4.1 and LC4.3.
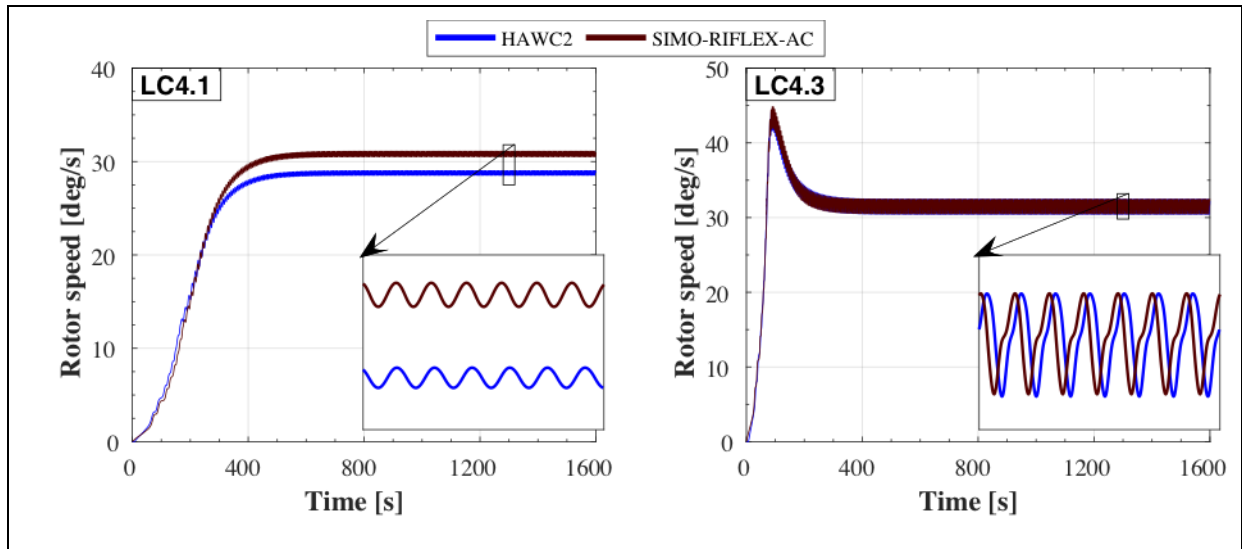
Figure 5.2: Rotor speed in HAWC2 and SIMO-RIFLEX-AC (LC4.1 and LC4.3)

Generally, the rotor speed response of the two codes agree well in terms of shape. In terms of magnitude however, a different steady-state response is found at LC4.1 for the low wind speed of 8 m/s. Here the mean rotor speed in steady-state is 28.8 deg/s for HAWC2 and 30.8 deg/s for SIMO-RIFLEX-AC.

As addressed previously, LC4 isolates the aerodynamic model, structural formulation and controller model of the codes. The considered Darrieus rotor at a wind speed of 8 m/s operates in a region where the C_p is optimized by the controller. The power optimization is done through a generator torque algorithm that aims to minimize the error between the reference and measured rotational speed. The performance of the controller is compared here by observation of the reference rotational speed in time. As shown by Figure 5.3, the steady-state reference rotational speed is lower for HAWC2 than for SIMO-RIFLEX-AC.
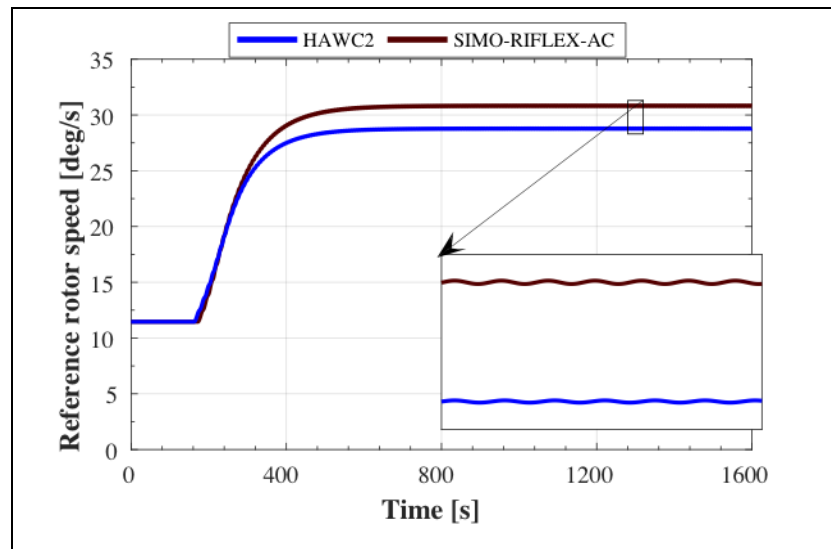
Figure 5.3: Reference rotor speed for the land-based VAWT at LC4.1 in HAWC2 and SIMO-RIFLEX-AC

From comparison of the reference rotational speed and the actual (measured) rotor speed, it is concluded that the controller performs correctly in both codes. This implies that the measured generator torque causes the different rotor speed at LC4.1. A difference in the standard deviation of generator torque (thus rotor speed) would point towards rotor inertia. However, a difference in the mean rotor speed implies that the aerodynamic excitation loads are different.

5.1.3 Comparing the Aerodynamic Models

This section focusses on the outputs of the aerodynamic model in HAWC2 and SIMO-RIFLEX-AC. First the differences in the aerodynamic models are described, which is followed by a presentation of the resulting induced flow velocities. Then the rotor-averaged aerodynamic loads are compared, and the analysis on LC4 is concluded with a presentation of the overall aerodynamic performance in terms of the power and thrust coefficients.

Implementation of the AC Flow Theory

It was brought forward in Section 3.3.1 that the modified linear solution of the AC flow model is slightly different in HAWC2 and SIMO-RIFLEX-AC. There is distinguished between modified linear solution II (HAWC2) and modified linear solution III (SIMO-RIFLEX-AC). The theoretical background on these solutions of the AC flow model is extensively covered in Section 2.2.2. The differences between the modified linear solutions are highlighted here. To summarize, modified solution III considers three additional elements being (1) another correction factor k_a at high tip-speed ratios, (2) local blade element inclination and (3)

inclusion of the tangential loading terms. The consequences of the additional correction factor are expected to be most direct and significant, hence a more detailed description is given below.

In the modified linear solution II the induced velocities are amplified by a correction factor k_a. Cheng et al. [21] suggested an addition to the correction factor k_a at high tip-speed ratios, which is implemented in modified linear solution III. The additional correction is based on experimental data and corrects the induced velocities based on the following relationship between the axial induction factor a and average thrust coefficient C_T.

$$a = 0.0892074 \cdot C_T{}^3 + 0.0544955 \cdot C_T{}^3 + 0.251163 \cdot C_T - 0.0017077 \qquad \textbf{(5.1)}$$

The value of the induction factor as function of thrust coefficient is visualized in Figure 5.4.
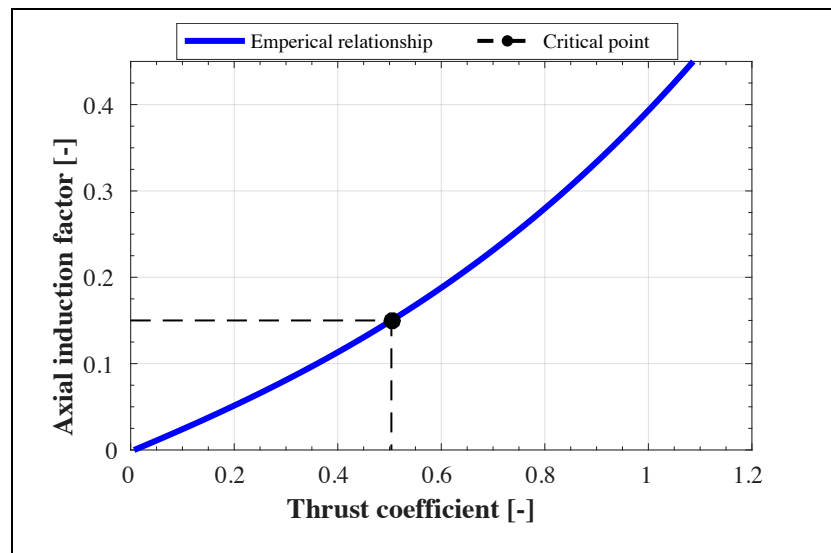
Figure 5.4: Empirical relationship between the axial induction factor and the time-averaged thrust coefficient C_T

Figure 5.5 presents the correction factor k_a as function of the axial induction factor (left) and the average thrust coefficient (right). The curves are based on Equation (2.24) for HAWC2 and Equation (2.25) for SIMO-RIFLEX-AC. Figure 5.5 points out that the correction factor at high induction factors –and thus high thrust coefficients – is lower in SIMO-RIFLEX-AC. This implies that the induced velocities computed in HAWC2 are expected to be higher than in SIMO-RIFLEX-AC. From the thrust coefficients presented later in this section, it means that the induced velocities in LC4.1 are corrected differently. The induced velocities at LC4.2 and LC4.3 are computed by the same set of equations, but the correction factor k_a in HAWC2 and SIMO-RIFLEX-AC is equal at these operating conditions.
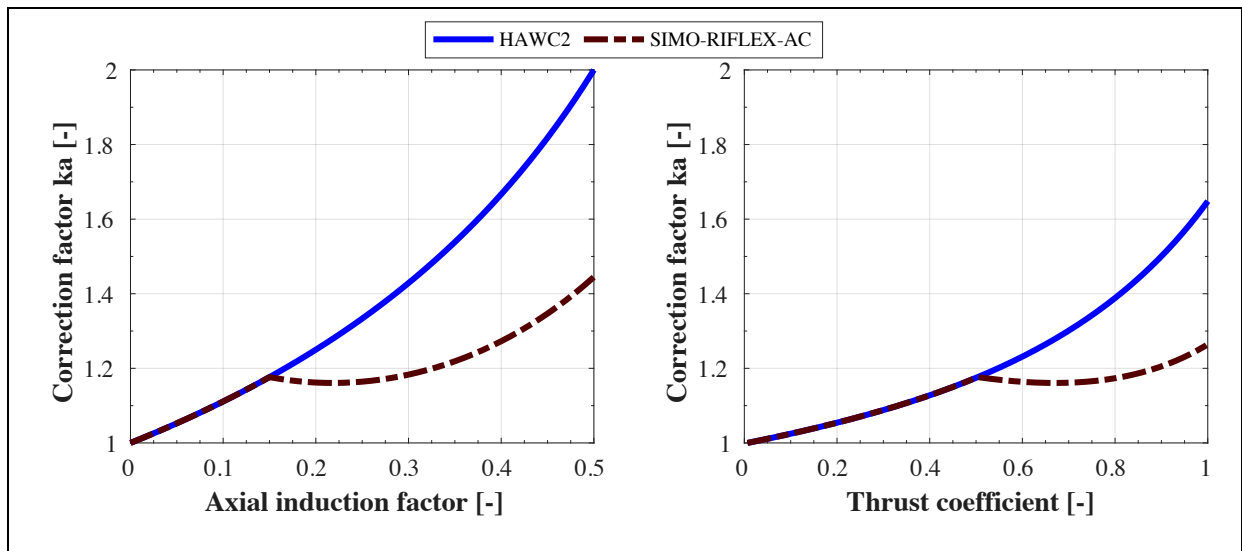
Figure 5.5: Correction factor k_a in the modified linear solution of the AC flow model, as implemented in HAWC2 and SIMO-RIFLEX-AC
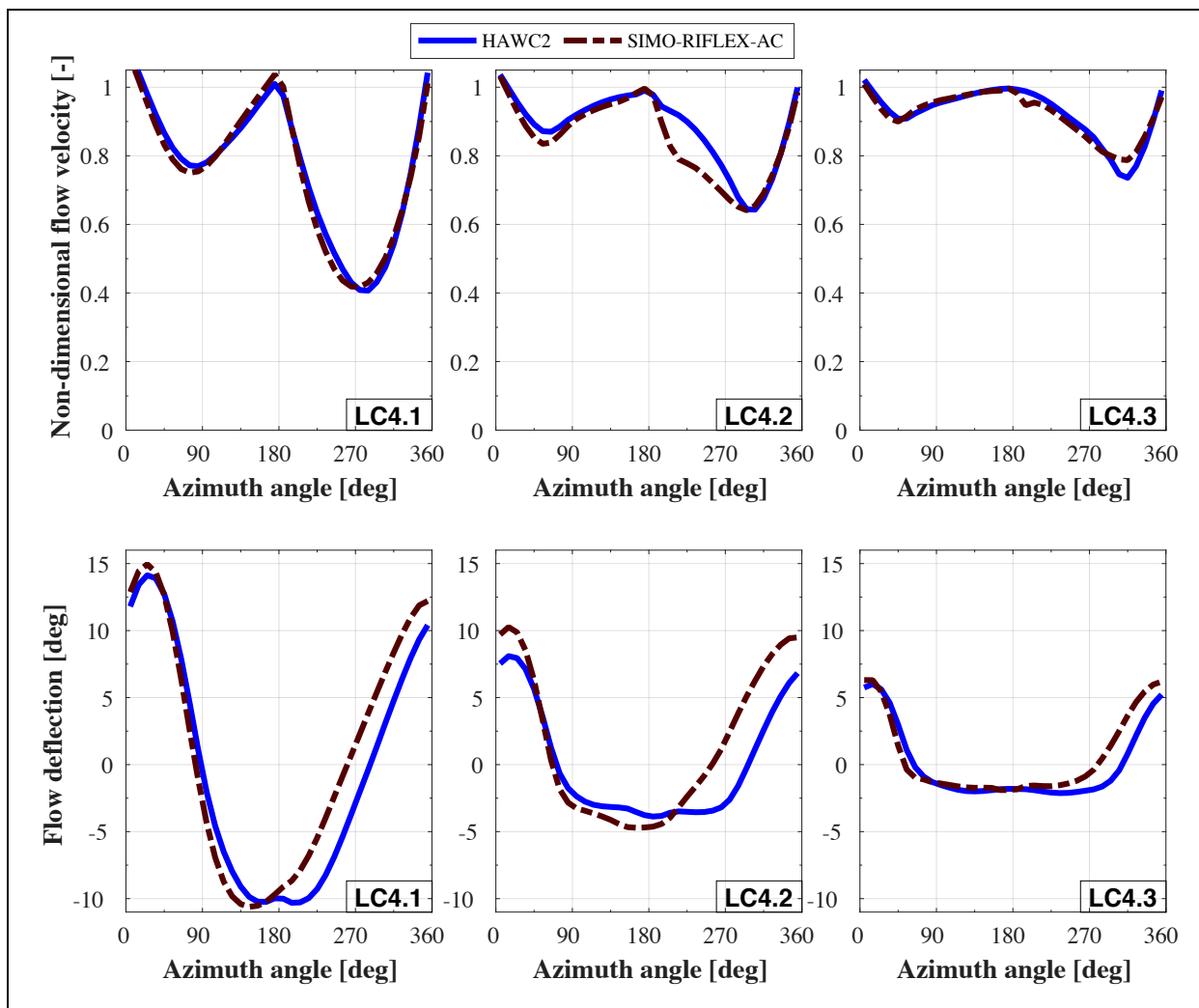
Figure 5.6: Flow velocity and deflection at the mid-blade in HAWC2 and SIMO-RIFLEX-AC (LC4)

Induced Flow Velocity Along the Rotor Periphery

The simulations in HAWC2 and SIMO-RIFLEX-AC are set up such that induction output is recorded at a desired time, for LC4 this is at 1300 s. The induction output is then computed along the whole rotor periphery using the instantaneous value of rotor speed. Upon analysis of the induced velocities in HAWC2 and SIMO-RIFLEX-AC several unexpected findings are encountered. The induced velocities are represented by flow velocity magnitude and flow deflection at the mid-blade and shown in Figure 5.6.

The velocity magnitude is very similar for both codes at LC4.1, whilst being significantly different in the downwind half of the rotor at LC4.2 and LC4.3 ($180° \leq \theta \leq 360°$). These results are notably different from the previously mentioned expectations. At this stage it is important to know the initial conditions at the time that the induction output is computed in HAWC2 and SIMO-RIFLEX-AC. The initial conditions of the land-based VAWT rotor are described by azimuth angle and rotor speed in Table 5.1.

Table 5.1: Azimuth angle of blade 1 and rotor speed at induction output (1300 s) in HAWC2 and SIMO-RIFLEX-AC (LC4)

	Azimuth angle blade 1 [deg]		Rotor speed [deg/s]	
	HAWC2	SIMO-RIFLEX-AC	HAWC2	SIMO-RIFLEX-AC
LC4.1	99.1	131.8	28.71	30.52
LC4.2	167.3	111.7	31.38	30.71
LC4.3	99.8	138.3	31.21	30.70

It is important to keep the differences in rotor speed in mind when analyzing the induction output. Whereas the rotor speed is assumed constant in computing the induction output along the rotor periphery, it actually fluctuates with the 2P frequency for a steady wind field as shown in Chapter 4.

Time Series of Aerodynamic Loads

In order to make a more valuable comparison between the aerodynamic models in HAWC2 and SIMO-RIFLEX-AC the rotor thrust and aerodynamic torque can be analyzed. The normal and tangential force on the blade elements of the VAWT rotor serve as an input to the velocity induction calculation, hence the rotor-averaged loads can potentially reveal differences in the aerodynamic models of the codes. A time series of rotor thrust in steady-state conditions is

presented in Figure 5.7. Here the results are shown at the lower wind speed of LC4.1, because this is where differences are found between HAWC2 and SIMO-RIFLEX-AC.

Figure 5.7: Rotor thrust for HAWC2 and SIMO-RIFLEX-AC (LC4.1)
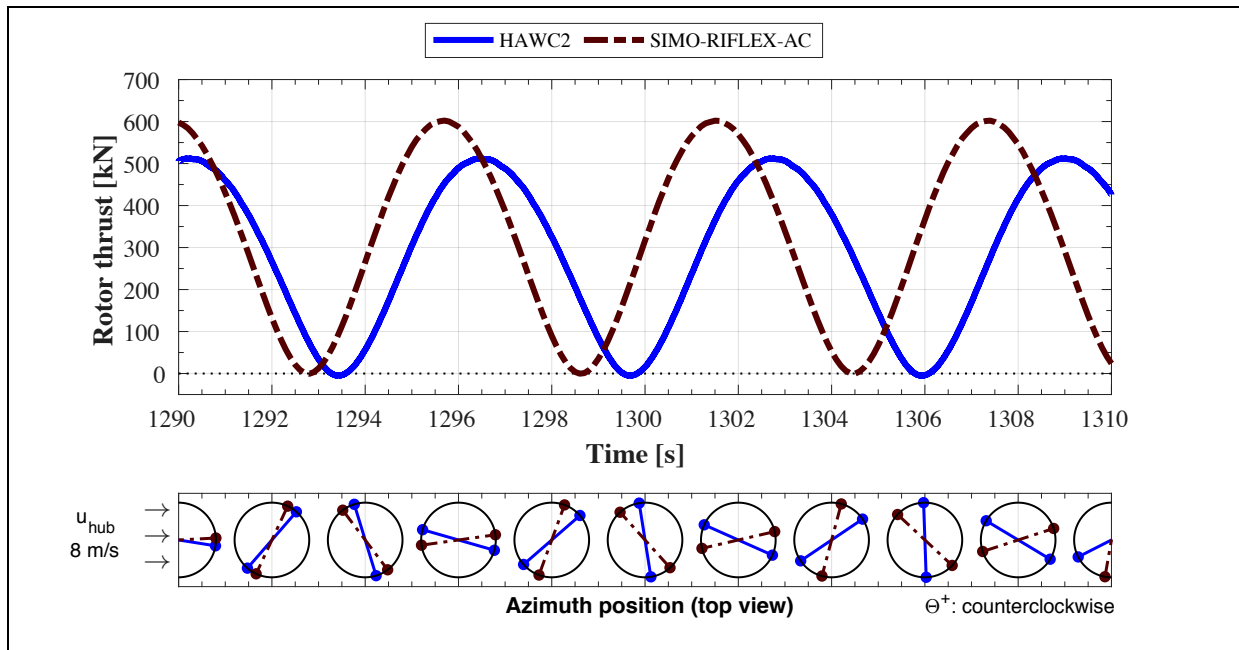
Figure 5.7 shows that rotor thrust maxima at LC4.1 are higher in SIMO-RIFLEX-AC, this is because the VAWT rotor observes higher flow velocities in the downwind half of the rotor due to a lower correction factor k_a. The aerodynamic torque, presented in Figure 5.8, shows similar behavior.
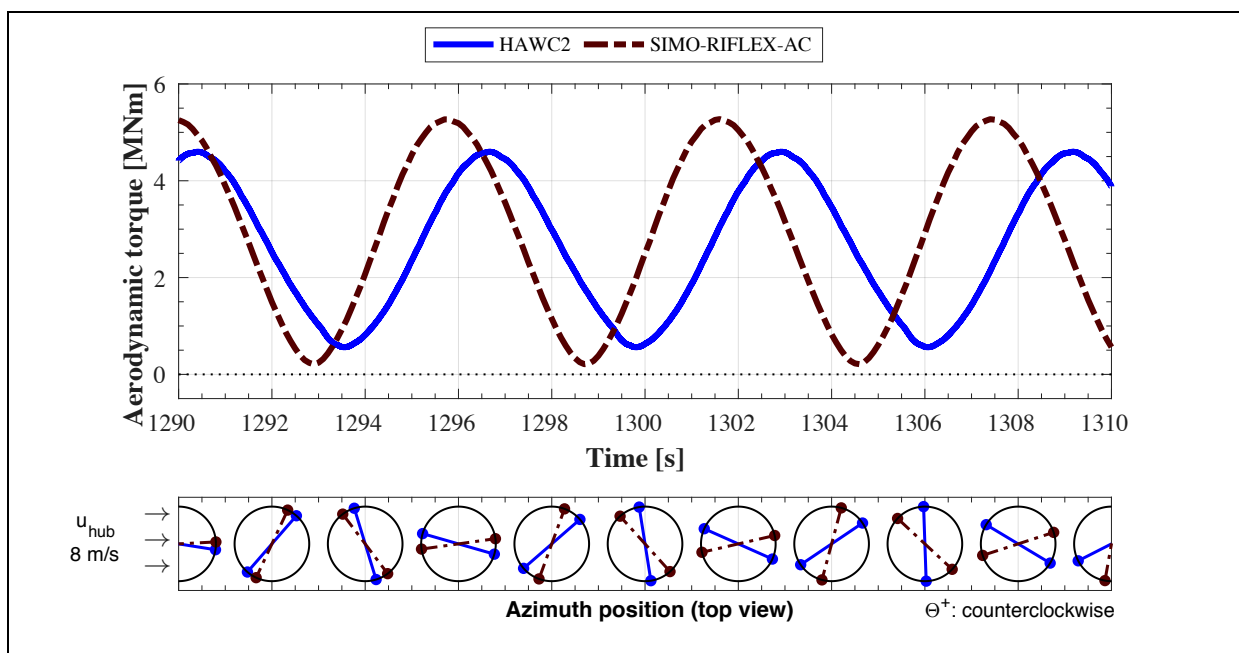
Figure 5.8: Aerodynamic torque in HAWC2 and SIMO-RIFLEX-AC (LC4.1)

The aerodynamic torque maxima in HAWC2 are lower than in SIMO-RIFLEX-AC. Additionally, the aerodynamic torque minima are higher in HAWC2 than in SIMO-RIFLEX-AC. This may point to the inclusion of the tangential terms in the modified linear solution of SIMO-RIFLEX-AC. Figure 5.8 shows that the minima in aerodynamic torque take place at the azimuth positions $\theta = 0°$ and $\theta = 180°$. At these positions the tangential terms are drag forces that accelerate the flow at $\theta = 180°$ and decelerate the flow at $\theta = 0°$. Aerodynamic drag goes with the square of the inflow velocity, hence the overall (negative) drag-induced aerodynamic torque at these azimuth positions would become larger.

Statistical Analysis of Overall Aerodynamic Loading and Performance

In the previous chapter valuable observations were made from statistical analyses. The same is done here to compare the aerodynamic loads at all environmental conditions of LC4. The mean values and standard deviations of rotor thrust and aerodynamic torque are shown in Figure 5.9.
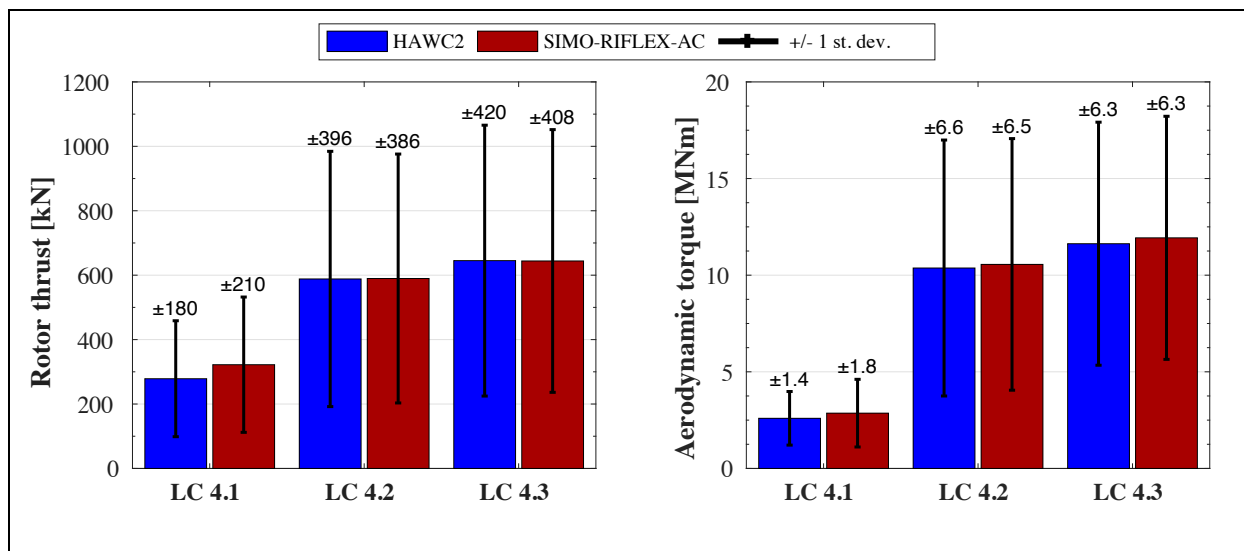
Figure 5.9: Statistics of rotor thrust and aerodynamic torque for the land-based VAWT in HAWC2 and SIMO-RIFLEX-AC (LC4)

The differences in the modified solutions to the AC flow model is notable in the mean loads. At LC4.1, the rotor thrust is higher for SIMO-RIFLEX-AC, and both codes produce a similar output at the higher wind speed of LC4.2 and LC4.3. The larger mean aerodynamic torque in SIMO-RIFLEX-AC may be related to the inclusion of tangential terms in the calculation of induced velocities.

As shown previously in Figure 5.5, the induced velocities are corrected differently for axial induction factors larger than 0.15, corresponding to an average thrust coefficient larger than 0.50. Table 5.2 shows that the thrust coefficient exceeds 0.50 in both codes only at LC4.1. The

power coefficient is also presented, which reflects the significant effect of the correction factor k_a on the calculated power output.

Table 5.2: Average thrust and power coefficient for the land-based VAWT at LC4 in HAWC2 and SIMO-RIFLEX-AC

	C_T [−]		C_p [−]	
	HAWC2	**SIMO-RIFLEX-AC**	**HAWC2**	**SIMO-RIFLEX-AC**
LC4.1	0.661	0.765	0.389	0.465
LC4.2	0.456	0.457	0.319	0.324
LC4.3	0.245	0.245	0.124	0.126

It should be noted that the results presented in Section 4.1 or for LC4 are calculated with the exclusion of the dynamic stall effect. At higher wind speeds the dynamic stall effect becomes more important and can significantly increase the aerodynamic loads on the VAWT rotor. If a dynamic stall model is included it is possible that LC4.2 (and perhaps LC4.3) would also exceed the $a \geq 0.15$ and $C_T \geq 0.50$ boundary. This would mean that the induced velocities at higher wind speeds would also be subjected to a different correction factor k_a between HAWC2 and SIMO-RIFLEX-AC.

5.2 Stepped Wind Field of LC5: Comparison of the Dynamic Stall Model

Dynamic stall is a phenomenon that occurs when the flow separates from the surface of the blade. For a VAWT it is likely to occur at low tip-speed ratios where the angle of attack changes more rapidly. Research has shown that it is essential to include the effect of dynamic stall for a more accurate prediction of the aerodynamic loads [35]. As described in Section 3.3.1, the modified Beddoes-Leishman dynamic stall model in SIMO-RIFLEX-AC should perform equal to the Stig Øye model in HAWC2. A stepped wind environment at a range of wind speeds is introduced in order to create sudden changes in the angle of attack, this environment is visualized in Section 5.2.1. The rotor speed response is compared for cases with and without dynamic stall between HAWC2 and SIMO-RIFLEX-AC in Section 5.1.2. The effect of dynamic stall is explained and compared through aerodynamic loading in Section 5.1.3.

5.2.1 Inspecting the Wind Environment

The load case designed for investigating differences in the dynamic stall model considers a stepped wind environment. The wind field is first held constant for transient effects to damp out and then followed by wind speed steps of $2\ m/s$. The wind speed at hub height is visualized by Figure 5.10.
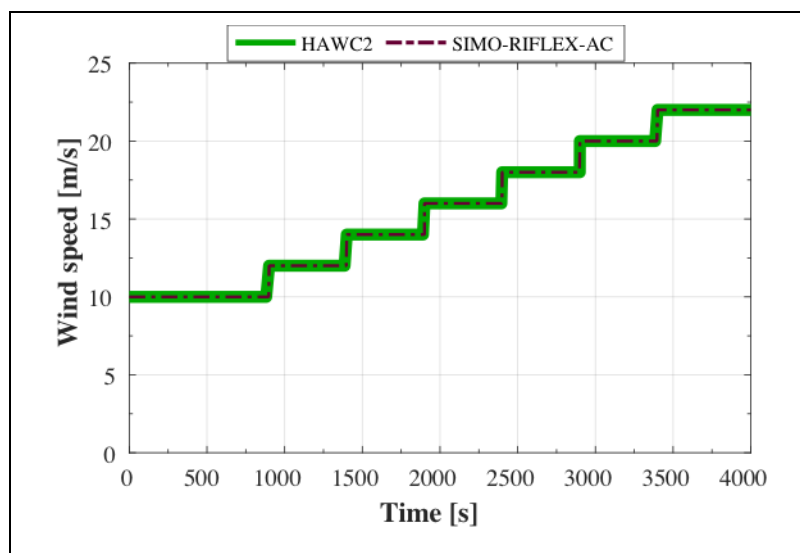

Figure 5.10: Wind speed at hub in HAWC2 and SIMO-RIFLEX-AC (LC5)

The wind environment in both codes appears to be identical. After each step the wind speed is held constant for $500\ s$, this is for the system to reach a new steady-state equilibrium before exposing the VAWT to the next wind step.

5.2.2 Response of Rotor Speed

The wind turbine model that is considered for LC5 is the rigid land-based VAWT. Again, this means that the only degree of freedom of the system is the rotation of the rotor. The resulting rotor speed is compared between the codes with and without dynamic stall in Figure 5.10.
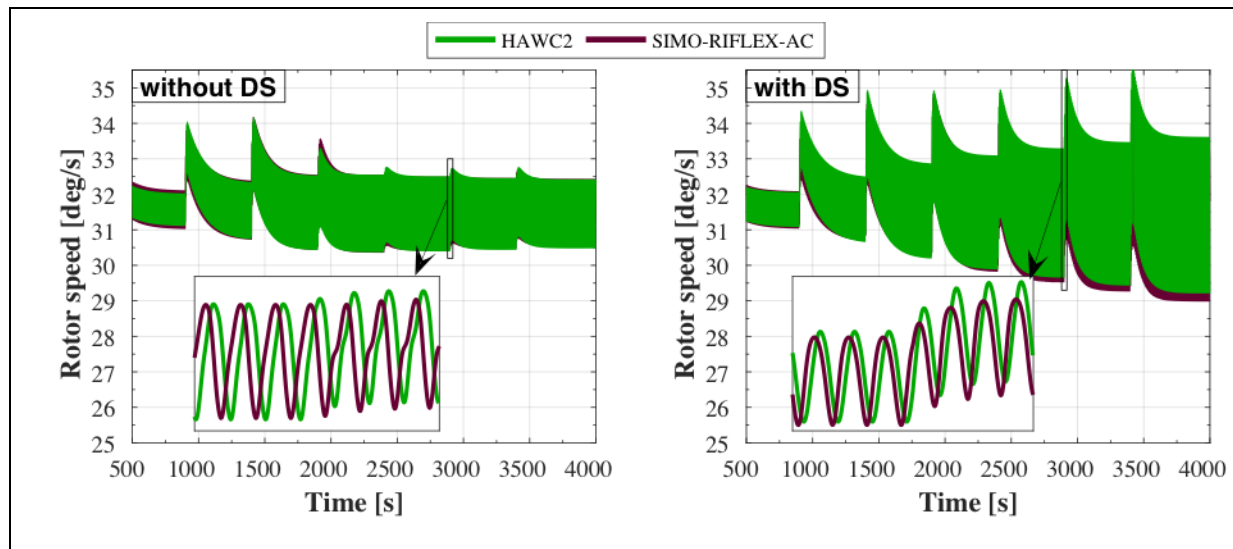
Figure 5.11: Rotor speed in HAWC2 and SIMO-RIFLEX-AC with and without dynamic stall (LC5)

The rotor speed responses agree well between the numerical codes. At high wind speeds and inclusion of dynamic stall the VAWT in HAWC2 seems to rotate slightly faster. As a general remark, the rotor speed amplitude remains fairly constant when applying no dynamic stall model. However, when including the dynamic stall effect the amplitudes increase significantly with wind speed.

The tip-speed ratio is a function of rotor speed and wind speed. Both are changing throughout LC5, hence to create a reference point the tip-speed ratio is presented against time in Figure 5.11. It is seen that the tip-speed ratio varies from approximately 3.5 at $10\,m/s$ to approximately 1.6 at $22\,m/s$.

5.2.3 Comparing the Dynamic Stall Models

As addressed previously, the Beddoes-Leishman dynamic stall model has been modified such to perform the same as the Stig Øye model in HAWC2. Ideally, the similarities and differences would be analyzed by comparison of the angle of attack and the lift- and drag coefficients in both codes right after the increase of wind speed. However, the parameters related to aerodynamics are only stored as part of the induction output at one time instant in SIMO-RIFLEX-AC. For this reason, the effect of dynamic stall will be discussed using results solely

from HAWC2. A code-to-code comparison on dynamic stall is done using the rotor-averaged aerodynamic loads.
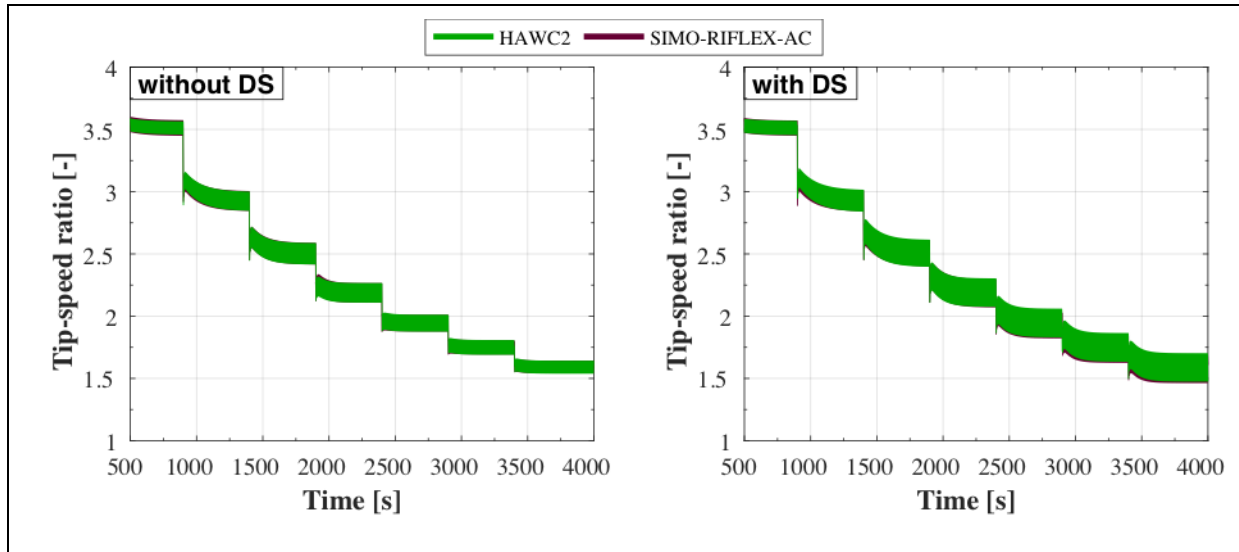
Figure 5.12: Tip-speed ratio in HAWC2 and SIMO-RIFLEX-AC with and without dynamic stall (LC5)

Effect of Dynamic Stall

For investigating the effect of dynamic stall in general, the airfoil performance coefficients are plotted as a function of angle of attack in Figure 5.13. The results are shown for the midpoint of blade 1.
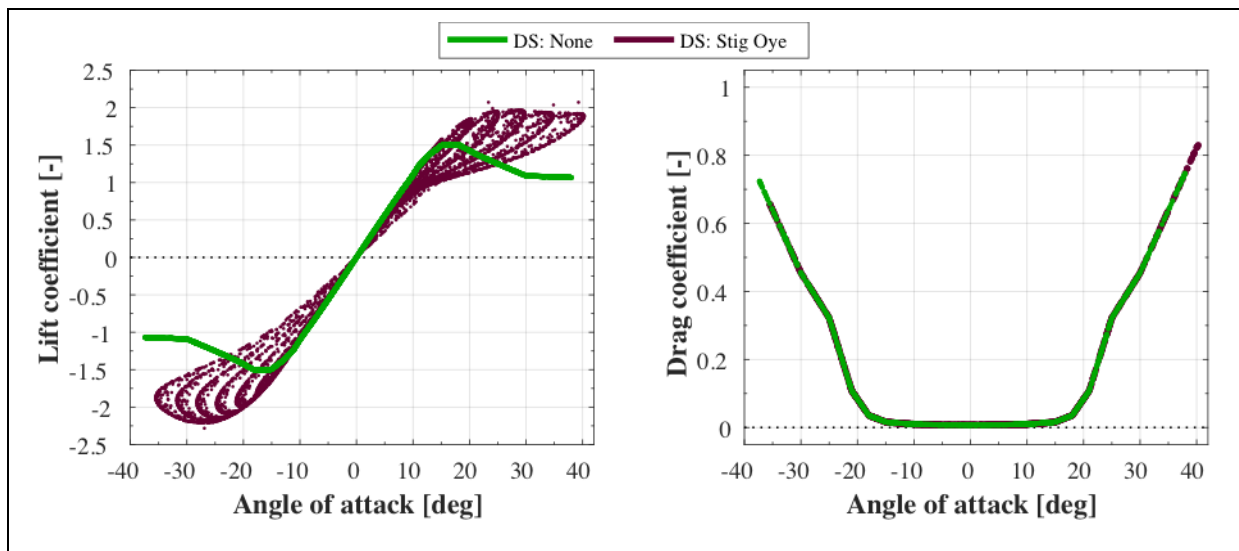
Figure 5.13: Lift- and drag coefficients against angle of attack in HAWC2 with and without dynamic stall (LC5)

It becomes evident that the dynamic stall effect is very significant when determining the lift coefficient at the larger angles of attack. The outer paths or rings in the left of Figure 5.13 represent the higher wind speed regions. At the high wind speed of $22\ m/s$, the angle of attack

at mid-blade changes from $-35°$ to $+40°$ in half a rotational period of $5.7\ s$ when considering dynamic stall. At the low wind speed of $10\ m/s$, the angle of attack ranges between $-15°$ and $+10°$. The lower wind speed gives a lift coefficient curve that is not significantly affected by dynamic stall, it agrees well with lift coefficients under static stall. The drag coefficient is unchanged when using the Stig Øye dynamic stall model, the same goes for the moment coefficients. The effect of dynamic stall on these two coefficients are not considered by the Stig Øye model. Other dynamic stall models, such as the original the Beddoes Leishman model, do include this effect.

The lift coefficient directly affects the calculation of lift force on the blade elements. The resulting lift force (per unit length) at the mid-blade can be plotted against angle of attack using data from the full time series. Figure 5.14 shows the resulting plots for the case where the dynamic stall is included and excluded.
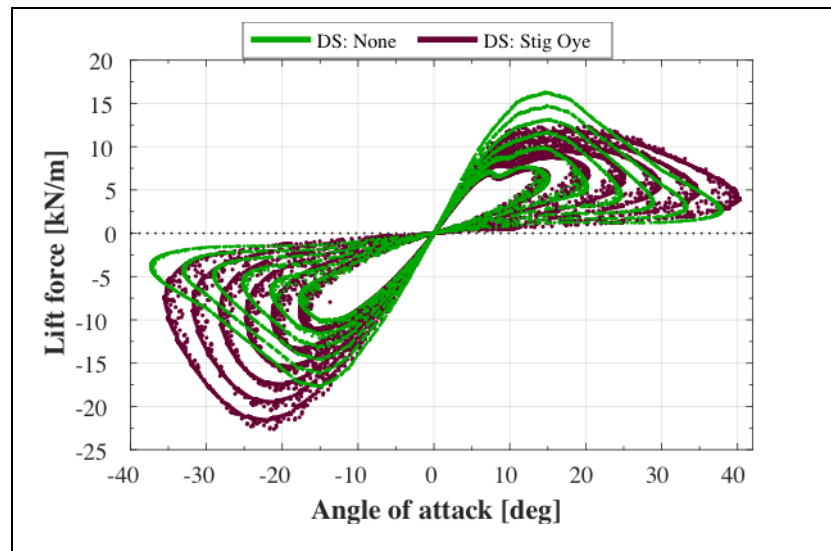
Figure 5.14: Lift force against angle of attack in HAWC2 with and without dynamic stall (LC5)

It can be seen that the effect of dynamic stall is strongest in the upwind half of the rotor, where the angle of attack is defined positive in HAWC2. Here the lift force is much reduced from the effect of flow separation at higher wind speeds (outer paths). In the downwind half of the rotor the lift forces are significantly higher when including the dynamic stall model. This is due to a lower velocity induction in the upwind half and hence a higher inflow velocity in the downwind half of the VAWT rotor.

Code-to-Code Comparison of Dynamic Stall

The performance of the dynamic stall models in HAWC2 and SIMO-RIFLEX-AC will be compared by assessment of the rotor-averaged aerodynamic loads. A time series of the rotor thrust is presented in Figure 5.15. The time series are deliberately shown in the last part of LC5, where the wind speed changes from $20\ m/s$ to $22\ m/s$
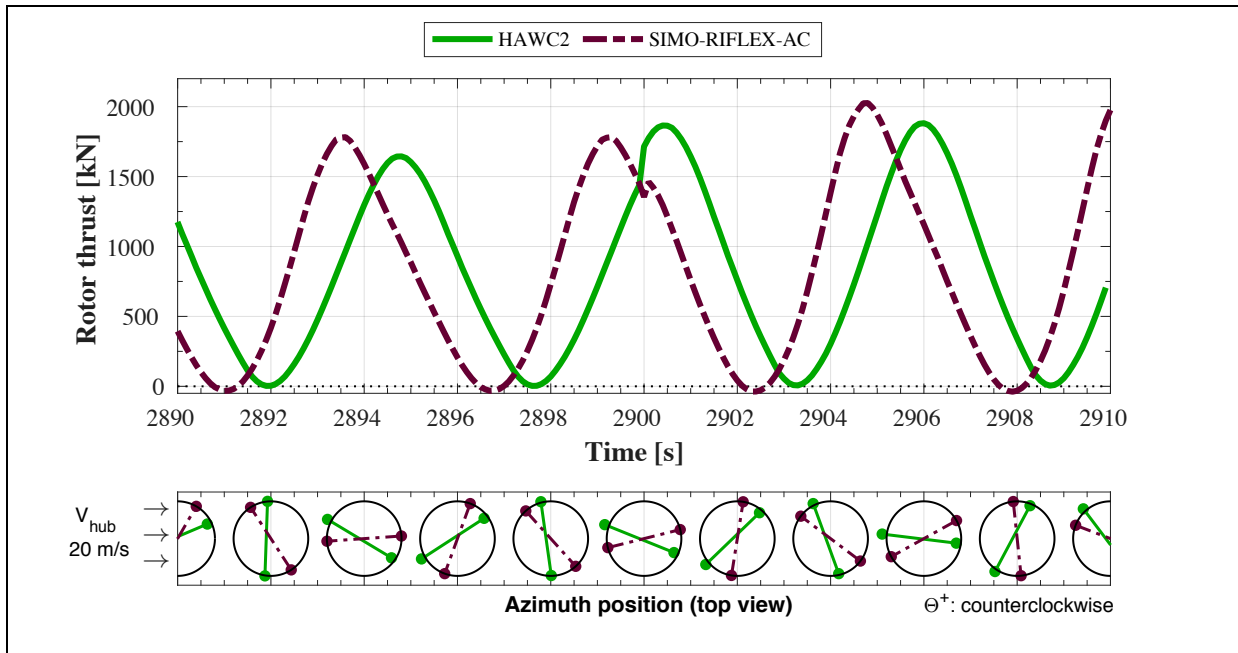
Figure 5.15: Rotor thrust in HAWC2 and SIMO-RIFLEX-AC with dynamic stall (LC5)

Generally, it is seen that the amplitude of rotor thrust is increased with the inclusion of dynamic stall when compared to the results from Section 4.1. The amplitude of rotor thrust at LC4.3 (steady wind of $20\ m/s$) was recorded at $1200\ kN$ in both codes. At LC5, the trend of rotor thrust is similar in HAWC2 and SIMO-RIFLEX-AC. The amplitude is slightly different. The aerodynamic torque acting on the VAWT rotor is shown in Figure 5.16. The same amplitude difference is found for the aerodynamic torque as for rotor thrust. It is likely that the differences between the rotor-averaged aerodynamic loads at higher wind speeds are caused by the aerodynamic models.

The step in the wind field was originally designed to compare the response between the codes from a sudden change in angle of attack. The sudden change in angle of attack occurs, but it was unforeseen that the input conditions (azimuth, rotor speed) would have to match as well for a valid comparison. An additional difference in the aerodynamic load calculation makes it more difficult to isolate the dynamic stall model. Nonetheless, a conclusion that can be made in Section 4.2 is are that the inclusion of dynamic stall induces significantly higher

117

aerodynamic loads. This can be up to a factor 2 at high wind speeds, whereas the effect is minimal at a low wind speed of $10\ m/s$. At last, the Stig Øye model and modified Beddoes-Leishman model in respectively HAWC2 and SIMO-RIFLEX-AC seem to agree. The differences observed between the codes is significantly smaller than the general difference induced by dynamic stall.

Figure 5.16: Aerodynamic torque in HAWC2 and SIMO-RIFLEX-AC at with dynamic stall (LC5)

5.3 Turbulent Wind and Irregular Waves of LC6: The Fully Coupled Codes

The last load case of this thesis work considers a fully turbulent wind field and irregular wave environment using the spar VAWT. LC6 is with regards to environmental conditions (almost) the same as LC3, although here the focus lays of comparison of the numerical tools. The spar VAWT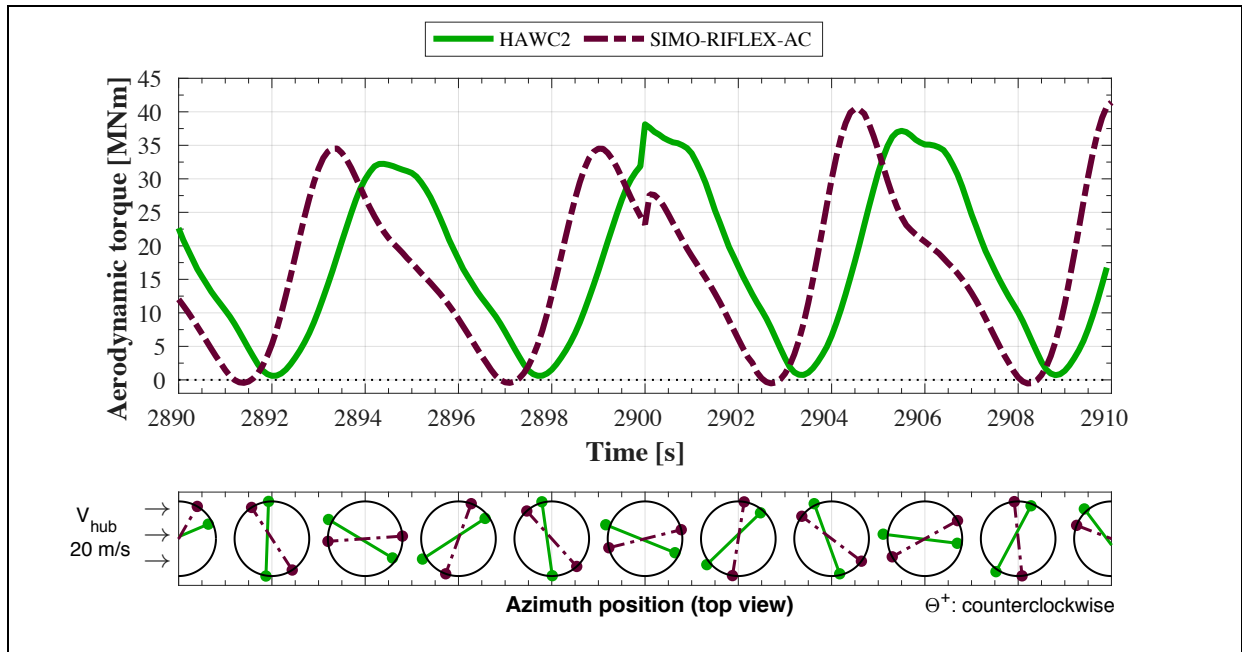 is placed in a realistic environment, hence the fully coupled capabilities of HAWC2 and SIMO-RIFLEX-AC are compared. Structural elasticity (of the rotor) and dynamic stall is both accounted for, and the rotor speed is regulated by the constant rotational speed controller. The fully coupled code comparison is structured as following. First the wind- and wave environment is compared in Section 5.1.1 to ensure that the input conditions match. Secondly, the dynamic response of the rotor and floater is analyzed in Section 5.3.2. The excitation loads are presented in Section 5.3.3 and the internal structural loads are compared in Section 5.3.4.

5.3.1 Inspecting the Wind and Wave Environment

LC6 consist of a mild, medium and severe wind environment with correlated wave conditions. Each load case is simulated for three different seeds in order to minimize stochastic effects. It is not possible to give HAWC2 and SIMO-RIFLEX-AC the exact same input conditions, because the wind and waves are generated by different programs and therefore the stochastic component cannot be matched. Also a check is performed whether the desired wind shear profile (NWP) is obtained in the turbulent wind fields of HAWC2 and SIMO-RIFLEX-AC.

Statistical Analysis of Wind Speed and Wave Elevation

The stochastic component is different in the environment of the codes, nevertheless the statistical values are specified by the input conditions of LC6 and should match. To give an impression of the wind field generated by both codes, Figure 5.17 shows the time series at LC6.2a. This describes an environment with a mean wind speed of $14\ m/s$. Throughout this last section the time series at the medium sea state of LC6.2a are presented (when possible) to provide consistency.
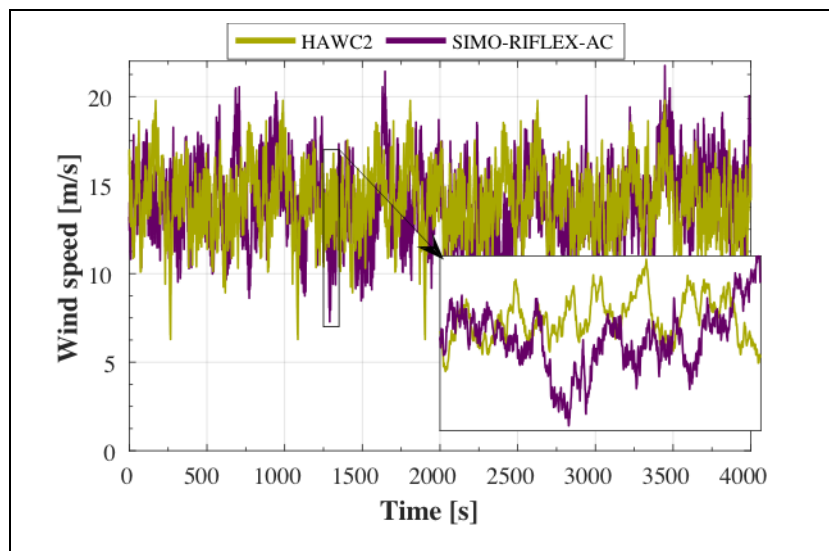
Figure 5.17: Wind environment of LC6.2a in HAWC2 and SIMO-RIFLEX-AC

When observed carefully, Figure 5.17 shows that the wind environment of HAWC2 repeats itself every $800\ s$. This is due to a limitation of the computational requirements for the internal generation of the wind field. Nevertheless, this should not have an effect on the resulting statistical values and power spectral density. The same goes for using a different set of random numbers (or seeds) in the two numerical simulations. The statistical values of the prior and other wind environments are compared between HAWC2 and TurbSim (used for SIMO-RIFLEX-AC) in Table 5.3.

Table 5.3: Statistics of instantaneous wind speed at hub height by HAWC2 and TurbSim (LC6)

		$mean(V_{hub})$ [m/s]	$\sigma(V_{hub})$ [m/s]	$min(V_{hub})$ [m/s]	$max(V_{hub})$ [m/s]
HAWC2	**LC6.1**	8.01	1.37	3.19	14.04
	LC6.2	14.00	2.00	5.55	21.92
	LC6.3	20.00	2.38	9.59	28.99
TurbSim	**LC6.1**	8.00	1.39	2.36	12.48
	LC6.2	14.00	1.93	6.28	21.32
	LC6.3	20.00	2.46	10.71	29.41

An insignificant difference is shown between the mean values and standard deviations of wind speed of the codes. From the seed sensitivity study (Section 4.3.1) it showed that this order of differences can also occur between the individual seeds.

The same comparison is made for the wave environment through wave elevation, as shown in Table 5.4. It is concluded that also the wave environment computed by HAWC2 and SIMO-RIFLEX-AC are sufficient for comparison purposes.

Table 5.4: Statistics of wave elevation by HAWC2 and SIMO-RIFLEX-AC (LC6)

		$mean(\eta)$ [m]	$\sigma(\eta)$ [m]	$min(\eta)$ [m]	$max(\eta)$ [m]
HAWC2	LC6.1	0.00	0.64	−2.89	2.85
	LC6.2	−0.00	0.90	−3.92	3.93
	LC6.3	0.00	1.22	−4.83	4.82
SIMO-RIFLEX-AC	LC6.1	0.00	0.65	−2.37	2.60
	LC6.2	0.00	0.92	−4.09	3.32
	LC6.3	−0.00	1.24	−5.41	4.46

Inspection of the Sheared Wind Profile

The statistical values of wind speed presented in Table 5.3 are measured at hub height. The variation over height or wind shear should also be checked, since this can have a severe influence on overall rotor loading. The NWP is applied in LC6, which corresponds to a power law profile with parameter $\alpha_{NWP} = 0.14$ according to the standards of IEC61400-3 edition 1 [28]. Both codes should produce the same wind speed curve against height, however, it is good to check and avoid unforeseen differences. The turbulent wind files generated by HAWC2 and TurbSim are compared with each other, but also against the NWP power law as defined by
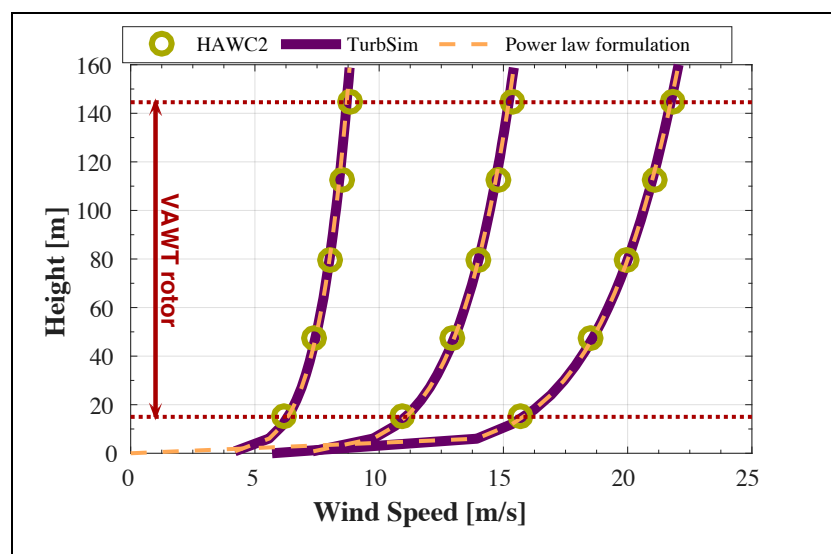

Figure 5.18: Mean wind shear in turbulent wind environment of LC6 generated by TurbSim

Equation (2.34). The result is illustrated by Figure 5.18. The five measurement points of HAWC2 agree adequately with the power law formulation. The measurements in TurbSim agree even better, except for the differences are observed close to the ground (or water). Here the power law formulation tends to $0\ m/s$ and the last measurement in TurbSim is just above the ground or water. Figure 5.18 indicates at what height the VAWT rotor is situated, and in this area the mean wind speeds are similar to the specified wind profile.

5.3.2 Global Dynamic Response

The wind-wave environment is carefully defined and the next step is to perform a dynamic analysis on the spar VAWT in both HAWC2 and SIMO-RIFLEX-AC. This section separately discussed the response of rotor speed and platform motion.

Response of Rotor Speed

The time series of rotor speed at a low and medium wind speed is shown in Figure 5.19. It should be noted that the transient duration is taken as $1000\ s$ in LC6.
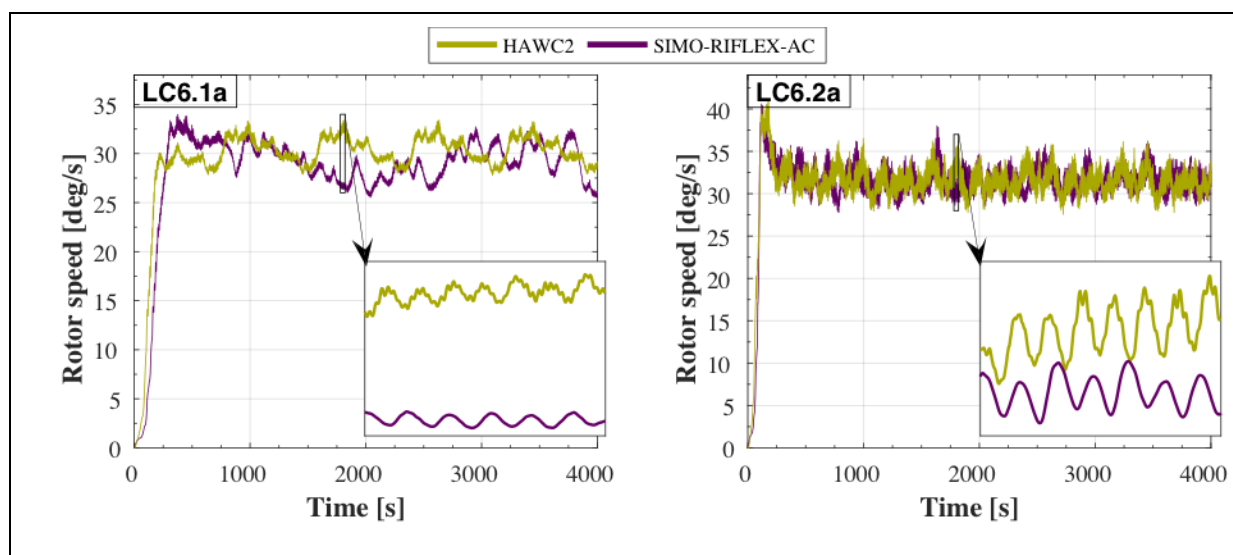
Figure 5.19: Rotor speed in HAWC2 and SIMO-RIFLEX-AC (LC6.1 and LC6.2a)

Various differences are indicated by the time series. First of all, the rotor speed response at the lower wind speed of LC6.1a (left) is more subject to variations in the wind field. This is because the VAWT mostly operates in the region before the maximum rotational speed is reached. Furthermore, the repetitive trend of the wind field of HAWC2 is found back in its rotor speed response. The smaller close ups show that the HAWC2 response contains a high frequent vibration. This can be due to a numerical instability or a higher structural mode.

When taking the statistical average of rotor speed, see Figure 5.20, it shows that the mean rotor speed in SIMO-RIFLEX-AC is lower. This is an unexpected result, because Section 4.1 pointed

out that the aerodynamic model in SIMO-RIFLEX-AC sets equilibrium at a higher rotor speed for a steady wind field of 8 m/s. Perhaps the reason can be found in the repetitive wind field of HAWC2. Due to a shorter duration the wind field has less chance to create higher (and lower) short-term mean wind speeds, which implies that the wind speed (thus rotor speed) remains closer to the specified mean value. On the contrary, the TurbSim's wind field may reach more short-term highs and lows. For rotor speed, the short-term highs are limited by maximum rotation speed, which could reduce the overall mean value. This conclusion agrees with the response in Figure 5.19.
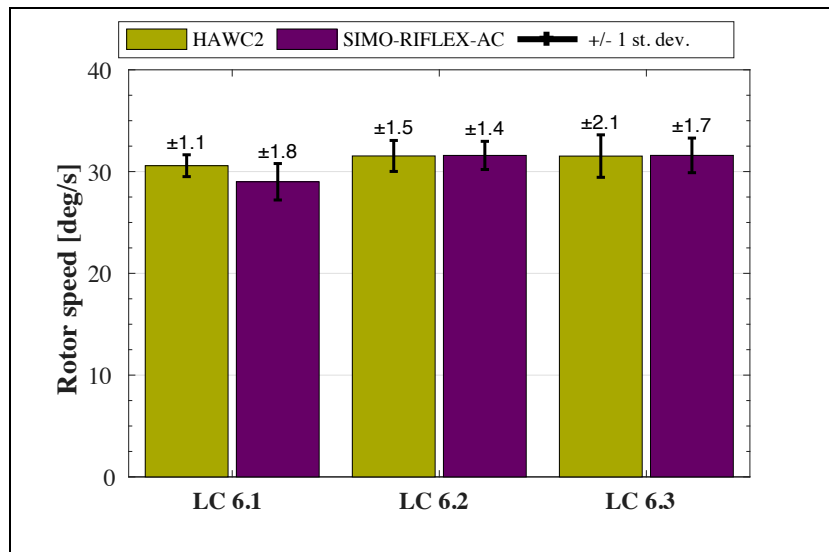
Figure 5.20: Mean value and standard deviation of rotor speed for the spar VAWT in HAWC2 and SIMO-RIFLEX-AC (LC6)

The standard deviation of the rotor speed corresponds well, a higher value at LC6.3 is observed for HAWC2. In order to learn more about the reason for this larger standard deviation spectral analysis is done. The results are presented in Figure 5.21. It shows that the wind spectrum in LC6.1 is more dominant for SIMO-RIFLEX-AC, this indicates that the wind field contains larger low-frequent variations as speculated before. On the other hand, the wind field of HAWC2 is more dominant for the rotor speed response at LC6.3. Additionally, HAWC2 shows no peak at the 1P frequency. In Chapter 4 it was concluded that the 1P peak in rotor speed is related to the yaw and/or blade response, hence the mooring system or structural model may cause the difference here. At last, a (very) small peak at 0.83 Hz and 1.02 Hz is found in the spectral density of HAWC2 that represents the high-frequent response found in Figure 5.11. It is likely related to a structural mode, because no rotor speed (1P) dependency is found when comparing this peak between LC6.1 and LC6.2/LC6.3.
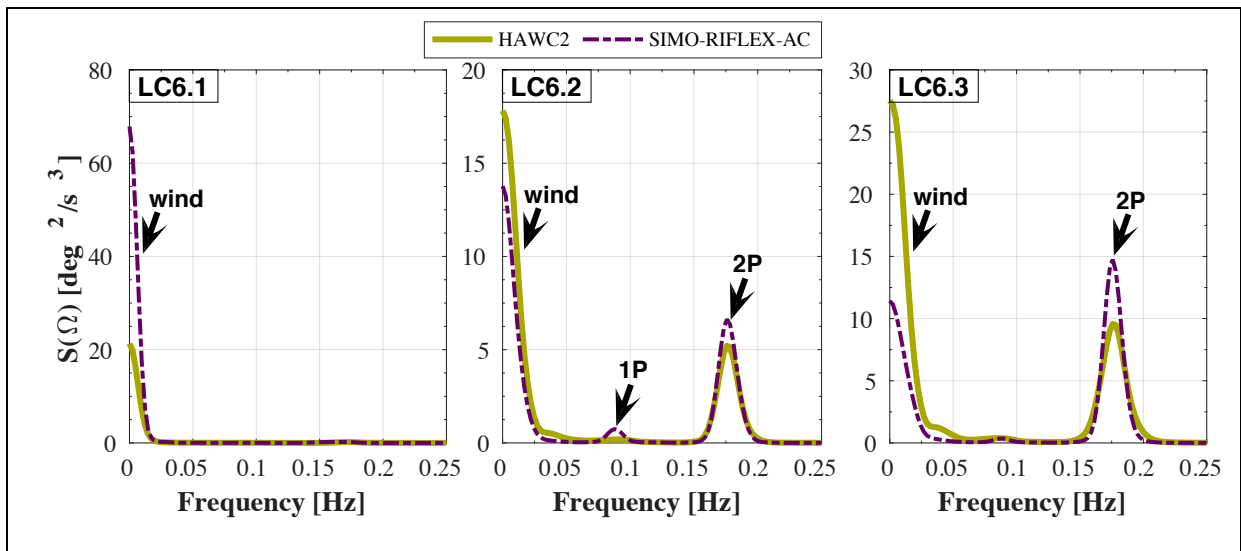
Figure 5.21: PSD of rotor speed in HAWC2 and SIMO-RIFLEX-AC (LC6)

Response of Platform Motions

The response of the spar floater in its six DOFs is described in a similar manner through statistical and spectral analysis. The platform motions are excited by aerodynamic and hydrodynamic loads, and offsets are counteracted by the restoring force from the mooring system and hydrostatic pressure differences. The results from the statistical analysis are presented in Figure 5.22.
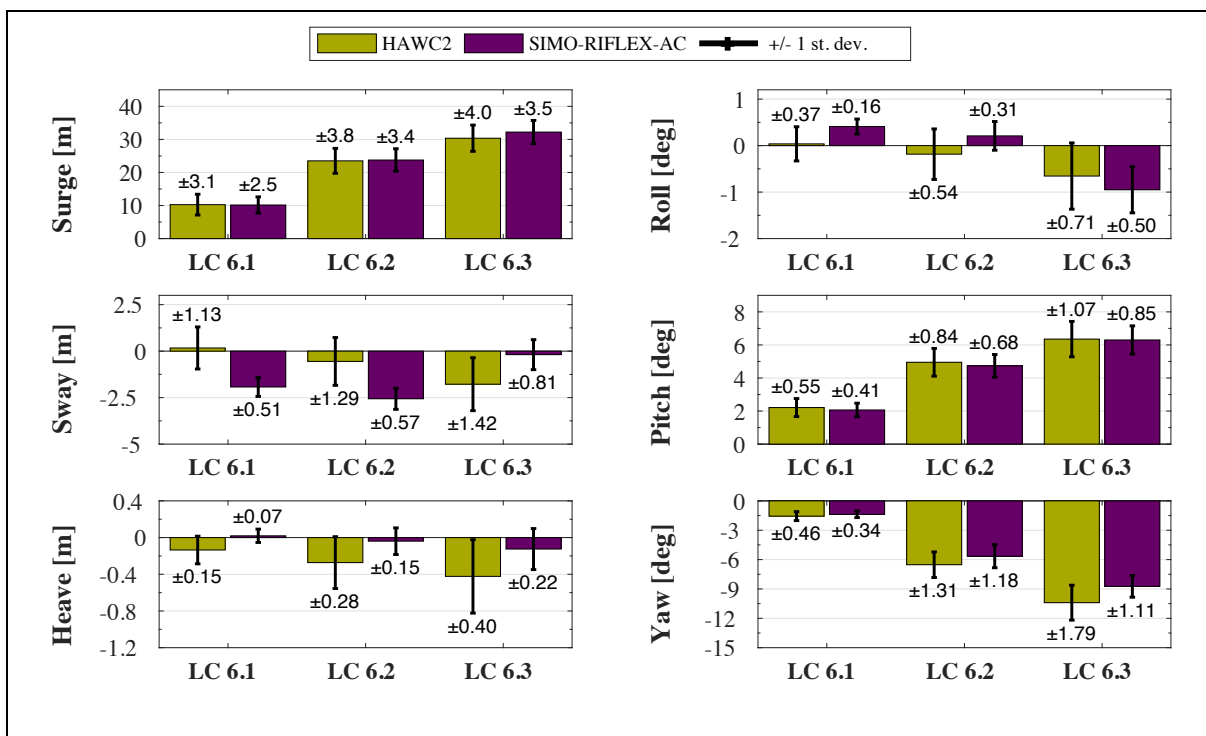
Figure 5.22: Statistics of the spar motions in HAWC2 and SIMO-RIFLEX-AC (LC6)

The platform response shows many differences, many which are likely related to the different (unphysical) mooring system of HAWC2. In general, it is observed that the platform response in HAWC2 contains a larger standard deviation in all DOFs at all load cases. The most important difference is found in heave and yaw, where also the mean offset is increased. Sway, roll and pitch are also affected.

The power spectra of the platform motions is given for LC3.2 in Figure 5.23, this tells us more about the frequency content of the energy in the response.
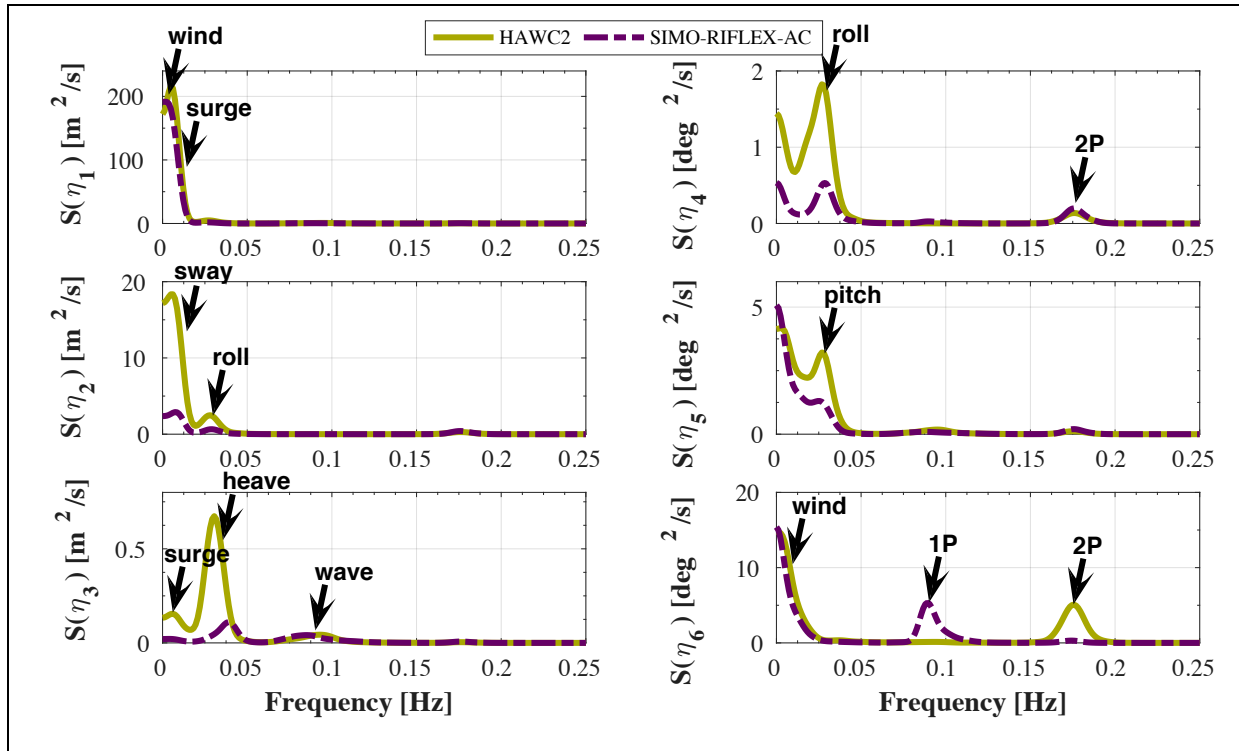
Figure 5.23: PSD of platform motions in HAWC2 and SIMO-RIFLEX-AC (LC6)

Also the spectral analysis shows interesting differences between HAWC2 and SIMO-RIFLEX-AC. The peaks in SIMO-RIFLEX-AC have already been discussed in LC3, hence comments on the peaks in HAWC2 are made here. Sway and roll show a large increase in PSD, this is likely related to the mooring stiffness. Whilst the surge responses are similar, a stronger coupling between heave and surge exists for HAWC2. This causes the heave response to be no longer dominated by the wave spectrum as was seen in SIMO-RIFLEX-AC. The yaw response is now occurring at the 2P frequency rather than the 1P frequency. The natural frequency in yaw (0.135 *Hz* for SIMO-RIFLEX-AC) may have shifted to a higher value with the differently designed mooring system in HAWC2.

5.3.3 Environmental Excitation Loads

The spar VAWT structure is excited by aerodynamic and hydrodynamic loads. It was shown in Section 4.1 that the aerodynamic model contains differences between HAWC2 and SIMO-RIFLEX-AC that are notable in the rotor-averaged loading. The aerodynamic loads in the fully coupled simulations are presented here. Due to a limitation in HAWC2 the presented output is limited to aerodynamic torque. It was shown in Section 3.3.2 that the hydrodynamic model in SIMO-RIFLEX-AC is more sophisticated and also includes second-order wave effects. Ideally, the calculated hydrodynamic loading on the spar floater would be compared here, however, the output data from both codes restricts this. The hydrodynamic loads, represented by the wave spectrum, was shown to have little effect on the platform response in LC6. Perhaps this is the reason for HAWC2 applying a simpler hydrodynamic model and benefit the computation efficiency without compromising on accuracy.

Figure 5.24 presents the aerodynamic torque acting on the rotor in the unsteady environments of LC6.1a and LC6.2a.
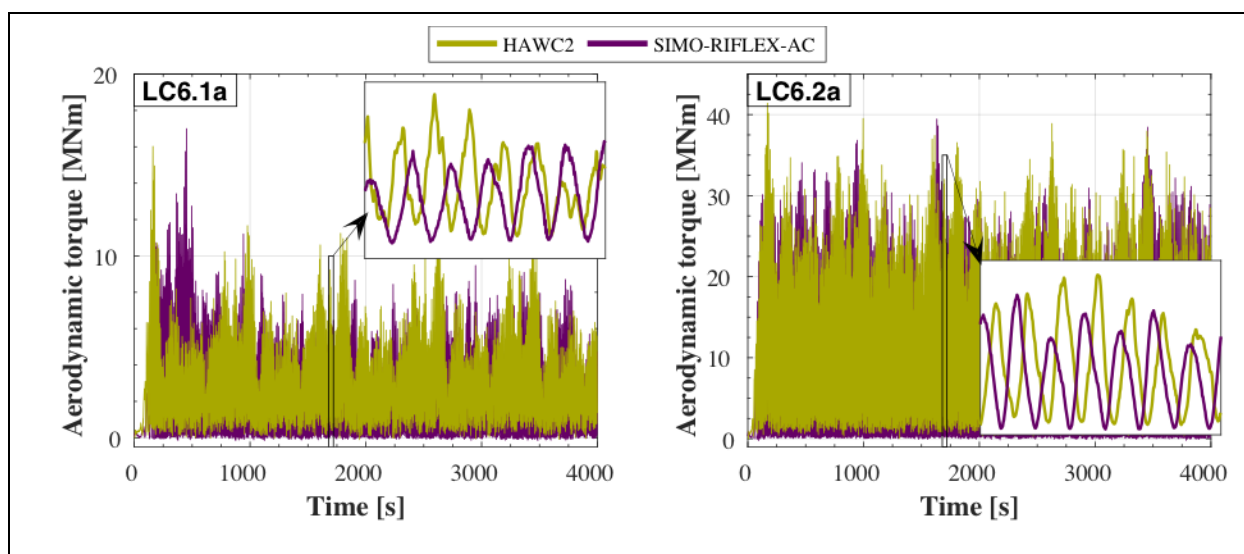
Figure 5.24: Aerodynamic torque in HAWC2 and SIMO-RIFLEX-AC (LC6.1a and LC6.2a)

Obviously the aerodynamic torque response is different in the codes, this is due to the seeds in the wind and wave environment. It seems that some of the high-frequent vibrations observed in the rotor speed response are also present in the aerodynamic torque calculated by HAWC2. However, the small variations observed in Figure 5.24 seem more stochastic and can also relate to turbulence in HAWC2's wind field at the instance of the snapshot. It can be said that in general the magnitude and variation between the codes is similar. Better comprehension on the

statistic results can be obtained through the mean values and standard deviations presented in Figure 5.25
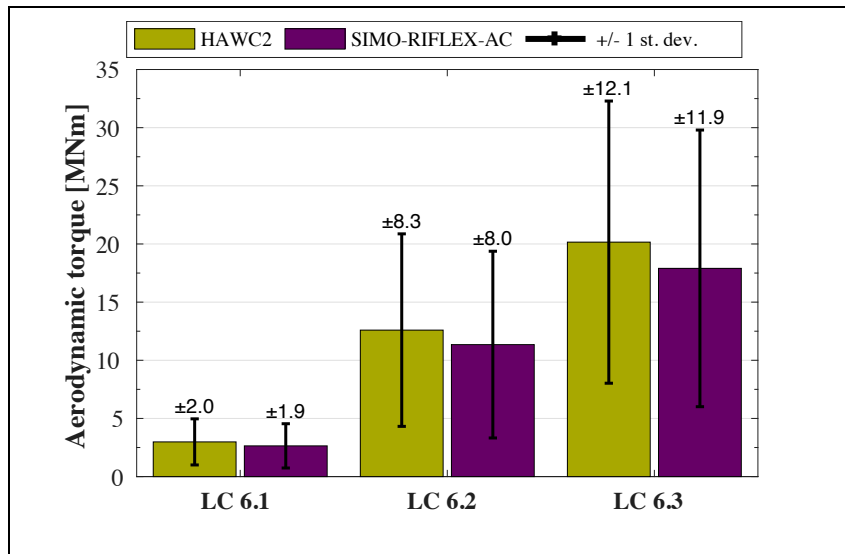
Figure 5.25: Statistics of aerodynamic torque in HAWC2 and SIMO-RIFLEX-AC (LC6)

The standard deviation of the aerodynamic torque agrees well between the codes. On the contrary, a lower mean value is observed for SIMO-RIFLEX-AC. The difference can be explained by the aerodynamic loads calculated at the 0° and 180° azimuth angles. Here the rotor-averaged aerodynamic loads tend to zero in SIMO-RIFLEX-AC, whereas HAWC calculates small positive values at the torque minima. It is concluded that this is related to the exclusion of tangential terms in the calculated induced velocities by HAWC2's aerodynamic model.

The spectral densities of aerodynamic torque are presented in Figure 5.26. The peaks are marked with the source of the frequency contents. The 2P peak at LC6.1 is wider in the SIMO-RIFLEX-AC response, this is due to a larger variation in rotor speed (thus 2P frequency). Furthermore, there is several peaks that do not come forward in one code or the other. There is the 1P response – related to yaw – that is only present for SIMO-RIFLEX-AC. The wave spectrum is found in the HAWC2 PSD at LC6.1, likely due to the stronger heave-surge coupling. At the same load case (LC6.1) structural modes are recognized around the 4P frequency in HAWC2. It was found in Section 3.2 that the eigenmodes between the codes agree well, but possibly the structural formulations cause a different significance in the aerodynamic torque response. The first lead-lag mode is found at the 4P frequency in the severe environment of LC6.3, but only in the spectral density of the SIMO-RIFLEX-AC response.
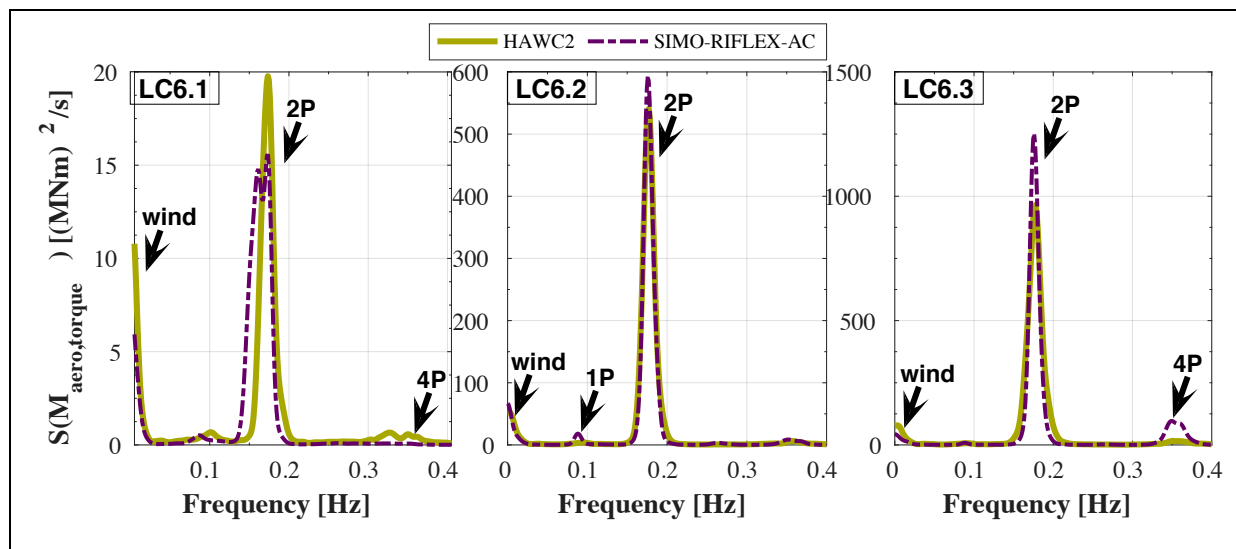
Figure 5.26: PSD of aerodynamic torque in HAWC2 and SIMO-RIFLEX-AC (LC6)

5.3.4 Internal Structural Loads

The previous results in this fully coupled code-to-code comparison showed indications of an influence by the different structural models in HAWC2 and SIMO-RIFLEX-AC. The structural impact is studied through analysis of the bending moments at the tower base and mooring line tension of the spar VAWT. Section 4.3.4 analyzed LC3 and made us understand the bending moment response at this location, hence this section mainly focusses on the differences that are observed between each numerical tool. Additionally, the resulting tensions in mooring line 1 and 2 are presented in this section. This does not directly reflect on the different structural formulations, but shows the effect of the platform motion on the mooring system.
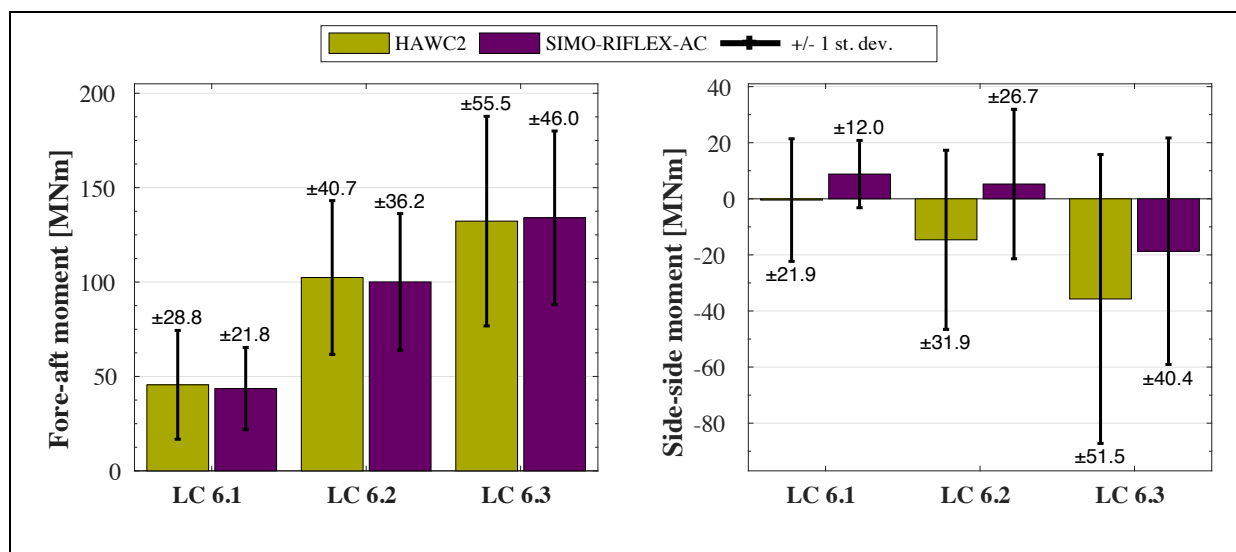
Figure 5.27: Statistics of tower base bending moment in HAWC2 and SIMO-RIFLEX-AC (LC6)

Tower Base Bending Moments

The results from statistical analysis of the moments at the tower base as presented by Figure 5.27. Both the fore-aft and side-side directions are considered here. The fore-aft bending moment shows a good agreement for the mean values, whereas the standard deviation is smaller in the SIMO-RIFLEX-AC response. The side-side moments show both higher mean values and standard deviations for HAWC2, where the mean is likely affected by the larger yaw offset that turns the side-side direction into the wind. The higher standard deviations in the tower base bending moments are partly related to the more energetic platform responses in HAWC2. However, some of the platform variation is possibly induced by the structural response in HAWC2, which is brought forward in the following.

In Chapter 4 it was brought forward that the spar VAWT reduces the tower base bending moments significantly (relative to the land-based equivalent) due to the extra DOFs introduced by the floater. Additionally, the land-based VAWT model has its first tower modes close to the 2P excitation frequency, causing a large dynamic variation. In the code-to-code comparison a similar phenomenon occurs for the spar VAWT in HAWC2, which seems to excite a tower mode of the structural rotor-spar combination. The result from spectral analysis is shown in Figure 5.28 and discussed hereafter.
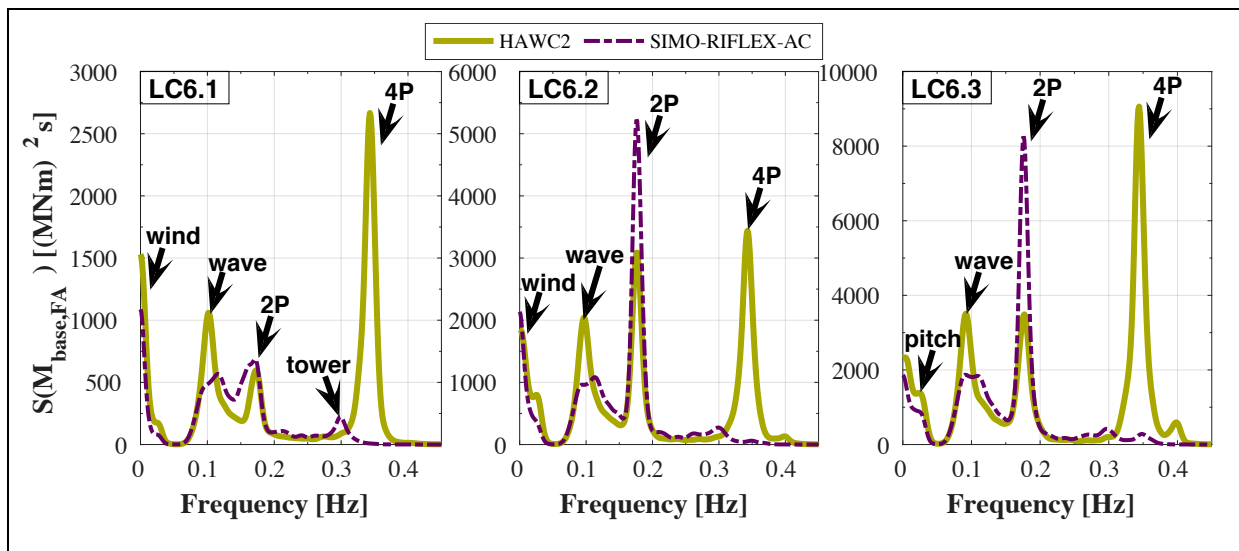
Figure 5.28: PSD of fore-aft bending moment at the tower base in HAWC2 and SIMO-RIFLEX-AC (LC6)

The power spectra show interesting variations between the responses computed by the two codes. Generally, the wave spectrum is better defined in the HAWC2 response, whereas SIMO-RIFLEX-AC contains a peak in this frequency range from the 1P effect and waves combined. The 2P effect is more strongly felt in the response by SIMO-RIFLEX-AC, whereas the spectra

in HAWC2 are dominated by a response at the 4P frequency (0.34 Hz). A similar peak was observed for the spar VAWT model in SIMO-RIFLEX-AC at 0.30 Hz, this indicates that the response is resonated by a tower mode of the spar VAWT structure with an eigenfrequency close to the 4P frequency.

Mooring Line Tension

The tension in the mooring lines are mainly governed by the response of the platform motions. The mooring system provides the stiffness for the restoring forces that keeps the spar VAWT in place. The mooring system consists of three catenary lines connected to the spar through two delta lines each, see Figure 3.3 for the reference system. Mooring line 1 is located 'behind' the spar floater when considering the streamwise direction. A time series of the tension in mooring line 1 and 2 is shown in Figure 5.29.
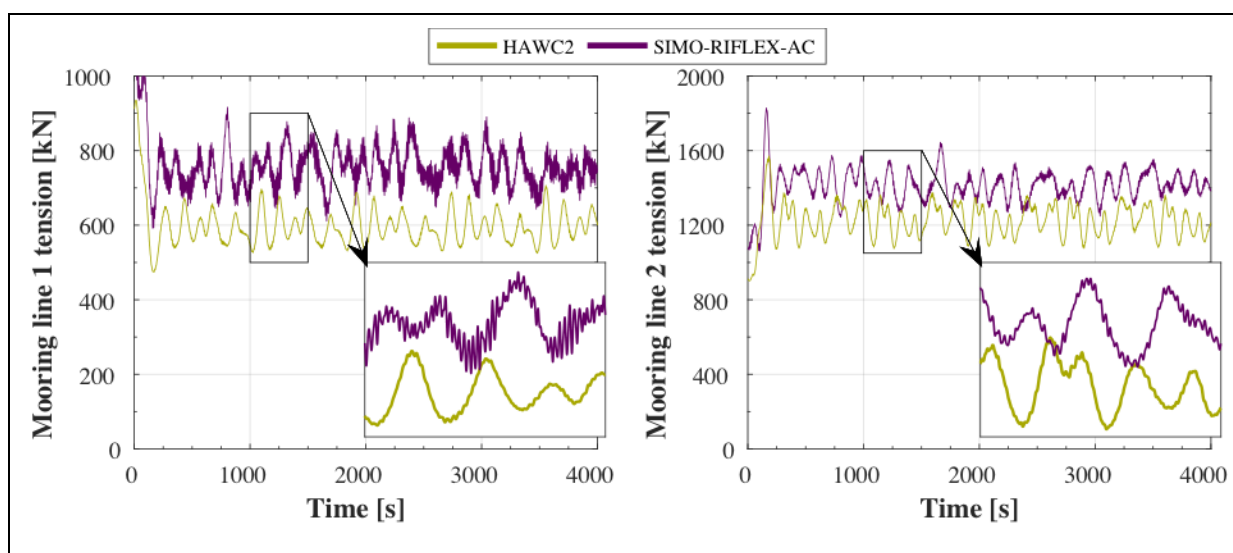
Figure 5.29: Mooring line tension in HAWC2 and SIMO-RIFLEX-AC (LC6.1a)

The response shows that the tension is governed by the surge motion, which accordingly follows the short-term mean wind speed. HAWC2 computes a lower tension than SIMO-RIFLEX-AC in the mild wind-wave environment of LC6.1a. A vibration-like response can be seen in tension of SIMO-RIFLEX-AC, this is likely related to the spar's yaw response. The results from statistic analysis is presented by Figure 5.30. An interesting finding is made with respect to the mean values. The mean values are lower for HAWC2 in both mooring lines at all load cases. This could be related to the fact that no hydrodynamic loads are acting on the mooring lines in HAWC2. As mentioned before, the mooring system is modelled by a set of matrices. On the contrary, SIMO-RIFLEX-AC models a physical mooring system from non-linear bar elements that are subjected to hydrodynamic loads as calculated by the Morison

equation. The exclusion of hydrodynamic loads in HAWC2 is also likely to be responsible for a lower standard deviation in the tension of mooring line 1. The standard deviation of the tension in mooring line 2 is higher for HAWC2. This may be related to the more energetic response of the spar platform.
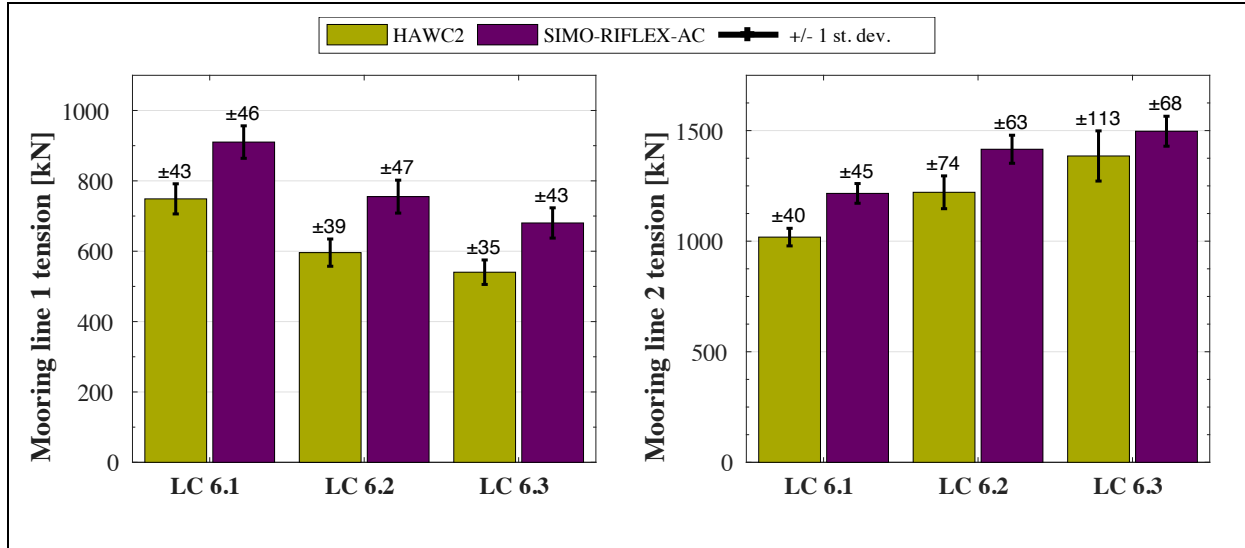
Figure 5.30: Statistics of mooring line tension in HAWC2 and SIMO-RIFLEX-AC (LC6)

6 Conclusions and Recommendations

This thesis deals with understanding the dynamic response characteristics of a spar VAWT and analyzes the fully coupled methods that can model this floating concept. A solid basis of understanding is created by comparison of the spar VAWT with an equivalent land-based VAWT in a variety of (un)steady wind- and wave environments. The numerical tool that is used for performing the fully coupled aero-hydro-servo-elastic simulations is SIMO-RIFLEX-AC, a verified code with its aerodynamic model based on the AC flow theory. The implementation of this theory – and modeling methods of other physical phenomena – is subjected to a code-to-code comparison against HAWC2. This is done through dynamic analysis of the rigid land-based VAWT in steady wind environments and the spar VAWT in unsteady wind-wave environments. This chapter presents the conclusions of the work related to the VAWT model comparison in Section 0 and the code-to-code comparison in Section 0. The recommendations for future work are given in Section 6.3.

6.1 Conclusions from Investigating the Spar VAWT Characteristics

The basic understanding is formed from a steady wind-only environment at wind speeds in the full operational range of the VAWT rotor. The structure is excited by aerodynamic loads that oscillate with a 2P frequency from zero to a maximum value. The 2P effect is found in the rotor speed response, whereas the yaw motion of the spar floater absorbs some of the energy and responds with the 1P frequency. The aerodynamic thrust excites the first tower mode of the land-based VAWT, an effect that is strongly reduced by the spar VAWT. Rotor thrust also causes tower tilt, which in return decreases the aerodynamic loading and introduces additional gravitational loads at the tower base and mid-blade. The flatwise blade bending moments are mainly governed by gravity, whereas lead-lag blade bending moments are mostly induced by aerodynamic torque. Mean platform offsets can be significant at higher wind speeds, up to 38.9 m for surge, 7.5° for pitch and 10.0° for yaw. The 1P yaw response and mean tower tilt ultimately affects the generator power, which is 4.9% lower at cut-out wind speed as compared to the land-based VAWT.

Irregular waves are introduced to investigate the influence of hydrodynamic loading on the dynamic response. The stochastic components in the wave environment add excitation loads on the spar floater in a broader frequency range. The wave-induced platform response is mostly

noticeable in heave and strengthens the 1P effect in surge and pitch, which increases the 2P effect in the fore-aft tower base bending moments by a factor up to 2.1 with respect to its standard deviation. The flatwise blade bending moments are also affected by the wave-induced response, mostly for low wind speeds.

Turbulence in the wind field introduces extra frequency content in the aerodynamic excitation loads that significantly affect the dynamic response of the spar VAWT. The 2P effect is reduced, but standard deviations increase with a factor up to 8 for rotor speed, 10 for surge and 3 for pitch. The increased platform response also brought forward motion coupling in surge-heave and sway-roll. The variation of wind speed in space and time (turbulence) decreases the variation of rotor-averaged aerodynamic loads, the standard deviation is reduced by 4.2% for rotor thrust and 10.7% for aerodynamic torque.

6.2 Conclusions from the Code-to-Code Comparison

Before performing dynamic analysis in HAWC2 and SIMO-RIFLEX-AC, the generation of the wind and wave fields is inspected to ensure the land-based and spar VAWT are subjected to similar input conditions. It is concluded that wind turbulence, wind shear and waves are modeled correctly. The first part of the code-to-code comparison isolates the aerodynamic model, the different implementation of the AC flow theory is notable at the tip-speed ratio of approximately 4.0. The induced velocities in the codes are corrected differently, causing lower mean aerodynamic loads in HAWC2 in a steady wind environment. The aerodynamic torque is generally higher in SIMO-RIFLEX-AC at all tip-speed ratios, which can be related to the inclusion of tangential terms.

The effect of dynamic stall is studied through a stepped wind field. Dynamic stall significantly amplifies the 2P effect on rotor speed and becomes increasingly important at lower tip-speed ratios. Using the Stig Øye model it is shown that the lift force at the mid-blade is decreased in the upwind rotor half and increased in the downwind half. Comparison of the dynamic stall models in HAWC2 and SIMO-RIFLEX-AC shows in general a good agreement, but output parameters and the influence of the aerodynamic models constrained a detailed analysis.

The fully coupled capabilities of the numerical tools are compared by placing the spar VAWT in realistic environments. Analysis of the platform motions shows higher standard deviations in all DOFs for HAWC2, also a stronger coupling in surge-heave and sway-roll is found. The yaw response is at 1P in SIMO-RIFLEX-AC and at 2P in HAWC2. Differences in the platform response is likely related to the mooring system design. The introduction of turbulent wind

shows higher mean aerodynamic torque for HAWC2, whereas this was opposite in the steady wind cases. With respect to the internal structural loads, HAWC2 models larger tower base bending moments and shows a larger wave-induced response. A concentration of energy at the 4P frequency is found in the PSD of the fore-aft moment. This could indicate the first tower mode of the rotor-spar combination is around 0.34 Hz in HAWC2, where a similar peak is found at 0.30 Hz in SIMO-RIFLEX-AC. The mooring line tension in SIMO-RIFLEX-AC is higher in mean value but generally lower in standard deviation. This can be related to the less energetic platform response (standard deviation) and the inclusion of hydrodynamic loads on the mooring lines (mean) in SIMO-RIFLEX-AC.

At last a comment on computational efficiency of the numeral tools. HAWC2 is approximately 2 to 3 times faster than SIMO-RIFLEX-AC, but is also more storage intensive due to saving the output parameters at every time step.

6.3 Recommendations for Future Work

There is many fields and modeling methods in the dynamic analysis of floating VAWTs that remain uncertainties, such as the aerodynamic and dynamic stall phenomena. This thesis included a comparison in fully coupled methods of one code to another, because limited experimental data is available. It would be interesting to verify the numerical tools with field tests at the multi-megawatt scale.

Until such field measurements are available, it is required to perform research with the currently available tools. This study addressed the differences in the hydrodynamic models of HAWC2 and SIMO-RIFLEX-AC, but analysis on the induced responses was limited by the dominant aerodynamic loading. A load case with an isolated hydrodynamic model could be designed for this. Also the effect of the non-physical mooring system in HAWC2 could be addressed in future work. In such study it would be desirable to subject the spar floater and mooring system to the exact same environmental conditions, which requires an extension in the compatibility of the codes.

With regards to the aerodynamics it is seen that the modeling of dynamic stall and dynamic inflow has a significant influence. It would benefit the accuracy of the aerodynamic load prediction if methods are developed for modeling these unsteady phenomena specifically for VAWTs. Here is is important that the aerodynamic model used is accurate and that the method is also sufficiently efficient for implementation in fully coupled time-domain analysis.

This thesis work brought forward a couple of aspects that can be used in further developing the spar VAWT model. First of all, a reduction in the dominant 2P loading can be realized by inclusion of more blades and/or introducing a helical shape. The influence of multiple blades in a H-type rotor is addressed in recent research, this can be extended by studying the effect of helical shaped blades. The 2P effect excites the tower modes of the land-based VAWT. If the current design is converted to an onshore concept, the inclusion of stiffening guy wires should be considered. Simulations using the spar VAWT showed a strong structural response at the tower base of around $0.30\,Hz$, a frequency that is not observed in the land-based VAWT response. It would be interesting to perform a modal analysis on the spar VAWT, and investigate the response characteristics around this frequency. The spar floater is originally designed for a HAWT concept, general optimization can be done to improve the dynamic behavior of the floating VAWT.

References

[1] The European Wind Energy Association, "Wind in Power: 2015 European statistics," 2016.

[2] Z. Cheng, "Integrated Dynamic Analysis of Floating Vertical Axis Wind Turbines," Norwegian University of Science and Technology, Trondheim, Norway, 2016.

[3] L. Vita, "Offshore Vertical Axis Wind Turbines with Rotating Platform," Technical University of Denmark, Kgs. Lyngby, Denmark, 2011.

[4] MODEC, "[skwíd]," MODEC Inc, 02 2013. [Online]. Available: http://www.modec.com/fps/skwid/pdf/skwid.pdf. [Accessed 22 09 2016].

[5] EOLFI, "SPINFLOAT, FLOATING VAWT," EOLFI, [Online]. Available: https://www.eolfi.com/fr/eolfi-recherche-developpement/spinfloat. [Accessed 22 09 2016].

[6] K. Wang, T. Moan and M. O. L. Hansen, "Stochastic dynamic response analysis of a floating vertical-axis wind turbine with a semi-submersible floater," *Wind Energ.,* 2015.

[7] A. V. Metrikine, *Dynamics, Slender Structures and an Introduction to Continuum Mechanics CT 4145,* Delft: Delft University of Technology, 2015.

[8] MARINTEK, "RIFLEX Theory Manual," MARINTEK, Trondheim, 2012.

[9] A. Shabana, Dynamics of multibody systems (2nd edition), Cambridge: Cambridge University Press, 1998.

[10] Bbanerje, "Wikimedia Commons," 11 12 2012. [Online]. Available: https://commons.wikimedia.org/wiki/File:TimoshenkoBeam.svg. [Accessed 12 09 2016].

[11] T. J. Larsen and A. M. Hansen, *How 2 Hawc2, the user's manual,* Roskilde, Denmark: Risø DTU Wind Energy, 2009.

[12] A. Mabrich, "Bentley RM Bridge Seismic Design and Analysis," 10 2015. [Online]. Available: http://slideplayer.com/slide/7654402/. [Accessed 13 09 2016].

[13] P. C. Klimas, "Darrieus Rotor Aerodynamics," *Journal of Solar Engineering,* vol. 104, pp. 102-105, May 1982.

[14] K. Wang, "Modelling and dynamic analysis of a semi-submersible floating vertical axis wind turbine," Norwegian University of Science and Technology, Trondheim, Norway, 2015.

[15] I. Paraschivoiu, "Double-multiple streamtube model for studying vertical-axis wind turbines," *Journal of Propulsion and Power,* pp. 370-377, 1988.

[16] I. Paraschivoiu, Wind Turbine Design: With Emphasis on Darrieus Concept, Montreal: Polytechnic International Press, 2002.

[17] M. T. Brahimi and I. Paraschivoiu, "Darrieus Rotor Aerodynamics in Turbulent Wind," *Journal of Solar Energy Engineering,* vol. 117, pp. 128-136, May 1995.

[18] K. Wang, M. O. L. Hansen and T. Moan, "Model improvements for evaluating the effect of tower tilting on the aerodynamics of a vertical axis wind turbine," *Wind Energ. Wind Energy,* 2013.

[19] H. A. Madsen, "The Actuator Cylinder - A Flow Model for Vertical Axis Wind Turbines," The Institute of Industrial Constructions and Energy Technology, Aalborg, Denmark, 1982.

[20] H. A. Madsen, T. J. Larsen, U. S. Paulsen and L. Vita, "Implementation of the Actuator Cylinder Flow Model in the HAWC2 code for Aeroelastic Simulations on Vertical Axis Wind Turbines," in *51st AIAA Aerospace Sciences Meeting including the New Horizons Forum and Aerospace Exposition*, Grapevine, Texas, 2013.

[21] Z. Cheng, H. A. Madsen, Z. Gao and T. Moan, "Aerodynamic modeling of floating vertical axis wind turbines using the actuator cylinder flow method," *Submitted to Energy Procedia,* 2016.

[22] T. J. Larsen and H. A. Madsen, "On the way to reliable load simulation on VAWT's," in *Proceedings of EWEA 2013*, Vienna, Austria, 2013.

[23] C. S. Ferreira, H. A. Madsen, M. Barone, B. Roscher, P. Deglaire and I. Arduin, "Comparison of aerodynamic models for Vertical Axis Wind Turbines," *Journal of Physics: Conference Series,* vol. 524, 2014.

[24] M. O. L. Hansen, Aerodynamics of Wind Turbines, 2nd Edition ed., Earthscan, 2008.

[25] Z. Cheng, H. A. Madsen, Z. Gao and T. Moan, "A fully coupled method for numerical modeling and dynamic analysis of oating vertical axis wind turbines," *Submitted to Renewable Energy,* 2016.

[26] Department of Wind Energy DTU, *Wind - a brief overview,* Roskilde, 2015.

[27] W. Bierbooms, *Offshore Wind Climate,* Delft: TU Delft - guest lecture at OE5662, 2015.

[28] Dansk Standard, "Wind turbines - Part 3: Design requirements for offshore wind turbines," IEC 61400-3, Copenhagen, 2009.

[29] DNV-OJ-J101, "OFF SHORE STANDARD: Design of offshore wind turbine structures," DNV, 2007.

[30] Dansk Standard, "Wind turbines - Part 1: Design requirements," IEC61400-1, Copenhagen, 2005.

[31] N. Sørensen and H. A. Madsen, "Modelling of transient wind turbine loads during pitch motion," in *Online Proceedings. European Wind Energy Conference and Exhibition*, Athens, Greece, 2006.

[32] O. de Vries, "Fluid Dynamic Aspects of Wind Energy Conversion," AGARD, Neuilly-sur-Seine, France, 1979.

[33] T. Theodorsen, "General theory of aerodynamic instability and the mechanism of flutter," in *NACA report no 496*, National Advisory Committee for Aeronautics, 1935, pp. 413-433.

[34] J. G. Leishman, Principles of Helicopter Aerodynamics, New York: Cambridge University Press, 2000.

[35] S. Øye, "Dynamic stall, simulated as a time lag of separation," in *Proceedings of the 4th IEASymposium on the Aerodynamics of Wind Turbines*, Harwell, UK, 1991.

[36] D. Castelein, "Dynamic Stall on Vertical Axis Wind Turbines," Technical University of Delft, Delft, 2015.

[37] P. Crimi, Dynamic stall, California: North Atlantic Treaty Organization, Advisory Group for Aerospace Research and Development, 1973.

[38] O. M. Faltinsen, Sea Loads on Ships and Offshore Structures, Cambridge University Press, 1993.

[39] W. J. Pierson and L. A. Moskowitz, "Proposed Spectral Form for Fully Developed Wind Seas Based on the Similarity Theory of S. A. Kitaigorodskii," *Journal of Geophysical Research,* vol. 69, pp. 5181-5190, 1964.

[40] J. Hasselmann, T. P. Barnett, E. Bouws, H. Carlson, D. E. Cartwright, K. Enke, J. A. Ewing, H. Gienapp, D. E. Hasselmann, P. Kruseman, A. Meerburg, P. Muller, D. J. Olbers, K. Richter, W. Sell and H. Walden, "Measurements of wind-wave growth and swell decay during the Joint North Sea Wave Project (JONSWAP)," Deutches Hydrographisches Institut, 1973.

[41] K. O. Merz and H. G. Svendsen, "A control algorithm for the deepwind floating vertical-axis wind turbine," *Journal of Renewable and Sustainable Energy,* vol. 6, no. 5, 2013.

[42] Z. Cheng, K. Wang, Z. Gao and T. Moan, "A comparative study on dynamic responses of spar-type floating horizontal and vertical axis wind turbines," *Submitted to Wind Energy,* 2016.

[43] Statoil, "Vestlefrikk," 13 09 2007. [Online]. Available: http://www.statoil.com/en/ouroperations/explorationprod/ncs/veslefrikk/. [Accessed 03 09 2016].

[44] K. Johannessen, T. S. Meling and S. Haver, "Joint Distribution for Wind and Waves in the Northern North Sea," in *Proceedings of the Eleventh International Offshore and Polar Engineering Conference*, Stavanger, Norway, 2001.

[45] K. Wang, T. Moan and M. O. L. Hansen, "A Method for Modeling of Floating Vertical Axis Wind Turbine," in *Proceedings of the 32th International Conference on Ocean, Offshore and Arctic Engineering*, Nantes, France, 2013.

[46] J. Jonkman, "Definition of the Floating System for Phase IV of OC3," National Renewable Energy Laboratory, Colorado, 2010.

[47] Z. Cheng, K. Wang, Z. Gao and T. Moan, "Dynamic Response Analysis of Three Floating Wind Turbine Concepts with a Two-Bladed Darrieus Rotor," *Journal of Ocean and Wind Energy,* vol. 2, no. 4, pp. 213-222, 2015.

[48] E. E. Bachynski, M. I. Kvittem, C. Luan and T. Moan, "Wind-Wave Misalignment Effects on Floating Wind Turbines: Motions and Tower Load Effects," *Journal of Offshore Mechanics and Arctic Engineering,* vol. 136, no. 4, 2014.

[49] D. Verelst, H. A. Madsen, M. Borg, U. S. Paulsen, H. G. Svendsen and P. A. Berthelsen, "Integrated Simulation Challenges with the DeepWind Floating Vertical Axis Wind Turbine Concept," *Energy Procedia,* vol. 80, pp. 321-328, 2015.

[50] U. S. Paulsen, L. Vita, H. A. Madsen, J. Hattel, E. Ritchie, K. M. Leban, P. A. Berthelsen and S. Carstensen, "1st DeepWind 5 MW baseline design," *Energy Procedia,* vol. 24, pp. 27-35, 2012.